This is to certify that the

dissertation entitled

Growth and Characterization of Epitaxial Films and Magnetic Multilayers Grown By DC Sputtering

presented by

Reza Loloee

has been accepted towards fulfillment
of the requirements for

Ph.D. degree in Materials Science and Engineering

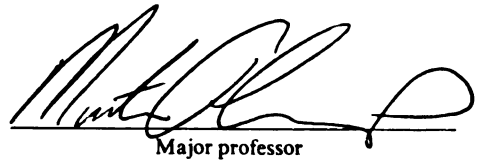

Major professor

Date December 13, 2000

DATE DUE	DATE DUE	DATE DUE
MAR 03 2002		

GROWTH AND CHARACTERIZATION OF EPITAXIAL FILMS AND MAGNETIC MULTILAYERS GROWN BY DC SPUTTERING.

By

REZA LOLOEE

A DISSERTATION

Submitted to
Michigan State University
in partial fulfillment of the requirements
for the degree of

DOCTOR OF PHILOSOPHY

Department of Materials Science and Mechanics

2000

ABSTRACT

GROWTH AND CHARACTERIZATION OF EPITAXIAL FILMS AND MAGNETIC MULTILAYERS GROWN BY DC SPUTTERING.

By

REZA LOLOEE

Epitaxial Nb-Cu-Co and Nb-Cu-Permalloy^{TM} ('Py') multilayers have been grown on (1 1 $\bar{2}$ 0) sapphire substrates by sputter deposition. Electron backscatter diffraction patterns (EBSPs) have been used to characterize individual layers, while atomic force microscopy (AFM) was used for studying surface topography. EBSP is a valuable technique for characterization of these thin sputtered films and shows that the Nb films grow as high-quality epitaxial single crystals with $(110)_{bcc}$ orientations. Cu films grown on the epitaxial Nb display two in-plane epitaxial variants corresponding to two stacking sequences of $\{111\}_{fcc}$ planes. These Cu variants take up the Nishiyama-Wasserman orientation relationship with the underlying Nb. Subsequent sputtering of Co or Py on the epitaxial Cu films results in growth of two variants of $\{111\}_{fcc}$ layers. Orientation maps of the epitaxial Cu, Co, and Py films grown at elevated temperatures, which illustrate the size and distribution of the growth variants, are presented. The EBSP analysis of the epitaxial Cu, Co, and Py samples grown at 90°C or room temperature revealed that two different orientation variants are present. However, due to degradation

of the associated EBSP patterns, mapping of the orientation distributions was not possible.

In this dissertation, the effects of epitaxial growth of sputter-deposited multilayers and spin-valves in a chosen orientation on the magneto-transport properties of these systems are discussed. In particular, sputter-deposited (Py-Cu-Py-FeMn) exchange-biased spin-valves (EBSV) structures were chosen for epitaxial (111)-orientated giant magnetoresistance (GMR) measurements. Optical lithography was used to prepare samples allowing current flow perpendicular to the layer plane (CPP), which provides the best access to the fundamental GMR parameters. The results obtained from magneto-transport measurements revealed that the deposition rate affects the exchange anisotropy between ferromagnetic and antiferromagnetic layers, the CPP-magnetoresistance, and the coercive field of the epitaxial EBSV. Studies of pinning the ferromagnetic layer to the adjacent antiferromagnetic layer along different in-plane axes provided information about the magnetocrystalline and shape anisotropy of both pinned and free ferromagnetic layers. Results have been compared to those for polycrystalline samples.

TO MY PARENTS, MY WIFE AND MY SONS

ACKNOWLEDGMENTS

There are many people in both Department of Materials Science and Mechanics, and Department of Physics and Astronomy that I would like to thank them for their help and support during this study.

Department of Materials Science and Mechanics:

Many thanks go to my thesis advisor, Professor Martin A. Crimp for his guidance and support for duration of this project. I am especially grateful for his patience and encouragement during the writing of this dissertation. I would also like to thank my guidance committee, Professor David Grummon and Professor Thomas R. Bieler for their helpful insights and suggestions.

I would like to thank Steve Ng and Ben Simkin for their help with Cam Scan, Hong Geng for teaching me TEM sample preparation, Dr. John Heckman and Dr. Richard Schalek for editing a part my dissertation.

Department of Physics and Astronomy:

I would like to thank Professor Jack Bass and Professor William P. Pratt for their patience, endless encouragement and support, helpful insights and enthusiastic discussions. I would also like to thank my colleagues, Professor Phillip Duxbury and Professor Thomas Kaplan for helpful discussions. Many thanks are due to Tom Palazzolo, Jim Muns, and Tom Hudson for their help and input on design of sputtering equipment. A special thanks goes to Nate Verhanovitz for helping me with using

AutoCAD drawing software, editing and for writing such wonderful LabView programs for automating our Quick Dippers and sputtering system. I would also like to thank Dr. Juan. A. Caballero for fabricating some of the CPP Spin-valves, training me for microfabrication using photolithographic technique, and having discussion that contributed greatly to my understandings; Dr. Baokang Bi for AFM training; Dr's. Ruby Ghosh and Lowell McCann for editing and great comments. I would like to thank Bob Slater for helping me with some of the sample preparation for GMR measurement. Also our collaborator in Leeds University, Didier Bonzec has made a few samples and many good comments on this project.

I am the most thankful to my wife Hora, my sons, Arshia and Avesta for their patience, support and generous love over the past few years.

I would like to acknowledge and thank the Department of Physics and Astronomy for their support and encouragement for employees seeking higher education.

The financial support for this project was generously provided by the MSU CFMR and the US NSF under grants DMR 98-20135 and MRSEC DMR 98-09688. I also acknowledge the use of the W. M. Keck microfabrication facility at MSU, an NSF MRSEC facility.

TABLE OF CONTENTS

LIST OF TABLES

LIST OF FIGURES

Figures identified with asters in this dissertation are presented in color.

CHAPTER 1

INTRODUCTION

In recent years there has been rapid progress toward the development of a new generation of magnetic devices such as magnetic head readers, magnetic position or velocity sensors, and magnetic random access memory (MRAM). These magnetic devices consist of layered structures with a (ferromagnetic / non-magnetic)$_{N=\text{ number of repeats}}$ configuration, referred to as a magnetic multilayer, e.g. ($[Co/Cu]_N$), or with a (antiferromagnetic / ferromagnetic / non-magnetic / ferromagnetic) configuration, referred to as spin-valve, e.g. (FeMn/Py/Cu/Permalloy^{TM} ('Py')). The operation of these devices is based on the large changes in electrical resistance (ΔR) of a magnetic multilayer upon experiencing an external magnetic field, referred to as giant magnetoresistance (GMR). Large changes in resistance upon application of a very small magnetic field (Oe), small field dependence hysteresis (small coercive field), and small saturation fields are needed to optimize the performance of such devices. GMR in these devices depends on structural details such as the thin-film growth direction, interfacial roughness and intermixing, and grain boundaries. However, the exact effects of these variables on given systems are not yet well understood. Consequently, it is necessary to further characterize the growth and film structure of these magnetic systems to explore the effect of crystal structure on the magneto-transport properties for advanced applications. This dissertation describes the development of sputter deposition techniques for growing epitaxial magnetic multilayers and spin-valves. Furthermore, the dissertation describes the results of crystallographic and magnetic characterization of

sputter-deposited epitaxial samples and compares these with polycrystalline samples made by sputtering.

1.1 THE GMR EFFECT

The operation of some of magnetic devices such as head readers was originally based on a small change (a few percent) in resistivity of a magnetic layer (generally a NiFe alloy) during application of an external magnetic field. The change in the resistance of this type of single magnetic film depends on the angle between the electric current and the direction of applied field (thus, the direction of magnetic moments). This behavior is known as the anisotropic magnetoresistance effect (AMR). AMR is usually expressed by the relation between resistivity and the angle between the magnetization in the ferromagnetic layer.

$$\rho = \rho_0 + \Delta\rho \cdot \cos^2\theta$$

where ρ_0 is the resistivity at zero field, $\Delta\rho$ the change in resistivity upon applying magnetic field, and θ is the angle between the magnetization vector and the applied current [1].

In 1988 two European scientists, P. Gruenberg of Germany and A. Fert of France, discovered a different magnetoresistance effect [2, 3]. Independently, they observed that the application of an external magnetic field to ultra-thin engineered multilayers decreased the resistance drastically. This behavior is called the giant magnetoresistance (GMR).

The GMR effect was first seen in single crystal Fe/Cr superlattices grown by molecular beam epitaxy (MBE), and in sputter deposited polycrystalline Fe/Cr

multilayers [2]. These multilayers consisted of alternating thin layers of magnetic and non-magnetic materials, where with the thickness of the non-magnetic layer chosen so that the magnetic moment of the Fe layers (magnetic layers) align anti-ferromagnetically (anti-parallel = AP state) to minimize the energy. Under application of an external magnetic field, these moments aligned parallel (P state) to each other in the external field and the resistance decreased. The change in resistance in the magnetic multilayer is explained by the two-current series-resistor model. According to this model, there are two spin dependent conduction channels in ferromagnetic materials corresponding to the spin$\uparrow$ (majority) and spin$\downarrow$ (minority) electrons. In the simplest case the change in resistivity is given by the following equation:

$$\Delta\Re = \Re\uparrow\downarrow - \Re\uparrow\uparrow$$

were $\Re\uparrow\downarrow = \dfrac{\Re\uparrow + \Re\downarrow}{4}$ and $\Re\uparrow\uparrow = \dfrac{\Re\uparrow\,\Re\downarrow}{\Re\uparrow + \Re\downarrow}$ are the final resistivities at AP state and P state, respectively, and $\Re\uparrow$ and $\Re\downarrow$ are the resistivity of the spin up and spin down channels in ferromagnetic layers [4]. Figure 1.1 shows a schematic diagram of a magnetic multilayer and the effect of the external field on the resistance (GMR effect). In Figure 1.2, the scattering of spin up and spin down electrons in a multilayer film system is shown. When the magnetic moments of the layers are antiparallel (fig. 1.2(a)), the electrons with one spin sense will scatter in the lower layer while the electrons with the opposite spin sense will scatter in the upper layer, resulting in all of the electrons being scattered and maximum resistance. If the moments are parallel, only electrons with one spin sense will be scattered, the other electrons being free to move, resulting in minimum resistance.

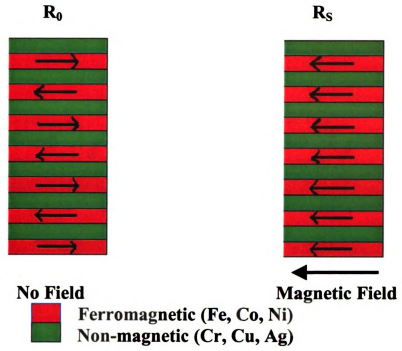

Figure 1.1 a) A representation of antiferromagnetic coupling (external field is zero) and the effect of the applying magnetic field in a magnetic multilayer. b) The field dependence of a Co/Ag multilayer (GMR effect) [10].

Two-Current Channel-Model

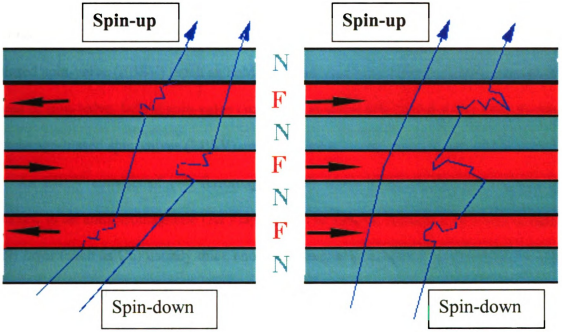

$$\Re\uparrow\downarrow = \frac{\Re\uparrow + \Re\downarrow}{4} \qquad \Re\uparrow\uparrow = \frac{\Re\uparrow \Re\downarrow}{\Re\uparrow + \Re\downarrow}$$

Figure 1.2 Illustration of the scattering of spin-up and spin-down electrons in a magnetic multilayer. F represents a ferromagnetic layer and N represents a non-magnetic layer.

One of the major problems with magnetic multilayers of the original type [2, 3] was the requirement of a high magnetic field (more than 2000 Oe for Co/Cu and more than 10000 Oe for Fe/Cr) for alignment of the magnetic moments parallel to the external field. The high field is not a problem in some applications. However, it is a problem in other areas such as read-heads and MRAMs. This problem was solved by Dieny and co-worker [5, 6] who succeeded in producing the GMR effect in an alternative exchange-biased spin-valve (EBSV) (such as FeMn/Py/Cu/Py) configuration. There is also another type of spin-valve, hybrid spin-valve (such as Co/Cu/Py) [7]. In this study, only Py based exchange-biased spin-valves (EBSV) are considered.

An EBSV consists of two ferromagnetic (F) layers (such as Py), one of which is pinned to an antiferromagnetic (AF) layer (such as FeMn), separated by a non-magnetic (N) layer (such as Cu) usually thick enough so exchange coupling between the Py layers is weak (see Figure 1.3(a)). The role of the AF layer is to pin the in-plane direction of magnetization of the adjacent ferromagnetic layer. In general, spin-valves have the advantage of needing a very small external magnetic field (low switching field) to realign the unpinned (free) magnetic layer to produce the GMR effect. This property makes the spin-valves suitable candidates for low field applications, such as those mentioned above. Figure 1.3(b) shows the GMR effect of a typical Py-based symmetric EBSV. In this figure, the switching from the parallel state to the antiparallel state is relatively fast and requires only 20 (Oe) compared to approximately 450 (Oe) in the Figure 1.1(b).

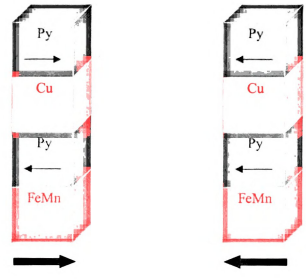

(a)

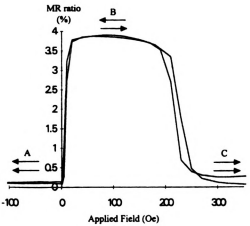

Figure 1.3 a) Two magnetic states (antiparllel and parallel) of a spin valve consisting of an antiferromagnetic layer (FeMn), pinned ferromagnetic layer (Py), nonmagnetic layer (Cu), and free ferromagnetic layer (Py). b) The magnetoresistance of a spin valve shows the GMR effect with small applied field [8].

1.2 GMR MEASUREMENT

In regular magnetic multilayers and spin-valves, GMR is typically measured with a four-probe current-in-plane (CIP) technique (current and magnetic field are parallel). As is described above, the GMR effect arises from spin-dependent scattering at the interfaces of the multilayers and CIP-MR depends on the electron mean free path. Therefore, if the electron mean free path is smaller than the thickness of the non-magnetic interlayer, a weak GMR effect is observed [9]. In the CIP geometry, the current distribution is not uniform, which adds to the complexity of modeling the GMR effect. In the early 1990s, W. Pratt et al. [10] developed a new measurement technique in which the flow of electrons is forced perpendicular through the layers. This configuration is called the current perpendicular to the plane (CPP) geometry. In the CPP geometry, superconducting Nb contacts on the top and bottom of the CPP-MR samples are used to obtain uniform current flow through the layers. Another main difference between CIP and CPP-MR is that the mean free path is not an important factor in the CPP geometry and the spin diffusion length (typically a few hundreds of nm) is the major factor affecting CPP-MR [10]. Because of the high symmetry of the CPP configuration, CPP-MR is theoretically less complex and easier to understand than the CIP equivalent and provides the best access to the fundamental parameters in modeling GMR [11].

In the CPP configuration, the area which electrons flow across is large, about 1 mm^2 (WxT $\approx$ 1 mm x 1 mm) and the resistance is measured across less than 1000 nanometers (L $\approx$ 0.0007 mm), compared to WxT $\approx$ 1 mm x 0.0007 mm and L $\approx$ 3 mm in CIP samples. This results in very small CPP resistances ($R_{CPP} \approx 10^{-7}$ Ω, compared to $R_{CIP} \approx 1$ Ω) which require sensitive measuring devices, such as a superconductive quantum

interference device (SQUID). Figure 1-4(a) illustrates both the CIP and CPP configurations, as well as corresponding GMR measurements (Figure 1-4(b)). Note the much larger GMR response in the CPP configuration. In Figure 1-5, an MSU CPP configuration ($1mm^2$) sample is shown. For study reported in this thesis, however, optical lithography was used to prepare micron-sized pillar samples in the CPP configuration.

1.3 GMR AND EPITAXIAL MAGNETIC SYSTEMS

There are two kinds of interaction between ferromagnetic layers which are separated by a non magnetic layer (metallic). The first is ferromagnetic coupling due to exchange coupling (see Appendix 1-A and [12, 13]) between ferromagnetic layers which depends on the thickness of the non magnetic layer. This type of coupling referred to as Ruderman-Kittel-Kasuya-Yosida (RKKY)-like coupling. This coupling is due to an exchange mechanism with an oscillatory behavior of GMR as a function of nonmagnetic spacer thickness. The second is a magnetostatic coupling known as Neel's orange-peel effect, which is due to the interfacial roughness [14].

In a typical spin-valve, an interfacial interaction (see Appendix 1-A) between the antiferromagnetic and ferromagnetic layers results in an exchange anisotropy, which is a unidirectional anisotropy or 'exchange-bias' [15]. These types of spin-valves, such as FeMn/Py/Cu/Py, are referred to as exchange-biased spin-valves. The exchange-bias is a key feature in spin-valves to achieve the antiparallel and parallel states between the two ferromagnetic layers, one of which is adjacent to the antiferromagnetic layer (details are given in chapter 6). Exchange bias has been studied for both polycrystalline and single-

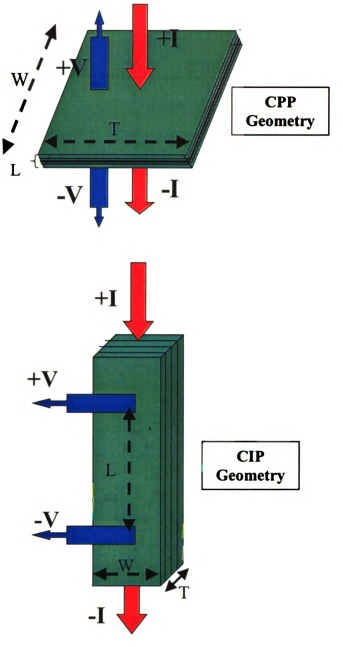

$$R \propto \frac{L}{WxT}$$

$R_{CPP} \approx 10^{-7}\ \Omega$ (L ≈0.7 μm, W ≈ 1000 μm, T ≈ 1000 μm)

$R_{CIP} \approx 1\Omega$ (L ≈3000 μm, W ≈ 1000 μm, T ≈ 0.7 μm)

Figure 1.4 (a) Schematic diagrams of the CPP and CIP configurations. Drawings are not in scale

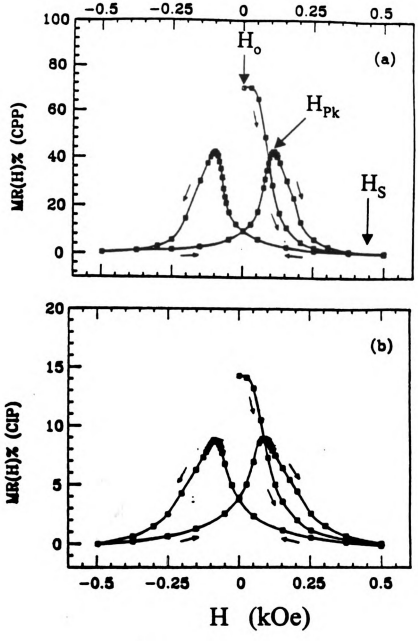

CPP-MR=45% > CIP-MR= 9%

Figure 1.4 (b) The GMR effect in a $[Co(6nm)/Ag(6nm)]_{60}$ magnetic multilayer measured at 4.2 K using the CPP and CIP configurations [10].

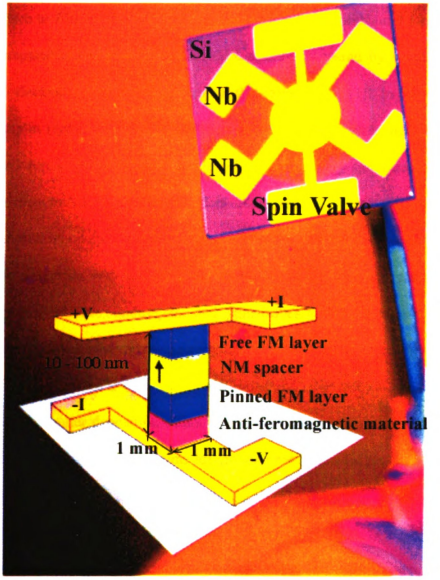

Figure 1.5 A non scaled schematic diagram of the MSU designed CPP spin-valve sample. The up-right corner shows a picture of a sputtered sample with the CPP configuration.

crystal (MBE grown) systems [16, 17].

One of the advantages of the CPP geometry over CIP is that the CPP-MR should be less sensitive to film inhomogeneities such as grains, impurities, and structural defects [14]. Comparable data for Co/Cu CPP-MR samples prepared by standard sputtering, MBE, and electrodeposition seem to support this expectation [11]. In general, epitaxially grown samples (typically grown by MBE) should have fewer structural defects. This is due to the lower kinetic energy of the depositing atoms, very small deposition rate, and ultra-high vacuum ($\sim 10^{-11}$ torr) in such deposition systems. Therefore, epitaxially grown samples should be useful for assessing fundamental GMR parameters and for exploring anisotropic properties with respect to the film crystal structure, e.g. magnetocrystalline anisotropy in magnetic multilayers and spin-valves. At present, epitaxial sputter deposited multilayers have mostly been studied by CIP-MR [18-21]. Only one group has used MBE grown epitaxial Cu/Co(111) multilayers for CPP-MR studies [22]. However, less expensive sputter deposition offers higher deposition rates, and a larger number of substrates in the chamber at same time for growing epitaxial CPP samples.

1.4 DEPOSITION TECHNIQUES

In typical sputter deposition, the substrates are kept at ambient temperature, which results in the growth of polycrystalline films. By selecting a proper single crystal substrate, the growth of a highly textured film is possible [23]. To grow an epitaxial metal film, a proper single-crystal substrate and a high temperature environment (hot substrate) is required [18, 24, 25].

For this study, a new sputtering top assembly with proper accessories, including high and low temperature heaters, was designed and constructed to achieve epitaxial growth of metallic films. This new high temperature assembly top has been used in conjunction with a pre-existing dc magnetron sputtering system.

1.5 CHARACTERIZATION TECHNIQUES

Epitaxial films have been characterized using a wide range of techniques including x-ray diffraction (XRD) [18, 26, 27], reflection high-energy electron diffraction (RHEED) [26-29], low-energy electron diffraction (LEED) [26, 29], neutron diffraction, high-resolution electron microscopy (HREM) [27, 30], scanning tunneling microscopy (STM) [31, 32], and atomic force microscopy (AFM) [33]. However, it is very difficult to obtain enough crystallographic information from an individual technique to form a complete picture of the microstructure (in large scale). For example, x-ray diffraction or neutron diffraction, provide information about spatial average area of the sample [34] but do not provide detailed information about the size and shape of grains, existence and distribution of different variants, and strain in the samples. Therefore, the use of a better characterization technique to examine the relationship between morphology, orientation, and orientation distribution is desirable.

A complimentary approach to many of the above characterization techniques is acquisition of electron backscatter patterns (EBSP), which are made with a scanning electron microscopy (SEM) technique and can measure crystallographic orientations, grain distribution of crystalline materials, and strain in the samples. EBSP is one of the few characterization technique that provides a practical means for coupling between the

orientational and morphological aspects of microstructures in a quantitative and statistically reliable manner [35]. The backscattered electrons form patterns by near-surface diffraction upon exiting the crystals. Therefore, the patterns are dependent on near-surface crystallographic structure. The formation of EBSP has been reviewed in detail by Dingley [36], and a number of computer image processing procedures for analysis of these patterns have been developed [34-38]. However, the application of EBSP and associated orientation mapping to the study of epitaxial metal films and superlattices has only been dealt within a cursory manner.

In this study EBSPs, AFM, and CPP-GMR have been used to characterize the morphologies, crystallite size, orientation distribution (variants distribution), and magneto-transport properties of epitaxial sputter deposited Nb, Cu, Co, and Py films, bilayers, trilayers, multilayers and spin-valves. The relative growth orientation relationships (bcc/fcc) of the substrate and first few layers have been characterized using pole figures obtained from the EBSPs. Studies of films with varying thickness have also allowed assessment of the minimum effective film thickness at which these films may be readily characterized by EBSP. For the first time, orientation mapping has been used to assess grain size and twin morphologies of each epitaxial layer in these magnetic systems. The relationships between structural properties (such as misfit dislocations and point defects), magneto-transport properties (such as, coercive field, GMR value, and magnetization), and magnetocrystalline anisotropy have been observed and are discussed.

APPENDIX 1-A

Exchange Coupling: In most ferromagnetic materials, such as cobalt, nickel, iron, and many alloys of these and other elements, a quantum interaction between neighboring atoms tends to align the atomic magnetic dipoles in parallelism. At low temperature, they become lined-up (coupled) due to their interactions and at high temperature (Curie temperature) randomizing effect overcome the coupling [12, 13]. This quantum interaction is called exchange coupling.

Exchange Anisotropy and Interfacial Interaction: "*Exchange anisotropy refers to the magnetic manifestations of an exchange coupling at the interface between two different magnetically ordered systems*" [39]. For example, when a ferromagnetic film, such as Co, Py, or Fe is deposited on an antiferromagnetic film such as FeMn, CoO, or NiO, by heating the deposited sample to above Néel temperature of the antiferromagnetic and then cool to room temperature in some external magnetic field, the antiferromagnetic film will have a uniform spin direction at the interface. This is due to the influence of the neighboring ferromagnetic spins. The influences of the ferromagnetic layer on the neighboring antiferromagnetic layer due to interfacial interaction is called exchange anisotropy. A simple model of antiferromagnetic-ferromagnetic interaction is shown in figure below.

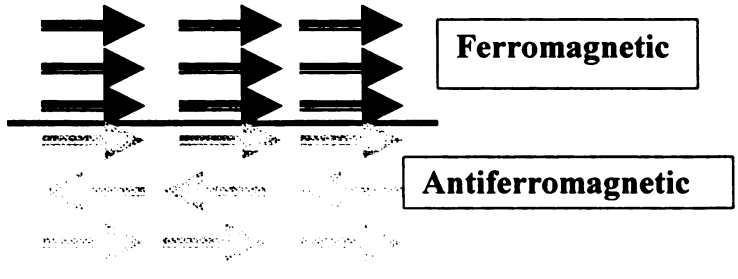

1.6 REFERENCES

1) D. J. Mapps, Applied Magnetism, Kluwer Academic Publisher, 377 (1994).

2) M. N. Baibich, J. M. Broto, A. Fert, F. Nguyen Van Dau, F. Petroff, P. Etienne, G. Creuzet, A. Friederich, and J. Chazelas, Phys. Rev. Lett., **61**, 2472 (1988).

3) G. Binash, P. Grünberg, F. Saurenbach, and W. Zinn, Phys. Rev. B, **39**, 4828 (1989).

4) T. Valet and A. Fert, Phys. Rev. B **48** 7099 (1993).

5) B. Dieny,V.S. Speriosu, S. S. P. Parkin, B. A. Gurney, D. R. Wilhoit, and D. Mauri, Pyhs. Rev. B **43**, 1297 (1991). B. Dieny, V.S. Speriosu, S. Metin, S. S. P. Parkin, B. A. Gurney, and P. Baumgart, J. Appl. Phys., **69** 4774 (1991).

6) A. Fert and P. Bruno, and S.S. Parkin, Ultra –Thin Magnetic Structures, Vol. **2**, Springer-Verlag, Berlin (1993).

7) T. Shanjo, Surf. Sci. Rep., **12**, 49 (1991).

8) M.F. Gillies et al., J. Appl. Phys., **78**, 5554 (1995).

9) P.M. Levy, Solid State Physics Series, Academic Press, **47**, 367 (1994).

10) W. P. Pratt Jr., S.F. Lee, J.M. Slaughter, R. Loloee, P.A. Schroeder, and J. Bass, Phys. Rev. Lett. **66**, 3060 (1991).

11) J. Bass, W. P. Pratt Jr., and P. A. Schroeder, Com. Cond. Mat. Phys., **18**, 223 (1998).

12) H. P. Myers, Solid State Physics, Talor & Franncis, Bristol PA USA, p 374 (1990).

13) D. Halliday and R. Resnick, Fundamentals of Physics, 3ed edition, John Wiley & Sons, Inc. New York p 791 (1988).

14) M. A. M. Gijs and G. E. W. Bauer, Advance in Phys., **46**, 285 (1997).

15) X. Portier, A. K. Petford-Long, P. Bayle-Guillemaud, A. C. Anthony, and J. A. Brug, J. Magn. Magn. Mater. **198**, 110 (1999).

16) A. E. Berkowitz, and Kentaro Takano, Magn. Magn. Mater. **200**, 552 (1999).

17) S. Maat, L. Shen, and G. J. Mankey, Phys. Rev. B, **60**, 10252 (1999).

18) G. R. Harp and S. S. P. Parkin, Appl. Phys. Lett. **65**, 3063 (1994).

19) E.E. Fullerton, M.J. Conover, J.E. Mattson, C.H. Sowers, and S.D. Bader, Appl. Phys. Lett. **63**, 1699 (1993).

20) R. E. Somekh and C. S. Baxter, J. Crystal Growth **76**, 119 (1986).

21) D.J. Smith, A.R. Modak, T.A. Rabedeau, and S. Parkin, Appl. Phys. Lett., **71**, 1480 (1997).

22) N.J. List, W.P. Pratt Jr, M.A. Howson, J. Xu, M.J. Walker, and D. Greig, J. Magn. Magn. Mater. **148**, 342 (1995).

23) I. K. Shuller, Phys. Rev. Lett. **41** 336 (1980).

24) M. Ohering, The Materials Science of Thin Films, Academic Press In., San Diago, (1992).

25) C. P. Flynn, J. Phys. F (Metal Phys.) **18,** L195 (1988).

26) E. Bauer, J. Phys.: Condens. Matter **11**, 9365 (1999).

27) T. Wagner, J. Mater. Res., **13**, 693 (1998).

28) P. Bödeker, A. Abromeit, K. Bröhl, P. Sonntag, N. Metoki, and H. Zabel, Phys. Rev. B, **47**, 2353 (1993).

29) M. T. kief and W. F. Egelhoff, Jr, Phys. Rev. B, **47**, 10785 (1993).

30) J. Mayer, G. Gutekunst, G. Möbus, J. Dura, C. P. Flynn, and M. Rühle, Acta Metall. Mater., **40**, S217 (1992).

31) J. de la Figuera, J. E. Prieto, C. Ocal, and Miranda, Phys. Rev. B, **47**, 13043 (1993).

32) J. Camarero, L. Spendeler, G. Schmidt, K. Heinz, J. J. de Miguel, and R. Miranda, Phys. Rev. Lett. **83**, 2448 (1994).

33) B. Wölfing, K. Theis-Bröhl, C. Sutter, and H. Zabel, J. Phys.: Condens. Matter, **11**, 2669 (1999).

34) B. L. Adams, S. I. Wright and K. Kunze, Metallurgical Transaction, **24A**, 819 (1993).

35) S. I. Wright, J. Computer-Assisted Microscopy, **5**, 207 (1993).

36) D.J. Dingley, Scanning Elect. Microsc., IV **273** (1981).

37) N.C. Krieger Lassen, D. Jul Jensen and K. Conradsen, Scanning Microscopy, **6**, 115 (1992).

38) A.J. Wilkison and D.J. Dingly, Acta Metall. Mater., **40**, 3357 (1992).

39) A. E. Berkowitz and K. Takano, J. Magn. Magn. Mater. **200**, 552 (1999).

CHAPTER 2

EXPERIMENTAL PROCEDURES

2.1 INTRODUCTION

The focus of this study was to design and develop a sputtering system to grow epitaxial magnetic multilayers and spin-valves, and to optimize techniques for epitaxial growth. The sputter deposited samples were characterized using different techniques including AFM, EBSP, CPP GMR, and magnetometry. These techniques have provided information about the orientation, orientation distribution, and magneto-transport properties of epitaxial films, multilayers, and spin-valves.

This chapter is divided into four sections: apparatus design and development, growth techniques, structural characterization, and magneto-transport characterization.

2.2 APPARATUS DESIGN AND DEVELOPMENT

There are a number of different film deposition techniques. Molecular beam epitaxy (MBE), thermal evaporation, metal organic chemical vapor deposition (MOCVD), chemical vapor deposition (CVD), and sputter deposition are among the most widely used. Sputter deposition is divided to four branches: ion deposition, ion-assisted deposition, DC & RF magnetron deposition, and RF & DC triode–magnetron deposition.

An ultra-high vacuum, dc-magnetron (triode) sputtering system, located in the Physics and Astronomy Department at Michigan State University, has been modified for this study. An existing room temperature chamber top assembly has been used in the past to

grow polycrystalline and amorphous films and multilayers. A new high temperature chamber top assembly has been designed and built for this study to grow epitaxial films and multilayers and regular polycrystalline films and multilayers. The main emphasis was on the design of two substrate heater assemblies. One has both cooling and heating capability, with substrate temperatures ranging from below room temperature to about 600°C. The second one was designed for high temperature sputter deposition, with substrate temperatures ranging from 600°C to 1200°C. Each heater assembly can be lowered onto given substrate when heating is required. A brief description of dc-magnetron sputter deposition technique and the design of both tops is included in this chapter.

2.2.1 Sputtering:

A typical dc-magnetron (triode) sputtering gun system consists of three electrodes: an anode, a cathode, and a target. The sputtering chamber must be evacuated usually to a base pressure of $1x10^{-8}$ torr or lower. Lower pressure will provide cleaner sputtering environment (lower partial pressure of water vapor, N_2, O_2 and etc.) and therefore cleaner films (free from impurities). Sputtering takes place in purified argon gas at various pressures, typically 2-5 $x10^{-3}$ torr. Upon applying a high current to the filament (cathode), the heated filament emits electrons that accelerate toward the anode. These accelerating electrons ionize the Ar gas molecules in their paths creating positive ions. The target is located between the anode and cathode and the whole assembly is coupled to a pair of parallel magnets. Applying a negative voltage to the target creates a potential difference between the positive ions and the target, and the ions accelerate toward the

target (ion bombardment). During bombardment, the ions physically remove atoms from the target surface. The neutral ejected atoms flow toward the substrate where they adhere. Each sputtering gun assembly is water-cooled. Figure 2.1 give an overall view of the triode-sputtering system.

The following are advantages of triode sputtering over other deposition techniques:

- Both conductive and semiconductive materials can be deposited.
- Higher deposition rates are possible.
- The small ratio of residual gas molecules to sputtered atoms results in higher film densities and fewer impurities.
- The film composition is uniform and usually very similar to the target composition.
- Precise control of the deposition rate is possible by independent regulation of the plasma and/or target voltage.
- Maximum usage of the target material (up to 90%) is possible.

The sputtering system used for this study contain four independent Simard triode sputtering guns with a 2.25″ x 0.25″ (diameter x thickness) target size and a regular diode magnetron gun with a one inch target size. The five gun assemblies provide a capability of making a variety of multilayer samples. Figure 2.2 shows top views of the gun assemblies. A mechanical pump and a cryo-pump are used for evacuation. The plasma voltage, target current, and deposition rate of all sputtering guns are monitored by a PC running a LabVIEW program.

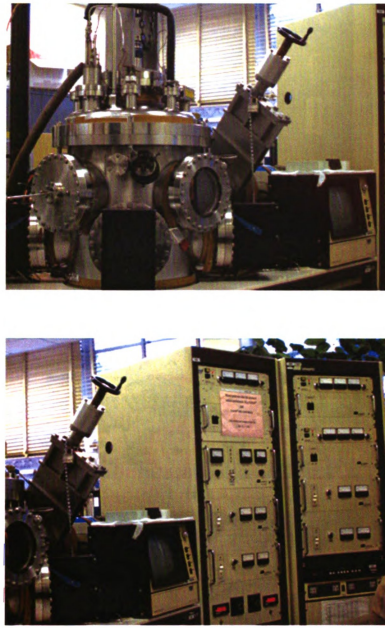

Figure 2.1 Front views of the MSU sputtering system with four dc-triode guns and a magnetron gun capability, including the related power supply and the residual gas analyzer.

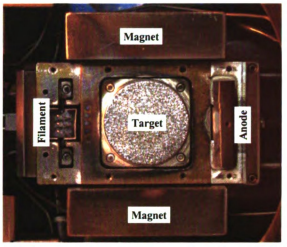

(a)

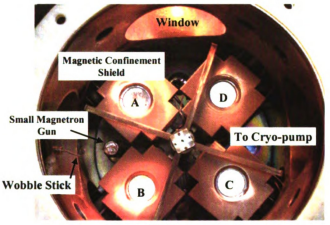

(b)

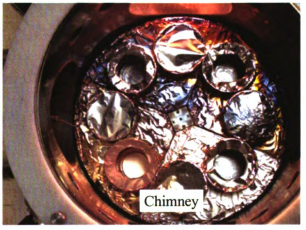

(c)

Figure 2.2 Top views of: a) an unassembled triode gun, b) four assembled guns with FeMn, Cu, Py, and Nb targets, c) four chimneys in the open position. Note that after deposition a computer controlled stepper motor rotates the chimneys to the closed position to protect the samples.

2.2.2 Room Temperature Chamber Top Assembly:

The room temperature chamber top assembly is hemispherical in shape and is made of stainless steel. This chamber top consists of the following components: cold trap, cooling system, thermocouples, shaft connected to a stepper motor, sample positioning and masking apparatus (SPAMA) plate, film thickness monitor (FTM), and substrate holders. Figure 2.3 shows photographs of the overall system and an inside view of the room temperature chamber top assembly. The cold trap is essential for freezing any remaining water vapor. Liquid nitrogen (LN_2) for the cold trap flows continuously during sputter deposition. The cooling system consists of a capillary tube that passes through the LN_2 in the cold trap. Dry nitrogen gas at 1000 psi pressure flows through the capillary tube. By controlling the dry nitrogen gas pressure, the substrate can be cooled to -100°C. Three K-type thermocouples (chromel-alumel) monitor the substrate temperatures during deposition. The SPAMA plate assembly is connected to a computer-controlled-stepper motor through a shaft. The stepper-motor is on the outside of the chamber, and the shaft goes into the chamber through a rotary feed-through.

2.2.3 High Temperature Chamber Top Assembly:

The high temperature chamber top assembly was designed and assembled by Professor W. Pratt of Physics and Astronomy Department and the author. As briefly described in the introduction (section 4), two substrate heater assemblies were designed. One with both cooling and heating capability, ranging from below room temperature to about 700°C. The second, for high temperature growth, ranging from 700°C to 1200°C. The general principle behind the design of these heaters was based on two heating

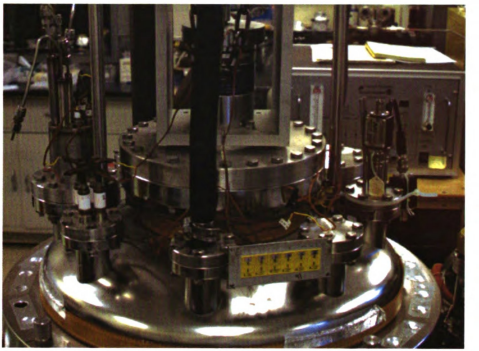

(a)

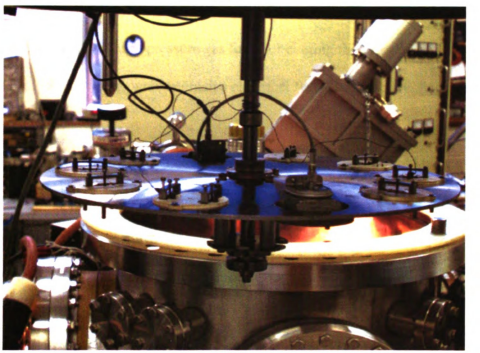

(b)

Figure 2.3 (a) A top view of the room temperature chamber top assembly. (b) A side view of the SPAMA plate, including the CPP and CIP substrate holders and FTMs.

techniques: (1) Heating by radiation (photons) for 700°C -1200°C and (2) Heating by conduction (phonons) for below 700°C. The detail of design and operation of both heaters will be discussed in next sections.

Most of the chamber top parts were manufactured in the machine shop of the Physics and Astronomy Department at Michigan State University. The high temperature chamber top assembly was based on a flat plate made of stainless steel. The top provides the following:

- One 1.5″ UHV viewport.
- Two wobble sticks; each mounted on a 2¾″ 'ConFlat' (CF) flange, for lowering the heaters onto the substrates or raising the heaters when not in use.
- One 2¾″ CF flange which contains a BNC connection for a film thickness monitor and two high-pressure gas lines for cooling the low temperature heater.
- One 2¾″ CF flange which contains electrical feed-through providing current to both heaters.
- One 2¾″ CF flange which contains liquid Nitrogen lines for cold trap.
- One 2¾″ CF flange which contains water lines for cooling the Cu heat shield of the high temperature heater.
- One 2¾″ CF flange which contains feed-through for both C-type and K-type thermocouples
- One stepper motor for rotating the SPAMA plate.

Figure 2.4 shows some of these accessories of the high temperature chamber top assembly.

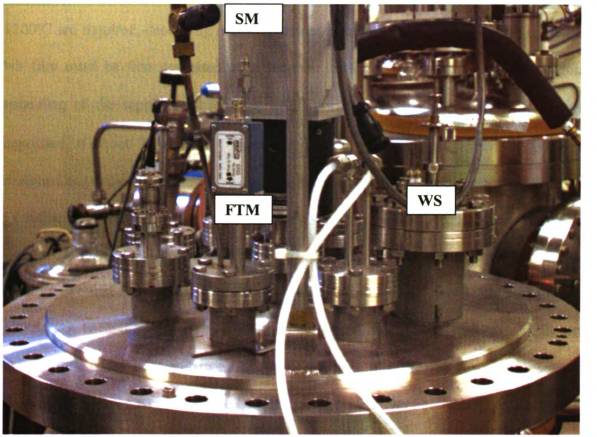

Figure 2.4 A top view of the high temperature chamber top assembly including the wobble sticks (WS), FTM amplifier (FTM), stepper motor (SM), and some of the feed throughs.

High Temperature Heater:

The high temperature chamber top assembly was designed for growing epitaxial films and multilayers. In epitaxial growth, substrate temperatures in the range of about 200 to 1200°C are required, depending on the sputtered element [1]. In this study, an epitaxial Nb film must be first deposited on a sapphire substrate. However, a pre-deposition annealing of the sapphire substrate at 1200°C was required before the Nb film was deposited at about 700-900°C. Therefore, the high temperature heater (HTH) was designed and dedicated to annealing sapphire substrates and depositing epitaxial Nb films by radiation technique. The heater element (VXPBN1A) was purchased from Kurt J. Lesker Company, Clairton, PA and consisted of a film of carbon (graphite) sandwiched between two thin layers of pyrolytic boron nitride. At full power, this heater could reach 1700°C. A basic description of HTH assembly is provided in Figure 2.5 (a). As shown in this figure, the heater element was held by two long molybdenum (Mo) screws (insulated), which also act as the electrodes. There were two heat-shields, made out of 0.005" Mo foil, surrounding the heater element and the substrate holder assembly (when the HTH was in its lowered position). There were two C-type thermocouples, one on the back of heating element and one in front. When the heater was lowered, the front thermocouple came in direct contact with the back of the substrate,. Upon lowering, the separation between the heating element and the substrate was about 1-2 mm. The heating then took place through radiation from the white-hot heater (photons). However, the sapphire is transparent to the photons. Therefore, a thin layer (~200 nm) of Nb must be deposited on the backside of substrate to block the photons and provide a uniform temperature during deposition on the front (polished side) of the sapphire substrates. The

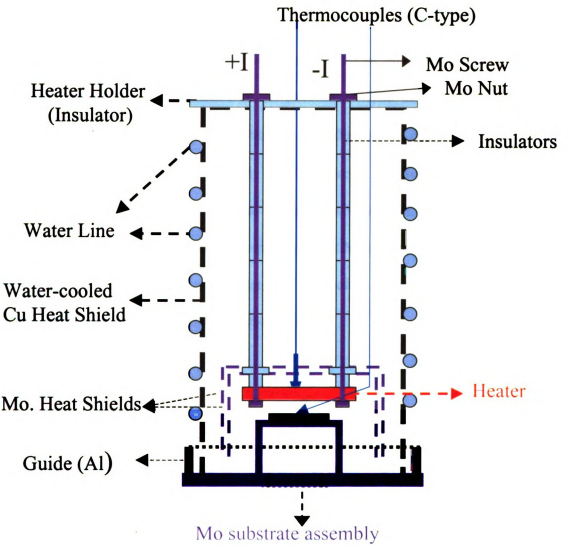

Figure 2.5(a). A schematic of the high temperature heater assembly in its lowered position. The assembly slides into the Al guide, on top of the substrate holder.

temperature of substrates during high temperature annealing and deposition of Nb films were measured by using the front thermocouple. In addition, an optical pyrometer was used for calibrating and checking the accuracy of this thermocouple for temperatures above 700°C. The optical pyrometer could be aimed onto the front of the heated substrate through a sapphire window located on the bottom of the sputtering chamber. Having a Nb film on the backside of sapphire substrates ensured that the pyrometer accurately measures the temperature of the substrates. Due to the high temperatures (high $T \geq 700°C$), a water cooling system was provided for HTH assembly. The water lines were flexible but limit the mobility of the heater in its lowered position to $\pm 90°$ rotation of the SPAMA plate. A vertical two-stage wobble-stick was used for lowering and raising the HTH. For deposition of epitaxial multilayers, the heater had to be able to move with the substrate over several targets. Therefore, a second heater with larger mobility and lower temperature range was desired.

Low Temperature Heater:

A second heater (a low temperature heater = LTH) was designed with an angular mobility of 270° for the SPAMA plate. The LTH is dedicated for growing epitaxial films and multilayers that required lower growth temperatures (below room temperature to 600°C). LTH heater is more accurate than the HTH in this temperature range, because the substrate is heated by conduction (phonons) via direct contact between the heater and substrate. A basic description of LTH assembly is illustrated in Figure 2.5 (b). As shown in this figure the heating element (same as the heating element in the HTH) is in direct contact with the stainless steel (SS) jacket. The two Mo screws (insulated) act as heater

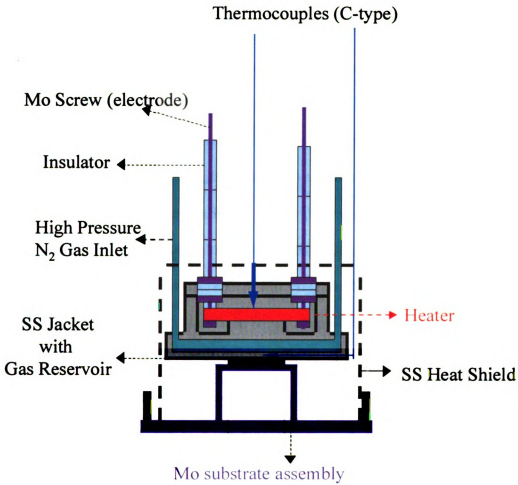

Figure 2.5(b) A schematic of the low temperature heater assembly in its lowered position. This heater is in direct contact with the substrate and capable of being cooled from 600°C to about room temperature within a few minutes, using cooled-high pressure nitrogen gas.
SS = Stainless Steel

electrodes and hold the heating element in direct contact with the jacket. The LTH SS jacket could be cool down by high-pressure nitrogen gas (capillary tube) from 600°C to about room temperature in a few minutes. There were two c-type thermocouples in LTH assembly, one right on the top of heater element and the other was inside the bottom wall of the jacket. The thermocouple in the lower part was calibrated by using a third thermocouple (K-type), which was attached to the front of the test-substrate (using silver paint). A second vertical, two-stage, wobble-stick eas used here to lower and raise the LTH. Figure 2.6 shows two different side views of the HT top, including pictures of both types heaters. In Figure 2.7, a top view of the substrate holders, including the heat shield guide, and a high temperature molybdenum (Mo) mask is shown. The substrate holders were designed to avoid heating the SPAMA plate during annealing and deposition. Four Mo rods (0.035" OD) are used to keep each substrate holder ½ inch above the SPMA plate. All the holders are also made from Mo plate (0.042"). A stainless steel sliding-shutter keeps the substrate and films from being contaminated by sputtering. Four C type (tungsten-rhenium) thermocouples monitor the temperatures of the heaters, substrate, and SPAMA plate. The thermocouples are either 0.005" or 0.01" in diameter with a useful temperature ranges of 0-2320°C: +Lead: W(5% Re) and -Lead W(26% Re).

2.3 THE GROWTH TECHNIQUES

2.3.1 Polycrystalline Films and Multilayers:

All of the polycrystalline films and multilayers were sputter deposited in the temperature range of –30°C -to- +30°C. The deposition rates varied from 5 to13 Å/s, depending on the target material. Several polycrystalline films and multilayers were

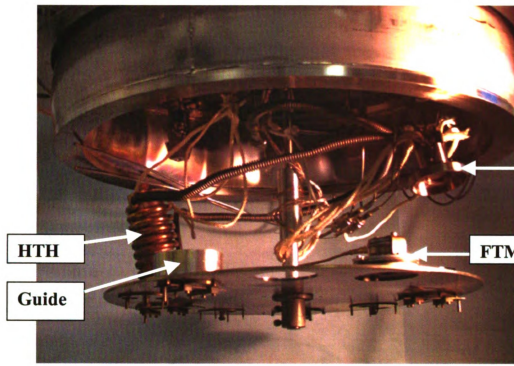

(a)

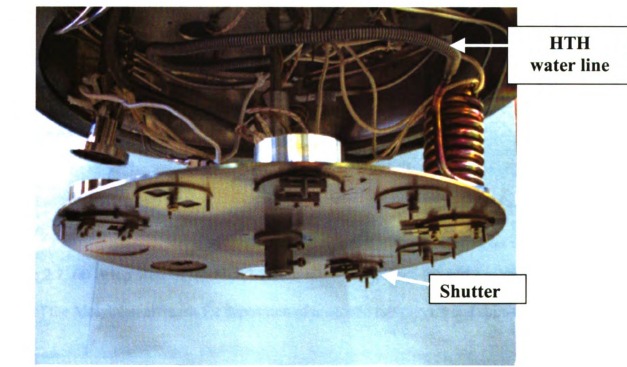

(b)

Figure 2.6 Side views of high and low temperature heaters, sliding shutter, cooling water line, and other accessories.

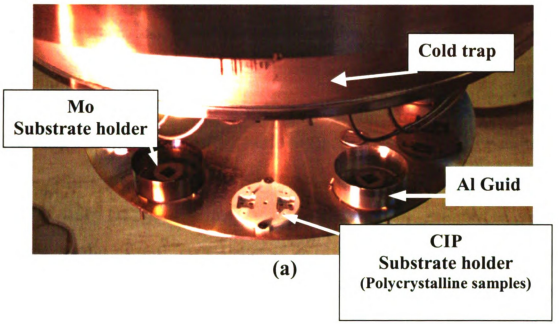

Figure 2.7 (a) A top view of the Molybdenum substrate holders, (b) and a schematic top view of the Molybdenum mask for deposition of magnetic multilayers and spin-valves.

grown at low temperature for comparison to similar epitaxial films and multilayers. The results obtained form these comparisons are discussed in chapters (4-6).

2.3.2 Epitaxial Films and Multilayers:

To achieve fully epitaxial growth in multilayers and spin valves containing $Nb(110)_{bcc}$, $Co(111)_{fcc}$, $Cu(111)_{fcc}$, and $Py(111)_{fcc}$ layers, it is necessary to establish optimum deposition conditions for each subsequent layer. Because of reactivity between Co (and possibly Py), with Nb, Co and Py should not be deposited directly on Nb [2,3]. Therefore the sequence of Nb-Cu-$[Co\text{-}Cu]_N$ or Nb-Cu-Py-... is preferred.

Growth conditions in a preferred orientation: To grow epitaxial CPP multilayers and spin-valves in the preferred (111) orientation (such as Cu/Co(111) multilayers or FeMn-Py-Cu-Py(111) spin-valves), the epitaxial Nb contact layer must first be grown in a $(110)_{bcc}$ orientation [4]. $(11\bar{2}0)$ oriented Al_2O_3 has been reported to be a suitable substrate for growing an epitaxial (110) Nb film [5]. In the present study, sapphire substrates with one side polished to within 0.3 degree of the $(11\bar{2}0)$ A-plane were purchased from Union Carbide.

Substrate cleaning: Most of the substrates were prepared in the sputtering room, cleaned with acetone and then alcohol in an ultrasonic bath. Others were first cleaned in a combination of boiling deionized (DI) water and detergent (Alconox) in an ultrasonic bath, then rinsed in boiling deionized water, rinsed again and mechanically cleaned in acetone using cotton swabs, rinsed in isopropyl alcohol, and finally rinsed with DI water and dried with industrial grade nitrogen gas. These latter substrates process were all in a clean room.

Substrate annealing: After reaching the desired vacuum (~1 x 10^{-8} torr), the substrates were pre-deposition annealed at 1200°C for twenty minutes to remove any residual organic layer and to decrease the surface roughness.

Deposition process: To determine the optimum growth temperature, Nb films were sputtered using substrate temperatures ranging from 25 to 1200°C. To improve the surface smoothness, some of the sputtered films were post-annealed at 950°C for ten minutes. The high temperature heater (HTH) was then turned off and allowed to cool-down while the low temperature heater (LTH) was heated up to the desired temperature in range of 150-500°C. Upon removal of the HTH, the SPAMA plate was rotated to the position for loading the LTH. Cu films were then deposited onto the Nb at temperatures ranging from ambient temperature to 500°C. Some of these samples (grown at low temperatures) were then post-annealed in a temperature range of 250 to 500°C. Finally, the Co, Py, and FeMn films were deposited at desired temperatures ranging from room temperature to 460°C.

Deposition rates: The deposition rate for each element was measured using a quartz film thickness/rate monitor. A typical deposition rate was 3-4 Å/s for most samples. However, samples were also grown with different deposition rates for comparison purposes.

2.4 STRUCTURAL CHARACTERIZATION

Epitaxial films were structurally characterized using atomic force microscopy (AFM) and electron backscatter diffraction patterns (EBSP). EBSP is capable of measuring crystallographic orientations of single-crystal and/or large grain polycrystalline materials

with a spatial resolution of approximately 1° and a detection depth of approximately 200 nm [6-9].

In this section a brief description of both instruments that were used for structural characterization of epitaxial samples are reviewed.

2.4.1 Atomic Force Microscopy

Description: A Digital Instruments atomic-force microscope (AFM) with tapping mode capability was used to image the surfaces of the films. This microscope has three operational modes: contact, tapping, and lateral force modes. Each mode measures different forces that act between the tip of cantilever and atoms on the surface of specimen. One of the most important forces is the interatomic force called the van der Waals force. This force is strongly dependent on the distance between two atoms and consists of a repulsive force and an attractive force. The operation of the contact and tapping modes are based on the repulsive part of the interatomic force as the cantilever approaches the surface of the specimen. In the tapping mode, the cantilever alternately contacts the specimen surface and lifts the cantilever off the surface to avoid dragging the tip across the surface of the specimen. A schematic of a AFM microscope is shown in Figure 2.8 (Courtesy of Digital instruments [10]).

Sample preparation: Samples for atomic force microscopy did not require any specific sample preparation. The samples must be clean and free of dust. A new cantilever enhances the resolution of the images.

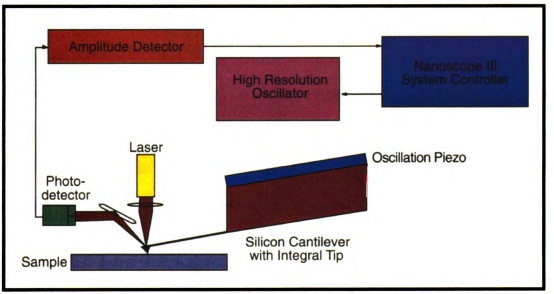

Figure 2.8 Block diagram of the components used in DI atomic force microscope with a tapping mode capability. (Courtesy of Digital Instruments [5])

2.4.2 Electron Backscatter Diffraction Pattern:

Description: Electron backscatter patterns (EBSP) is a scanning electron microscope (SEM) diffraction technique for measuring crystallographic orientations of single-crystal and/or polycrystalline materials. An EBSP consists of many intersecting, linear features called Kikuchi bands. These bands have slightly higher intensities with respect to a non-uniform background. This contrast is due to the diffraction of backscattered electrons by the crystal [8].

When an electron beam is incident on a sample, different interactions take place. The emission of secondary electrons, backscattered electrons, x-rays, and Auger electrons are among the most important results of these interactions. The electrons that impinge on the specimen surface (in all directions) go through inelastic scattering, losing about ~1% of their energy, and establish an interaction volume in the specimen. Near the surface, those backscattered electrons that satisfy the Bragg diffraction condition for a particular set of planes are channeled differently than the non diffracted ones and produce a change in intensity. These diffracted electrons are called the backscattered diffracted electrons (Figure 2.9 (a)). The diffracted backscattered electrons from each set of planes form a cone with its axis normal to the plane. The number of backscattered electrons depends on the atomic number, Z, of the specimen. The relationship between these two variables is given by the series:

$$\eta = \eta_{BSE} / \eta_B = -0.254 + 0.016Z - [1.86\text{x}10^{-4}]\, Z^2 + \ldots\ldots$$

where η is the backscatter coefficient, η_{BSE} is the number of backscatter electrons, η_B is the number of incident electrons, and Z is the atomic number [6].

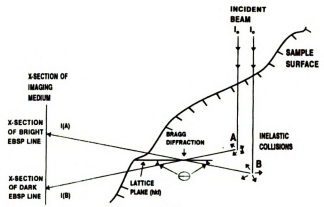

(a)

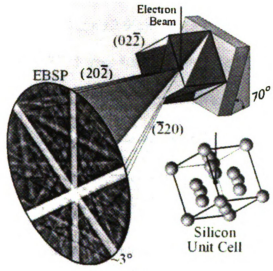

(b)

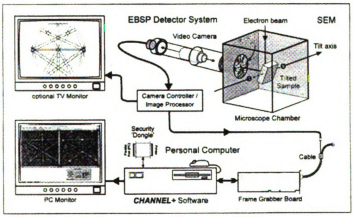

(c)

Figure 2.9 a) Schematic representation illustrating the inelastic collisions, Bragg diffraction, and resultant formation and imaging of EBSPs as a result of an incident electron beam. Adopted from [6]. b) A diagram of three set of band from {220} plane that are projected onto the phosphor as a pair of cones.. c) Experimental set-up for EBSP measurements. Figures (b) and (c) are adopted from [10].

The number of backscattered electrons escaping from the surface of specimen, is also dependent on the tilt angle of specimen: $\eta(\theta) = \frac{1}{(1+\cos\theta)^{9/Z^{1/2}}}$.

Usually, a tilt angle of approximately $\theta = 70°$ with respect to the electron beam is optimum. Figure 2.9(b) shows a schematic illustration of the diffraction cone and the pattern formation on the phosphor screen placed in front of the sample. A diagram of the EBSP system set-up is shown in figure 2.9(c).

A CamScan 44FE FEG-SEM was used to produce backscattered electrons. An accelerating voltage of 25 kV, emission current of approximately 120 μA, objective aperture of 50μm, and a working distance of 22 or 21 mm was used for this study. A CamScan ORTEX CCD video camera images the phosphor screen. The imaged patterns were then transferred to a Hamamatsu ARGUS-10 image processor which subtracts the background noise from the diffracted patterns. The processed patterns were then saved and analyzed using an interfaced PC. The detection and indexing of the Kikuchi bands can be performed either manually or automatically using the Channel 4 software package [11]. This software determines the crystal orientations and displays the orientation data in the form of pole figures and inverse pole figures. The Channel 4 orientation software was also used to display crystal grain orientation maps of desired areas, which have been scanned by moving either the electron beam or the sample (stage). The time required for the collection of a set of data varied from two hours to six days, depending on the length and step size of the scan. The spatial resolution of the EBSP technique is approximately 1 μm, but it is limited to the volume a few tens of nanometers below the surface [9]. Figure 2.10 shows the CamScan FE44 SEM and its accessories.

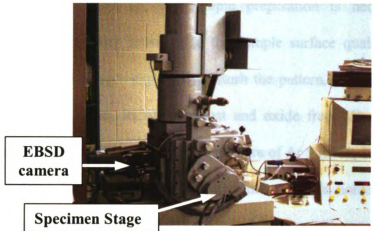

(a)

(b)

(c)

Figure 2.10 (a) A view of the CamScan 44FE electron microscope column, (b) a front view of main panel, (c) and PC monitor displaying an EBSP before and after indexing.

Sample preparation: No specific sample preparation is necessary for EBSP. However, since EBSP is very sensitive to the sample surface quality; a dirty, rough, and/or heavily oxidized surface can easily disturb the pattern. Therefore, care must be taken to keep samples clean, as well as dust and oxide free. During this study, all samples were kept in desiccators filled with a mixture of Ar 98% H_2 2% gas.

Sample holders: Two different kinds of aluminum sample holders, one a half inch round plate (which holds one sample) and a one inch by one inch square plate (capable of holding up to four ½ inch x ½ inch samples) were used. Since the sapphire substrates were insulators, silver paint was used to make electric conduction between the samples and the Al sample holders. A piece of p-type (100) Si wafer, placed along side the sample, was used to calibrate the EBSP system with respect to the X-Y-Z stage.

2.5 MAGNETO-TRANSPORT CHARACTERIZATION:

Special equipment was required for the measurement of the magnetic and magneto-transport properties of magnetic multilayers and spin-valves (such as magneto-resistance, magnetization, and coercivity of magnetic films). Sections 2.5.1 and 2.5.2 contain brief discussions of how these magnetic properties were measured.

2.5.1 Magneto-Resistance (CPP-GMR measurements)

Description: CPP measurements require Nb superconducting contact layers on the top and bottom of the multilayers and spin valves. To measure the very small resistance ($\sim 10^{-7}\ \Omega$) in CPP samples, a superconducting quantum interference device (SQUID) was

used. A detailed description of the CPP-GMR measurement apparatus has been reported elsewhere [12].

Sample preparation: A molybdenum mask was used to sputter the epitaxial multilayers and spin-valves in a L-shape (1 mm x 8 mm) pattern as was shown in figure 2.7(b). After sputtering the epitaxial samples, the top surface is often gold coated for protection. A series of 75 and 6 μm square pillars are then fabricated using photolithographic techniques. The details of the photolithography fabrication have been reported elsewhere [13]. The spin-valve samples are then pinned in an oven filled with Ar 98%H_2 2% gas. In a typical pinning process, samples are heated up to ~200°C in the presence of about 30 Oe magnetic field. After cooling the sample, the ferromagnetic layer is pinned to the adjacent antiferromagnetic layer through exchange-biased coupling. The pinned direction, which is referred to as the easy axis, is along the applied field. The details of the pinning process are given in chapter 6.

2.5.2 Magnetization

Description: A Quantum Design SQUID magnetometer is used to measure the magnetization of multilayers and spin-valves. This magnetometer has the capability of making fast, precise measurements of the dc magnetic properties of magnetic multilayers and spin-valves over a wide range of temperatures (2-350 K) and applied fields (±1 Tesla, and 1 Tesla = 10000 Oe)

Sample preparation: The sample chamber of this magnetometer was cylindrical, approximately 7 mm in diameter. The diameter of epitaxial films were approximately 11mm x 11mm. Therefore, these samples were cut in half (~5 mm) and placed vertically into the sample chamber. No other specific preparations were required.

2.6 REFERENCES:

1) C. P. Flynn, J. Phys. (metal Phys.), **18** L195 (1988).

2) K. Bröhl, P. Bödeker, N. Metoki, A.Stierle, and H. Zabel, J. Crystal Growth, **127**, 682 (1993).

3) R. E. Somekh and C. S. Baxter, J. Crystal Growth **76**, 119 (1986).

4) W. P. Pratt Jr., S.F. Lee, J.M. Slaughter, R. Loloee, P.A. Schroeder, and J. Bass, Phys. Rev. Lett. **66**, 3060 (1991).

5) S. M. Durbin, J. E. Cunningham, M. E. Mochel, and C. P. Flynn, J. Phys.: Met. Phys., **11**, L223 (1981).

6) A. W. Gibson, M.S. thesis, Michigan State University, (1995).

7) D.J. Dingley, Scanning Elect. Microsc. **IV,** 273 (1981).

8) N.C. Krieger Lassen, D. Jul Jensen and K. Conradsen, Scanning Microscopy **6**, 115 (1992).

9) A.J. Wilkison and D.J. Dingly, Acta Metall. Mater. **40**, 3357 (1992). 8) S. I. Wright, J. Computer-Assisted Microscopy **5**, 207 (1993).

10) Digital Instrument, Instruction manual (1997).

11) CHANNEL 4 orientation mapping manual; HKL Technology, (1997).

12) P. Holiday, Ph.D. dissertation, Michigan State University, (1996).

13) R. D. Slater, J. A. Caballero, R. Loloee, and W. P. Pratt, Jr., Submitted for publication in J. Appl. Phys. (2001).

CHAPTER 3

GROWTH OF Nb FILM ON SAPPHIRE

3.1 INTRODUCTION

As outlined in chapter one, it is necessary to establish optimum growth conditions for each subsequent layer to achieve epitaxial multilayers and spin-valves of $Co(111)_{fcc}$, $Cu(111)_{fcc}$, and $Py(111)_{fcc}$. Furthermore, to measure GMR in magnetic multilayers and spin-valves with current flow perpendicular to the layer planes (CPP), a Nb contact layer must be grown prior to the deposition of the multilayer [1]. A (111) growth direction in the fcc magnetic multilayers and spin-valves can be achieved by using epitaxial $Nb(110)_{bcc}$ substrate [2-4]. Therefore, the epitaxial Nb layer is the foundation of the epitaxial magnetic layer system, and the growth and characterization of this Nb film is an important step towards building high quality epitaxial magnetic structures. In this chapter, the growth of epitaxial Nb on a single crystal of sapphire is discussed. This discussion is followed by the crystallographic characterization of sputter deposited Nb films, using AFM and EBSP.

3.2 BACKGROUND

The epitaxial growth of Nb films on Al_2O_3 substrates (metal-ceramic), using several different techniques such as MBE and sputter deposition, has been extensively investigated [2-20]. In these studies different characterization techniques have been used to investigate the nucleation, the growth, and the interfaces of the Nb films grown on different orientations of sapphire.

Nb and Al_2O_3 have very similar thermal expansion coefficients and Nb thin films grow on Al_2O_3 almost strain free with a highly quality crystal structure and large coherence lengths [11,13]. Crystallographic data and some of the thermal properties for both Nb and Al_2O_3 are summarized in Table 3-1. Orientation relationships are defined by the interface planes and two parallel directions in the two materials. In the Nb/Al_2O_3 system, different orientation relationships have been observed (for examples see [2,9]):

$$(0001)Al_2O_3 \parallel (111)Nb \text{ with } [2\bar{1}\bar{1}0]Al_2O_3 \parallel [10\bar{1}]Nb$$

$$(01\bar{1}0)Al_2O_3 \parallel (\bar{1}2\bar{1})Nb \text{ with } [0001]Al_2O_3 \parallel [111]Nb$$

$$(11\bar{2}0)Al_2O_3 \parallel (\bar{1}01)Nb \text{ with } [0001]Al_2O_3 \parallel [111]Nb$$

$$(01\bar{1}2)Al_2O_3 \parallel (0\bar{1}0)Nb \text{ with } [2\bar{1}\bar{1}0]Al_2O_3 \parallel [10\bar{1}]Nb$$

Because of the above orientation relationships, the growth direction of epitaxial Nb films can be selected by choosing the properly matched sapphire substrate.

In this study an epitaxial Nb(110) underlayer (contact layer) was required for growth of the subsequence epitaxial magnetic multilayer structures and spin-valves in a (111)fcc orientation. It has been shown that bcc Nb(110) planes can be grown epitaxially on Al_2O_3 $(11\bar{2}0)$ substrates [2, 3, 9]. The in-plane epitaxial relationships are:

$$[0001]Al_2O_3 \parallel [111]Nb$$

$$[1010]Al_2O_3 \parallel [121]Nb$$

A portion of the corundum (sapphire) cell and atomic packing of a $(11\bar{2}0)$ plane of sapphire are shown in Figure 3.1 [21, 22].

Table 3-1

CRYSTALLOGRAPHIC DATA

Element:	Al_2O_3 - Corundum - Sapphire	Nb–Niobium-Columbium
Crystal system:	Hexagonal-Rhombohedric *	Cubic – bcc
a = b = c =	0.4763 nm 0.4763 nm 1.3003 nm	0.33067 nm 0.33067 nm 0.33067 nm
Unit cell volume:	0.2555 nm^3	0.0359 nm^3
# of atoms per unit cell:	12(Al) + 18(O) = 30	2
Atomic radius: Ionic Radius	Al = 0.143 nm Al^{3+} = 0.051 nm O^{2-} = 0.132 nm	Nb = 0.143 nm Nb^{+4} = 0.074 nm
Symmetry:	A single 6-fold rotation axis	Four 3-fold rotation axes
Melting Point:	2052 °C	2469 °C
Thermal expansion coefficient:	$5.4 \times 10^{-6}\ C^{-1}$ ‖ c-axis RT $6.2 \times 10^{-6}\ C^{-1}$ ⊥ c-axis RT	$7.1 \times 10^{-6}\ C^{-1}$

*Oxygen ions in a hexagonal close packed arrangement.

*Aluminum ions occupy the octahedral interstices.

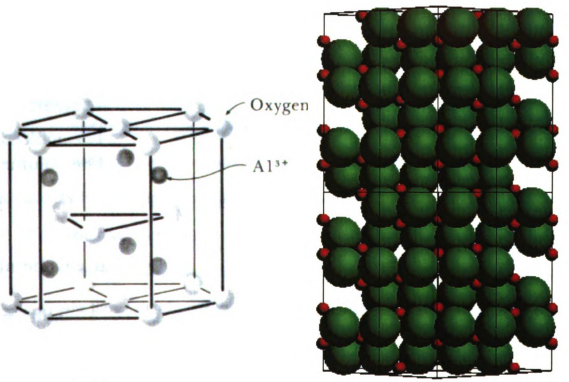

Figure 3.1 (a) A portion of the corundum cell and (b) atomic packing of a $(11\bar{2}0)$ plane of sapphire. One of the forms of alumina, Al_2O_3, has the corundum crystal structure, which is similar to a hexagonal close-packed structure. There are 12 Al ions and 18 O ions associated with each unit cell. The lattice parameters of alumina are a = 0.475 nm and c = 1.299 nm. The ionic radii of the Al^{3+} = 0.051 and the O^{2-} = 0.132. There are 6 Al_2O_3 groups with 12 Al ions and 18 O ions present in a hexagonal prism having the given lattice parameters.

3.2.1 Growth of Nb Film on Al_2O_3

Theoretically, growth and nucleation of Nb on sapphire should follow one of three basic growth modes. These three well-known modes are [23]:

1) The Volmer-Weber (VW) mode (island), which occurs when the smallest stable clusters nucleate on the substrate and grow in three-dimensions to form islands. The growth of islands is more common when there is stronger bonding between the deposited atoms than deposited atoms to the substrate.
2) The Frank-van der Merwe (FM) mode (layer-by-layer), which occurs when the smallest stable clusters nucleate on the substrate and grow in two dimensions to form a planar sheet (continuous layer). This type of growth mode occurs when there is strong bonding between the atoms and the substrate and is commonly seen in single crystal epitaxial growth of semiconductor films.
3) The Stranski-Krastanov (SK) mode (layer+ island): In SK growth mode, after the formation of a few monolayers (due to strong bounding between the atoms and the substrate), the surface energy changes and bonding between subsequent layers decreases with simultaneous increases in bonding between the atoms, resulting in three-dimension island formation.

Metal atoms typically do not wet insulating substrates and bond more strongly to each other. Due to this bonding, nucleation and growth of the metal on the insulator usually occurs in the VW (island formation) mode [24, 25]. When three-dimension islands form, the island size increases in three dimensions, until coalescence of the islands occurs, leading to a continuous film. If all of the islands grow with the same orientation or rotate

to the same orientation during coalescence, a single crystal will form. In practice, a number of factors affect the nucleation and growth of crystalline films. Among the most important factors are the nucleation rate, the substrate temperature, deposition rate, and the surface quality of the substrate or buffer layer [23].

The nucleation and growth of Nb(110) on the $Al_2O_3(11\bar{2}0)$ substrates seems to be unusual and different from the typical growth of metals on insulator substrates. Mayer et al. have shown that the $Al_2O_3(11\bar{2}0)$ surface is oxygen terminated and creates adsorption sites for the Nb atoms [11]. The results reported by a few other investigators indicate that a strong anisotropic bonding exists between Nb films and Al_2O_3 substrates, which is due to one adsorption per site for the Nb atoms in the first monolayer [15].

3.2.2 Grain Structure of Sputtered Metal Films

The temperature of the substrate and the argon pressure in the sputtering systems will affect both the sticking coefficient (the ratio of the number of atoms adhering to the number of atoms striking the substrate) and film structure. The structural morphologies of deposited films at different temperatures were described by Movchan et al. [26] using a zone structure model [23, 26]. In figure 3-2(a), the influence of both argon pressure and substrate temperature on microstructure of sputtered metallic film is shown [26]. In part (b) of this figure, four different zones as a function of temperature are illustrated [23]. In this figure, the horizontal axis is T_S/T_M where T_S is the substrate temperature and T_M is the melting temperature of the deposited metal.

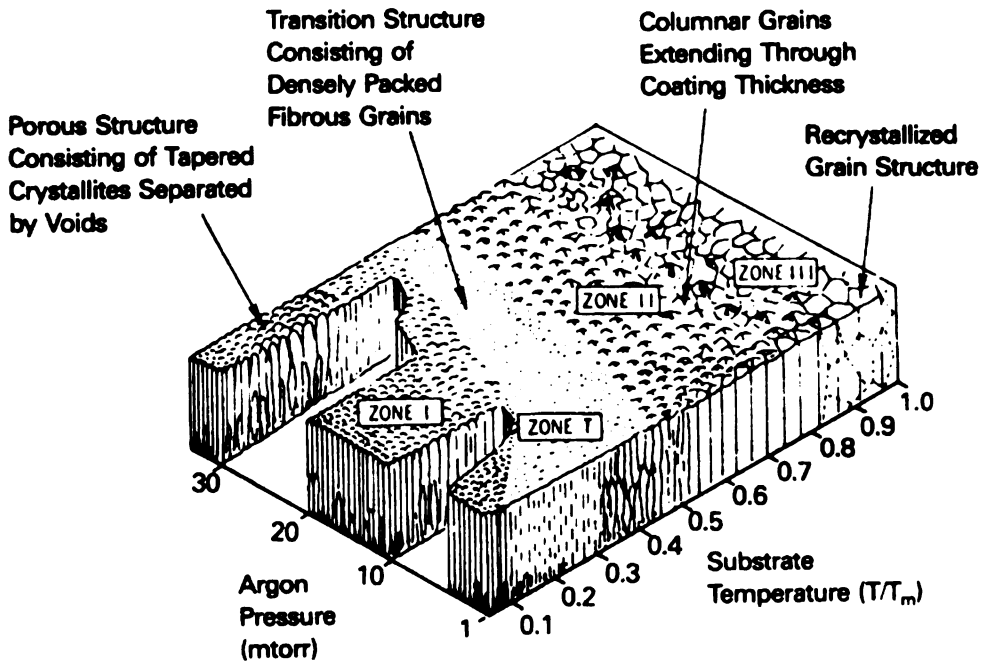

(a)

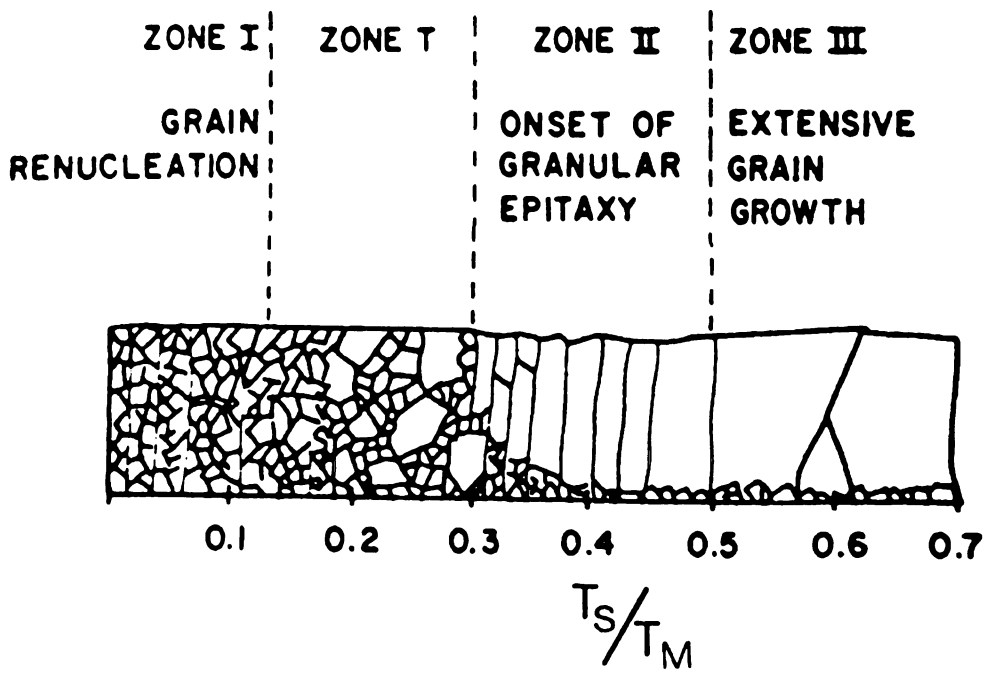

(b)

Figure 3.2 (a) Effect of argon pressure and substrate temperature on microstructure of sputtered metallic films (adopted from [26]). (b) Zone model for evaporated metal films (adopted from [26]).

3.3 RESULTS

3.3.1 Growth Process

As was described in section 2.3.2 the sapphire substrates used in the present study were pre-deposition annealed at 1200°C. Sputtering of the Nb films was carried out using substrate temperatures ranging from 25 to 1200°C. Surface smoothness of some of the sputtered films was improved by post-annealing the films at 950°C and 1100°C. All films were grown in 2.5×10^{-3} Torr Ar, with a chamber base pressure of $\sim1\times10^{-8}$ Torr and the deposition rate for Nb was 3 Å/s. A list of epitaxial Nb films is tabulated in appendix 3.A.

3.3.2 AFM Analyses

A series of 250 nm thick Nb films was grown on $Al_2O_3(11\bar{2}0)$ at different substrate temperatures. The surface topography of these films was imaged using a Digital Instruments atomic force microscope (AFM). In general, the quality and topography of sputtered Nb films grown on $Al_2O_3(11\bar{2}0)$ is affected by the substrate temperature. Figure 3.3 shows AFM images and line trace surface analyses of a Nb film grown at: (a) room temperature, (b) 450°C, (c) 660°C, (d) 750°C, and (e) 1100°C which illustrates the roughness of these films. Note that samples deposited at substrate temperatures of 450°C and higher were post deposition annealed at 1100°C for 10 minutes.

The samples deposited at ambient temperature (not annealed with $T_S/T_M = 0.01$) were characterized by a rough granular topography suggestive of a polycrystalline structure. The average size of the topographic futures (grains) in the Nb films grown at room temperature were approximately 125 nm x 50 nm. The image root-mean-square (RMS)

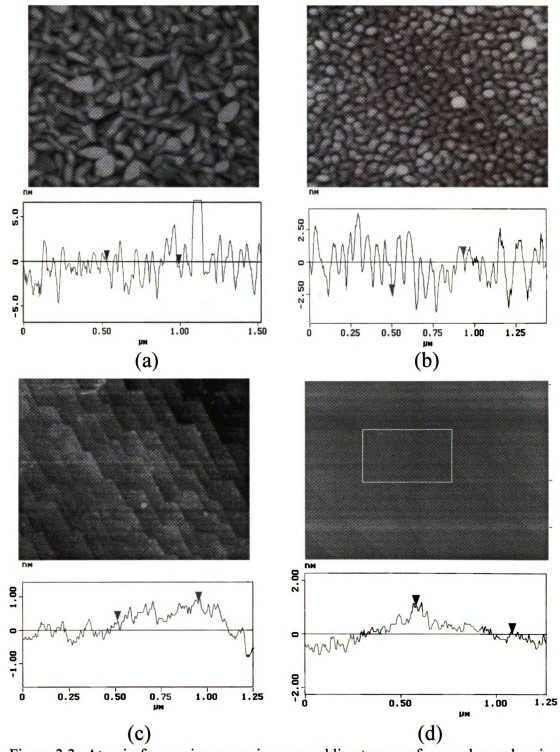

Figure 3.3 Atomic-force-microscopy images and line trace surface analyses showing the surface topography of Nb films deposited at substrate temperatures of 25°C (No PDA), 450°C (PDA=1100°C), 660°C (PDA =1100°C), and 750°C (PDA=1100°C), with image RMS roughness of 3.17, 2.52, 1.25, and 0.35 nm, respectively.
(PDA = Post Deposition Annealed)

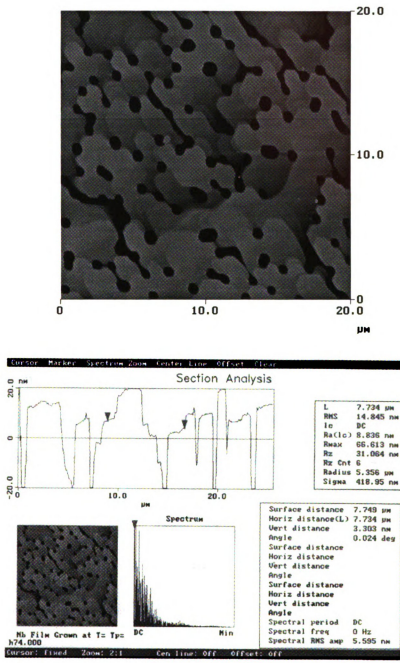

Figure 3.3(e) Atomic-force-microscopy images and line trace surface analyses showing the surface topography of Nb films deposited at substrate temperatures of 1100°C with image RMS roughness of 33.1 nm. The epitaxial Nb film grown at substrate temperature of 1100°C was found to be very rough, often containing many holes.

roughness was about 3.8 nm. Note that roughness measurements were performed over entire individual images and are referred to as image RMS roughness. The line traces in all AFM images are only representative of a single trace not the entire image.

At a substrate temperature of 450°C ($T_S/T_M = 0.18$), the surface topography suggested some alignment and possibly collimated grain formation. This could be due the post deposition annealing and a TEM cross-sectional study can clear up this issue. At this point, however, the effect of growth temperature seems to be the main factor, in agreement with zone T in Figure 3.2. The average topographic futures in this film varied from 45 to 55 nm with an image RMS roughness of 2.52 nm. At a substrate temperature of 660°C ($T_S/T_M = 0.26$), oriented steps, which may be structural ledges, run across the surface with an image RMS roughness of 1.25 nm. The steps have an average height of approximately 0.50 nm, equivalent to two (110) interplaner spacing of Nb ($\sqrt{2}$ x 0.331 nm = 0.47 nm). The misorientation (θ) in Figure 3.3(c) was calculated using the height of the structural ledges and number of them in one row within 1250 nm x 1250 nm scanned area:

$$8 \text{ (steps in 1250 nm length)} \times 0.5 = 4 \text{ nm}$$

$$\text{Sin}(\theta) = 4 \text{ nm} / 1250 \text{ nm} \quad \therefore \theta = 0.18 \text{ degrees}$$

This misorientation is most likely due to miscut in $Al_2O_3(11\bar{2}0)$.

At a substrate temperature of 750°C ($T_S/T_M = 0.3$), the surface topography appeared to be very smooth, free of any kind of grains and structural ledges (Figure 3.3(d)) resulting in an image RMS roughness of 0.35 nm. At a substrate temperature of 1100°C, the films were found to be very rough, containing many holes. Figure 3.3(e) shows an AFM image

and line trace surface analyses of a 250 nm thick film grown at a substrate temperature of 1100°C ($T_S/T_M = 0.46$). The image RMS roughness is about 33 nm.

As shown in Figure 3.3(f) a sample deposited at 750°C and post deposition-annealed at 950°C for 10 minutes had a better surface topography (smoothness) as a sample annealed at 1100°C. Therefore, a substrate temperature of 750°C with post deposition temperature of 950°C was chosen as an optimum growth temperature for Nb films used as a foundation for subsequent films grown in this study.

It should be noted that the optimal growth temperature for growing epitaxial films was proposed by Flynn [27] to be determined by the following empirical equation:

$$T_{\text{epitaxial growth}}(K) = (\frac{3}{8})\, T_{\text{melting temperature}}(K)$$

which results in $T_{\text{epitaxial growth}} = 755°C$ for growth of epitaxial Nb film. In practice, however, there are other factors such as growth technique and deposition rate that can affect the predicted growth temperature. The optimum growth temperature (750°C) of the epitaxial Nb in this study was very close to the predicted growth temperature

The AFM results for these films reveals only information about the surface morphology. The AFM results do not yield crystallographic information about the sputter deposited Nb films. To obtain information about the orientation and crystalline quality of these films, the EBSP technique was used.

3.3.3 EBSP Analyses

EBSP is very useful for characterizing the orientation of sputtered films. The patterns from the Nb films grown at a substrate temperature of 600°C or higher were very sharp

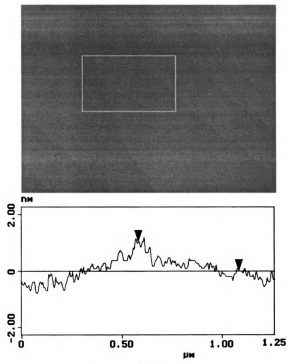

(a)

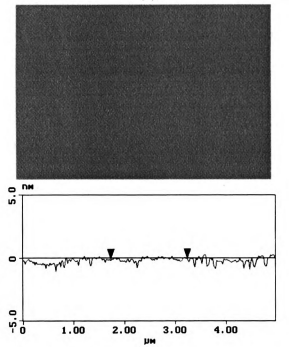

(b)

Figure 3.3(f) Atomic-force-microscopy images showing the surface topography of two Nb films deposited at substrate temperature of 750°C and post deposition annealed at (a) 1100°C and (b) 950°C with image RMS roughness of 0.35 and 0.16 nm, respectively.

and easily indexed as bcc. Due to the Nb thickness (t_{Nb} = 250 nm), the patterns did not suffer from contributions from the underlying Al_2O_3. Figure 3.4 shows representative EBSPs from Nb films. The patterns obtained from a Nb film grown at ambient temperature [Figure 3.4(a)] did not have any evidence of EBSP bands. This lack of Kikuchi bands along with the surface topography suggests that the grains in the deposited film are randomly oriented highly defective and this film is polycrystalline. At an ambient temperature, the growth directions of Nb islands were not influenced by substrate orientation (no substrate wetting). Patterns obtained from a sample grown at 450°C showed a weak signature of a few bands [Figure 3.4(b)]. This EBSP result and those of AFM surface topography, suggested that either the grains in this film are lightly textured, or all of them are collimated and have the same orientation (highly textured), but contain a lot of dislocations and/or other defects that cause strong pattern degradation. Electron backscatter diffraction patterns obtained from films grown at 660°C and 750°C were very sharp and are shown in figure 3.4(c & d). EBSP of the Nb film deposited at 1100°C was similar to those grown at 750°C. An EBSP obtained from one of these films (grown at 750°C) is shown before and after indexing in Figure 3.5.

Stage control scanning (controlled movement of the motorized specimen stage) was used to study and characterize the orientation distribution of Nb in the films grown at 750°C. Depending on the analysis, scan sizes ranged from 3 μm x 3 μm with 1 μm steps, to 1 mm x 1mm with 5μm steps. The resulting pole figures indicated that the entire film had the same orientation, within the 1° accuracy of the measurement [28]. Therefore, the films are epitaxial single crystals. The Nb films display normals of [110], which is consistent with the growth occurring on the closest packed {110} planes in the bcc Nb.

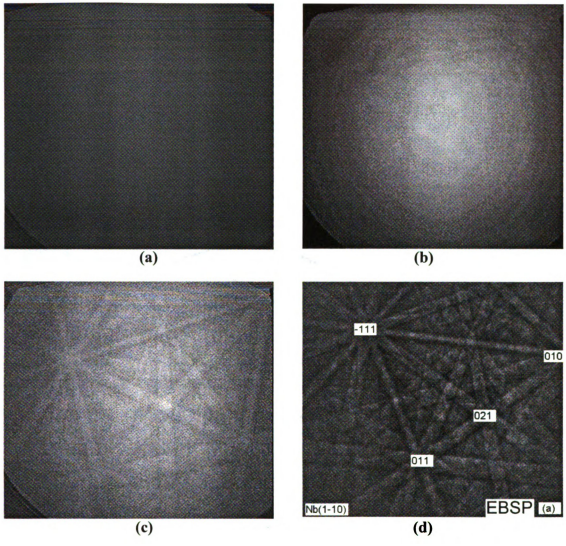

Figure 3.4 Electron backscatter pattern obtained from 250 nm Nb films grown onto (1 1 $\bar{2}$ 0)Al_2O_3 at a substrate temperature of : a) 25°C, b) 450°C, c) 650°C, d) 750°C.

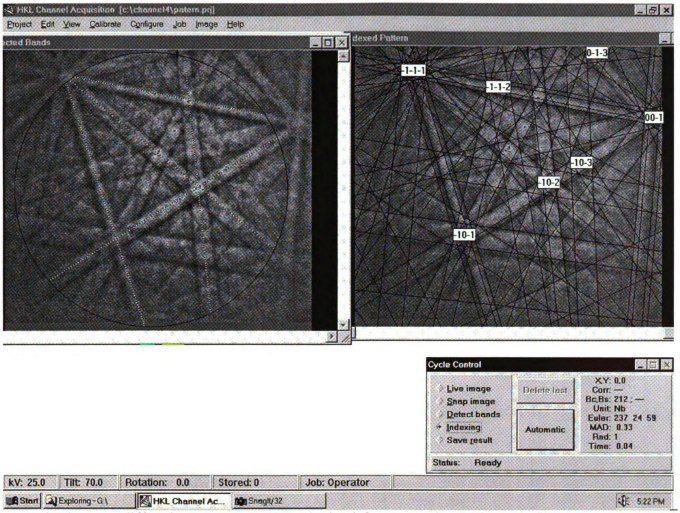

Figure 3.5 Electron backscatter diffraction pattern (EBSP) obtained from an epitaxial-bcc Nb film grown on (1 $\bar{1}$ 2 0) Al_2O_3 at a substrate temperature of 750°C. On left-hand side, a few bands were chosen automatically by software. On right-hand side the pattern were indexed.

3.3.4 Orientation Relationship Between Epitaxial Nb and Al_2O_3

EBSP generated pole figures of the bcc Nb and single crystal Al_2O_3 substrate were used to determine the epitaxial relationship between the sputtered Nb and substrate. Pole figures, which show the distribution of selected crystallographic directions in the sample relative to a given sample axis, were produced from the EBSP data. Pole figures of the epitaxial Nb film showing the distribution of <110>, <111>, and <100> poles are shown in Figure 3.6. These pole figures were then superimposed to create the stereographic projection for the epitaxial Nb film. Stereographic projections of the $(110)_{bcc}$Nb and $(11\bar{2}0)$ Al_2O_3, collected from the same sample (which had a small portion of the substrate masked during sputtering), are shown in Figure 3.7. The epitaxial relationship between Nb and Al_2O_3 was found to be $(1\bar{1}0)_{bcc}$Nb || $(11\bar{2}0)_{hcp}$ Al_2O_3 with $[111]_{bcc}$Nb || $[0001]_{hcp}Al_2O_3$, which agrees with HREM observations [11,12,19]. Generally, the epitaxial relationships determined using EBSP should be significantly more accurate (within ~1°) than those deduced from HREM, where structural images can be obtained when samples are tilted significantly off-axis leading to inaccuracies up to 4° [30]. In the epitaxial Nb films deposited for this study, the resulting pole-figure data from adjacent sections of Nb and Al_2O_3 did not also reveal any misorientation (within the accuracy of the measurement).

Pole Figure of an Epitaxial Nb Film

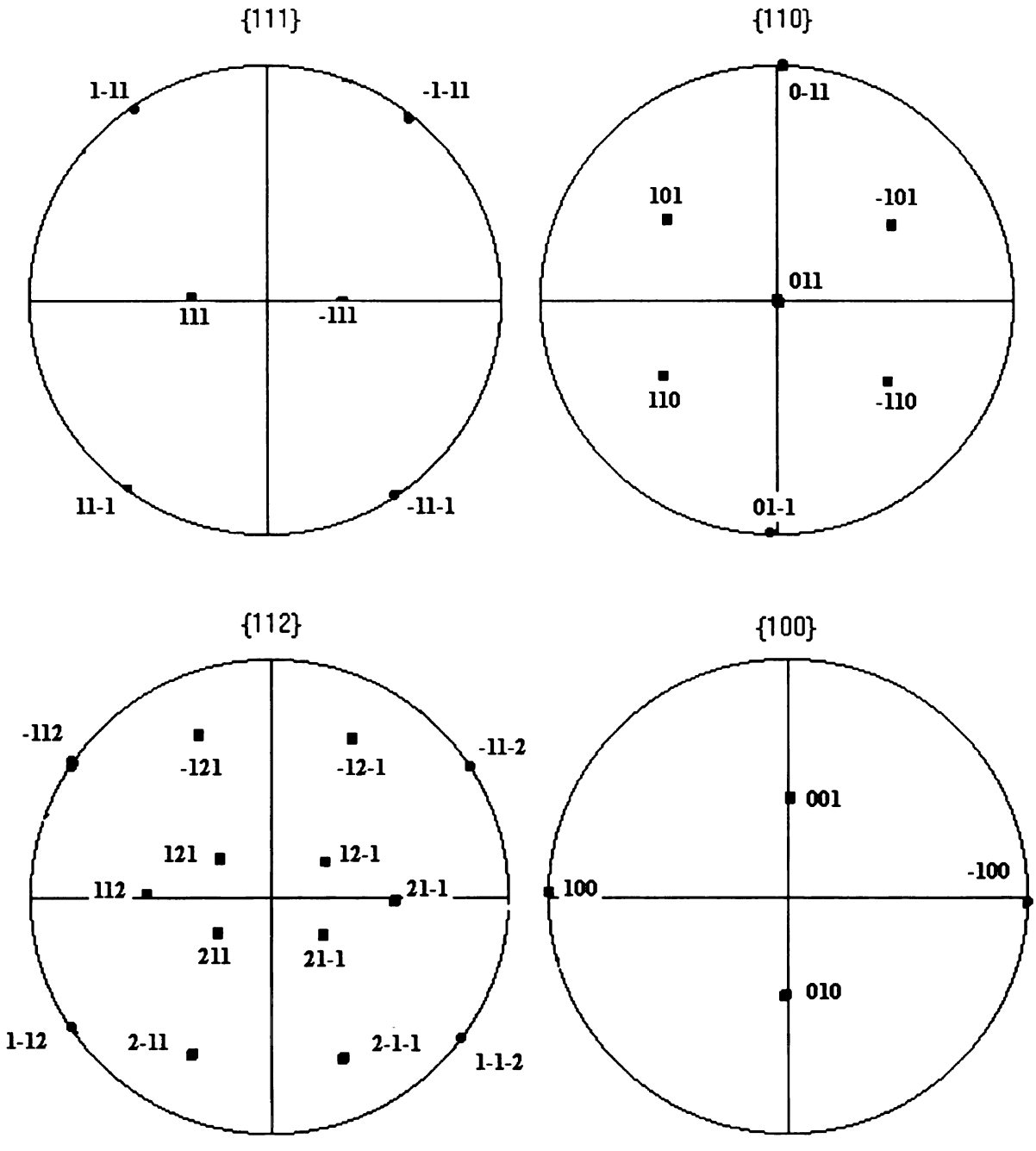

Figure 3.6 Pole figures of the epitaxial Nb film showing the distribution of <110>, <111>, <112>, and <100> poles.

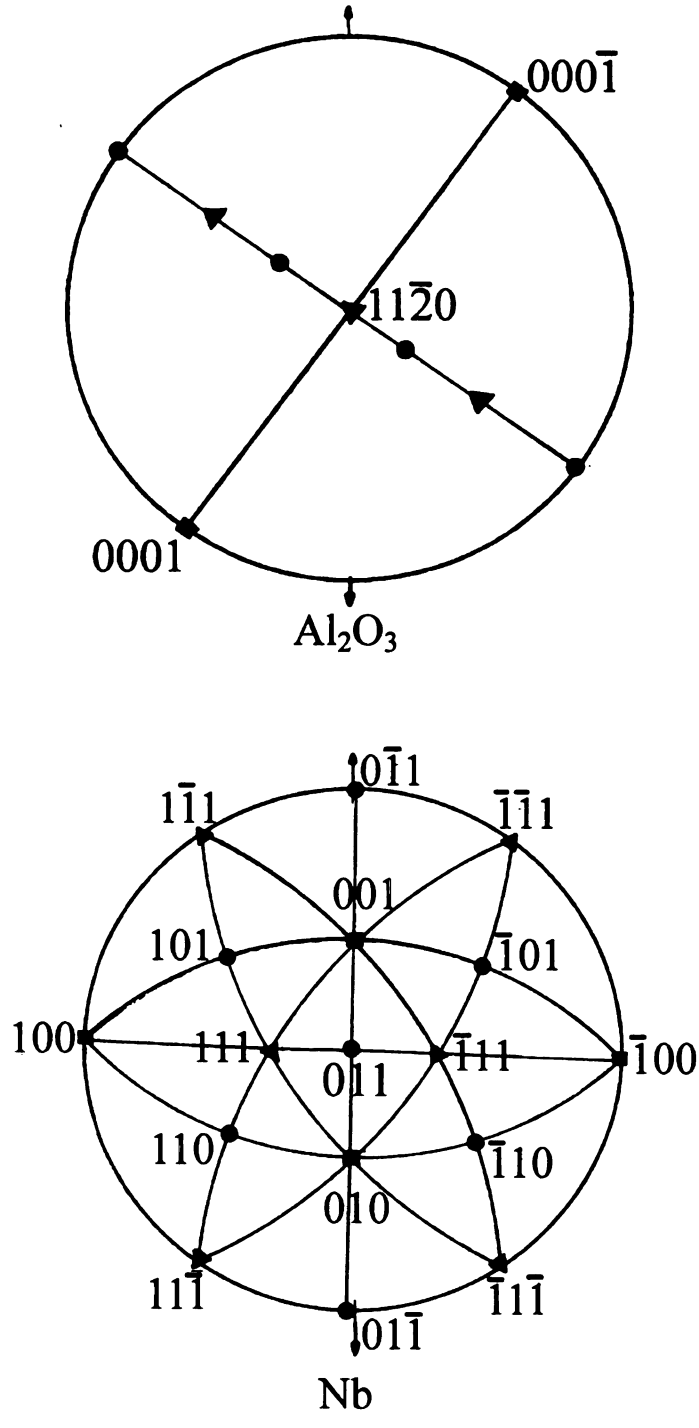

Figure 3.7. Stereographic projections of the epitaxial Nb film and sapphire substrate showing the epitaxial relationship between the Nb films and Al_2O_3 substrates is $(1\ \bar{1}0)_{bcc}Nb\ ||(1\ 1\ \bar{2}\ 0)_{hcp}Al_2O_3$ with $[111]_{bcc}Nb\ ||[0001]_{hcp}Al_2O_3$.

3.4 DISCUSSION

In general the results of AFM and EBSP suggests that in the sample grown at an ambient temperature there are strong bonding between Nb atoms and they form a granular polycrystalline film. At temperature of 450°C, there must be better bonding (compared with those grown at an ambient temperature) between the Nb atoms and the substrate (better surface topography and weak appearance of some Kikuchi bands). Therefore, the Nb islands could have grown in a partially preferred orientation, without any significant coalescence between the Nb islands (not enough thermal energy for atoms to move around). However, the possibility of partial effect from post deposition annealing at 1100°C can not be ruled out. At higher temperature, in particular at 750°C, a very smooth surface topography and well defined Kikuchi bands suggests a strong bonding between Nb film (atoms) and Al_2O_3 substrate in agreement with predicted growth mode [15, 23].

3.5 SUMMARY

In this chapter the growth and structural characterization of sputter deposited Nb films on $(11\bar{2}0)_{hcp}$ Al_2O_3 substrate using AFM and EBSP have been discussed. Nb films deposited at ambient temperature without post deposition annealing were characterized by a rough granular topography, suggestive of a polycrystalline structure. For those deposited at a substrate temperature of 450°C and post deposition annealed at 1100°C, the surface topography suggested some alignment and possibly collimated grain. At a substrate temperature of 660°C post deposition annealed at 1100°C, oriented steps, which may be structural ledges, run across the surface. The optimum growth temperature was

found to be 750°C with post deposition annealing at 950°C. EBSP and AFM results revealed that the Nb films deposited at 750°C grow as $(110)_{bcc}$ single crystals with a very smooth surface topography of about ~0.2 nm. It has been shown that bcc Nb(110) planes can be grown epitaxially on Al_2O_3 $(11\bar{2}0)$ substrates. The in plane epitaxial relationships were:

$$[0001]Al_2O_3 \parallel [111]Nb$$

and

$$[1010]Al_2O_3 \parallel [121]Nb.$$

Appendix 3.A

Summary of Sputtered Nb Films

Run # / Sample #	Predeposition annealing Temperature	Growth Temperature / Post deposition Annealing Temperature
7-1	1200°C	750°C / 1100°C
7-2	1200°C	660°C / 1100°C
7-3	1200°C	450°C / 1100°C
7-4	1200°C	1100°C / 1100°C
7-6	None	Room Temperature
8-6	1200°C	760°C / 1110°C
11-1	1200°C	765°C / 950°C
12-2	1200°C	750°C / 950°C
17-1	1200°C	750°C / 950°C
35-3	1200°C	750°C / 950°C

All substrates were Al_2O_3 $(11\bar{2}0)$.

Deposition rate = 3 Å/s

Deposition pressure = 1-2.5 x 10^{-3} torr.

3.6 REFERENCES

1) W. P. Pratt Jr., S.F. Lee, J.M. Slaughter, R. Loloee, P.A. Schroeder, and J. Bass, Phys. Rev. Lett. **66**, 3060 (1991).

2) S. M. Durbin, J. E. Cunningham, M. E. Mochel, and C. P. Flynn, J. Phys.:Met. Phys., **11**, L223 (1981).

3) S. M. Durbin, J. E. Cunningham, and C. P. Flynn, J. Phys.:Met. Phys., **12**, L75 (1982).

4) R. E. Somekh and C. S. Baxter, J. Cryst. Growth, **76**, 119 (1986).

5) J. Kwo, M. Hong, and S. Nakahara, Appl. Phys. Lett., **49**, 319 (1986).

6) K. Burger, W. Mader, and M. Rühle, Ultramicroscopy, **22**, 1 (1987).

7) W. Mader and M. Rühle, Act. Met., **37**, 853 (1989).

8) M. Kuwabara and J. C. H. Spence, J. Mater. Res., **4**, 972 (1989).

9) J. Mayer, C. P. Flynn, and M. Rühle, Ultramicroscopy, **33**, 51 (1990).

10) C. H. Lee and K. S. Liang, Acta Metall. Mater., **40**, S143 (1992).

11) J. Mayer, G. Gutekunst, G. Möbus, J. Dura, C. P. Flynn, and M. Rühle, Acta Metall. Mater., **40**, S217 (1992).

12) D. X. Li, P. Pirouz, A. H. Heuer, S. Yadavalli, and C. P. Flynn, Acta Metall. Mater., **40**, S237 (1992).

13) P. M. Reimer, H. Zabel, C. P. Flynn, and J. A. Dura, Phys. Rev. B, **45**, 11426 (1992).

14) T. Wagner, M. Lorenz, and M. Rühle, J. Mater. Res., **11**, 1255 (1996).

15) G. Song, A. Remhof, K. Theis-Bröhl, and H. Zabel, Phys. Rev. Lett., **79**, 5062 (1997).

16) G. Gutekunst, J. Mayer, and M. Rühle, Phil. Mag. A, **75**, 1329 (1997).

17) G. Gutekunst, J. Mayer, V. Vitek, and M. Rühle, Phil. Mag. A, **75**, 1357 (1997).

18) M. Wagner, T. Wagner, D. L. Carroll, J. Marien, D. A. Bonnell, and M. Rühle, MRS Bulletin, **42** (1997).

19) T. Wagner, J. Mater. Res., **13**, 693 (1998).

20) B. Wölfing, K. Theis-Bröhl, C. Sutter, and H. Zabel, J. Phys.: Condens. Matter, **11**, 2669 (1999).

21) D. R. Askeland, The Science and Engineering of materials, PWS-Kent publishing Co. Boston page 459 (1989).

22) EMS On Line, Center Interdepartmental de Microscoie Electronic, EPFT, Lausanne. Pierre-Henri Jouneau and Pierre Stadelmann. http://cimesg1.epfl.ch/CIOLS/.

23) M. Ohering, The Materials Science of Thin Films, Academic Press In., San Diago, (1992).

24) E. Bauer, Z. Kristallogr. **110**, 423 (1958).

25) J. H. v. d. Merwe, Interf. Sci. **1**, 77 (1993).

26) R. J. Hill, Physical Vapor Deposition, Temescal, Ca, Page 144 (1986). B.A. Movchen and A. V. Demchishin, Phys. Met. Metallogr. **28**. 83 (1969). H. T. G. hentzell, C. R. M. Grovenor, and D. A. Smith, J. Vac. Sci. Tech. **A2**, 218 (1984). J. A. Thornton, Ann. Rev. mater. Sci. **7**, 239 (1977).

27) C. P. Flynn, J. Phys. F: Met. Phys., **18** L195 (1988).

28) B.D. Cullity, Elements of X-Ray Diffraction Addison-Wesley, Reading Massachusetts, Second edition (1978).

29) S. I. Wright, J. Computer-Assisted Microscopy, **5**, 207 (1993).

30) H. Geng, J. W. Heckman, W. P . Pratt Jr., J. Bass, J. F. Espinosa, S. D. Conradson, D. Lederman, and M. A. Crimp, J. Appl. Phys., **86**, 4166 (1999).

CHAPTER 4

GROWTH OF Cu FILMS ON EPITAXIAL Nb

4.1 INTRODUCTION

In the growth process of typical CPP magnetic multilayers or spin valves, a thin layer (10-20 nm) of Cu film must be first deposited on the Nb contact layer. The presence of the Cu layer eliminates the reaction between the Co or Py layer with the Nb contact layer [1]. In the growth of epitaxial magnetic systems, this Cu layer has an additional role; it is the foundation for growing epitaxial multilayers and spin valves in a preferred orientation.

A series of Cu films with different thickness (20-300 nm) were grown on 250 nm thick epitaxial Nb films at several substrate temperatures. As described in Chapter 3, high quality epitaxial single crystal $(1\bar{1}0)$ Nb films have been grown on $(11\bar{2}0)$ sapphire substrates at an optimum temperature of 750°C (post deposition annealed at 950°C) using dc magnetron sputtering. A list of the epitaxial Cu films grown in this study is given in appendix 4.A.

In the past, researchers have used various fabrication techniques, such as MBE and sputter deposition, to grow epitaxial Cu films [2-24]. Most of the epitaxial Cu films fabricated using MBE and sputter deposition systems were grown on Nb substrates, using substrate temperatures between 150°C and 350°C.

In this chapter, background information on the nucleation and the growth of fcc materials (i.e. Cu) on bcc materials (i.e. Nb), including the epitaxial relationships between bcc and fcc, twinning in (111)fcc metals, and twin boundaries, are discussed.

This chapter includes a detailed explanation of sputter deposition of Cu films on epitaxial Nb. Also included are the results of AFM and EBSP characterization of the sputter-deposited Cu films (grown at 350°C, 150°C, and 90°C). A discussion of the growth process in sputter deposited films, based on the AFM and EBSP analysis, concludes this chapter.

4.2 BACKGROUND: NUCLEATION AND GROWTH

The crystallography and physical properties of Nb and Cu are well-known. Crystallographic data for both Nb and Cu are summarized in Table 4-1.

The nucleation and growth of Cu on epitaxial Nb differs from the epitaxial growth of Nb on Al_2O_3. In the Cu/Nb case, the surface free energies of the substrate, interface, and overlayer are important factors that determine the growth mode (Three possible growth modes, Volmer-Weber (VW), Frank-van der Merwe (FM), and Stranski-Krastanov (SK) were described in Chapter 3). Details of the growth modes for metal/metal materials have been discussed by Bauer and van der Merwe [3].

Theoretically, the free energies (γ) of the growing surface and substrate and the interface between the substrate and growing material play dominant roles in determining the growth mode. For example, if the surface energy of the substrate is greater than the growing overlayer surface energy, that is if $\gamma_s \geq \gamma_{fn} + \gamma_{in'}$, then the FM growth mode (layer by layer) will occur. In this growth mode γ_{fn}, $\gamma_{in'}$, and γ_s are the surface energy of the overlayer film (thickness = n), the surface energy of the interface (thickness = n'), and the surface energy of the substrate, respectively [24].

Table 4-1

CRYSTALLOGRAPHIC DATA FOR Nb AND Cu

Element name:	Nb–Niobium-Columbium	Cu-Copper
Crystal system:	Cubic – bcc	Cubic – fcc
a =	0.33067 nm	0.36148 nm
Unit cell volume:	0.0359 nm^3	0.0467 nm^3
# of atoms in unit cell:	2	4
Atomic radius:	Nb = 0.143 nm	Cu = 0.128 nm
$d_{(h,k,l)}$	$d_{(110)}$ = 0.2337 nm	$d_{(111)}$ = 0.2078 nm
Symmetry elements:	Four 3-fold rotation axes	Four 3-fold rotation axes
Melting point:	2469 °C	1083 °C

There are two basic conditions for growing epitaxial films. a) The surface energies of the two metals (overlayer and substrate) must be compatible. b) There must be only one crystallographic orientation relationship between the film and the substrate. It will be shown that the Nb and Cu can satisfy these requirements. Table 4-2, lists the surface energies for some metals and insulators.

4.2.1 Orientation Relationship Between fcc and bcc: A (110) bcc plane contains two <111> directions ($\bar{1}\,1\,\bar{1}$ and $1\,1\,\bar{1}$: close-packed directions), one <100> direction, and one <011> direction. A (111) fcc plane contains three <110> directions (110, 101, and 011: close-packed directions) and three <112> directions (112, 121, and 211). The epitaxial relationships between bcc and fcc materials were originally studied in the early 1930s [25-27]. Nishiyama and Wasserman independently showed that one of the possible atomic arrangements between $(110)_{bcc} \parallel (111)_{fcc}$, is $[1\,\bar{1}\,0]_{bcc} \parallel [1\,\bar{1}\,2]_{fcc}$, which also results in $[\bar{1}\,0\,0]_{bcc} \parallel [0\,1\,\bar{1}]_{fcc}$ (this will be referred to as the NW relationship) [25, 26]. Kurdjumov and Sachs showed another atomic arrangement between $(110)_{bcc} \parallel (111)_{fcc}$, with $[1\,\bar{1}\,1]_{bcc} \parallel [0\,1\,\bar{1}]_{fcc}$ (the KS relationship) [27]. Figure 4.1 shows the atomic arrangements of both the NW and KS relationships. These two relationships differ by 5.26° on the $(110)_{bcc} \parallel (111)_{fcc}$ planes. The orientation relationship can actually vary continuously from the NW to the KS to again the NW as r ($r = a_{bcc}/a_{fcc}$) increases from 0.70 to 0.86 [6]. The NW relationship has been reported to be the most common in (110)Nb/(111)Cu cases [2, 3, 6, 28].

To observe the geometrical NW relationship between $(110)_{bcc}$Nb and $(111)_{fcc}$Cu, the atomic arrangements of these two planes (see Figure 4.2 (a), (b)) have been superimposed

in the NW orientation relationship. The result of this superposition is shown in Figure 4.2 (c). The two alignments directions Cu[101] || Nb[100] and Cu[$1\bar{1}2$] || Nb[$\bar{1}10$], are labeled. Observe that none of the close-packed directions aligns with each other. The areas where Cu atoms coincide with Nb atoms appear in the diamond-shaped area and form a broad band along the $[100]_{bcc}$ and $[011]_{fcc}$ (see A and B in Figure 4-2(c)).

Table 4-2

SURFACE ENERGY OF SELECTED ELEMENTS AND MATERIALS

Transition metal	Ti	V	Nb	Mo	Ru	Rh	Pd	Ta	W	Pt	
	2.6	2.9	3.0	2.9	3.4	2.8	2.0	3.0	3.5	2.7	J/m^2
Noble metal	Al	Ag	Cu	Au							
	1.1	1.3	1.9	1.6	J/m^2						
Magnetic metal	Cr	Mn	Co	Fe	Ni	Gd					
	2.1	1.4	2.7	2.9	2.5	0.9	J/m^2				
Semiconductors	Diamond			Si	Ge	GaP	GaAs				
	1.7			1.2	1.1	1.9	0.9	J/m^2			
Insulator	LiF		Al_2O_3	CaF_2	MgO	NaCl					
	0.34		1.4	0.45	1.2	0.3	J/m^2				

Note that these are approximate values, which are difficult to measure and depend on surface orientation and reconstruction [24].

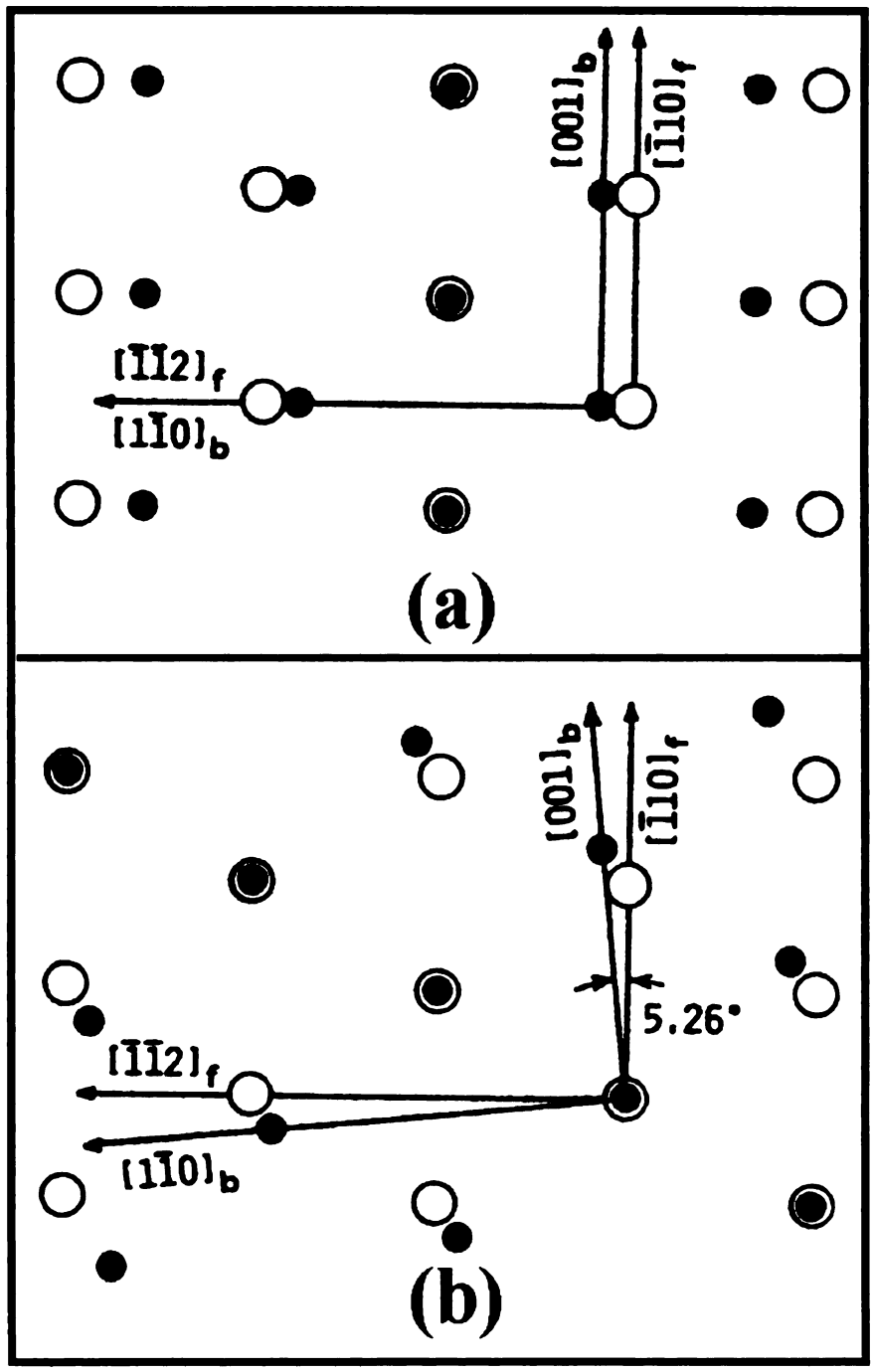

Figure 4.1 Atomic arrangement of the (a) NW and (b) KS (θ = 5.26°) relationships. With ●, atoms on $(110)_{bcc}$ and ○, atoms on $(111)_{fcc}$ [6].

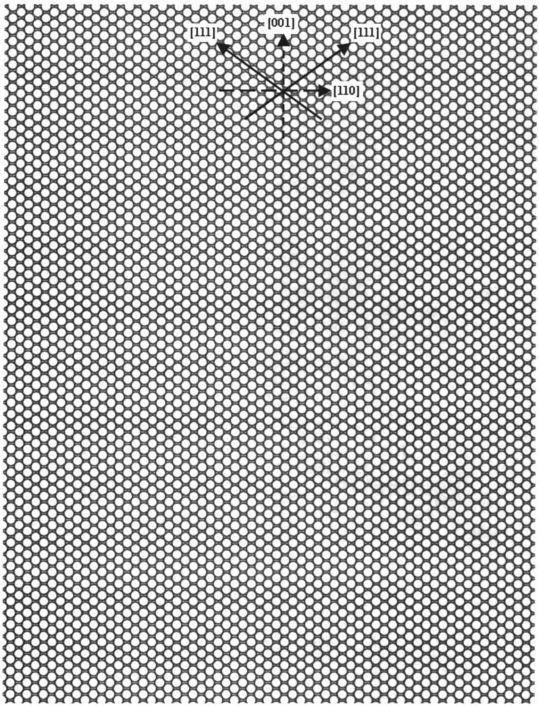

Figure 4.2 (a) Atomic arrangement of bcc Nb (110). The atomic radius of Nb is 0.143 nm with $d_{(110)} = 0.2337$ nm

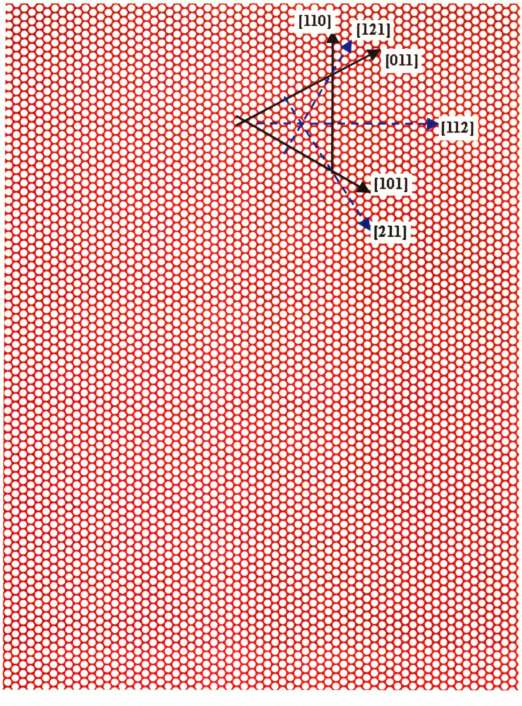

Figure 4.2 (b). Atomic arrangement of fcc Cu (111). The atomic radius of Cu is 0.128 nm with $d_{(111)} = 0.2078$ nm.

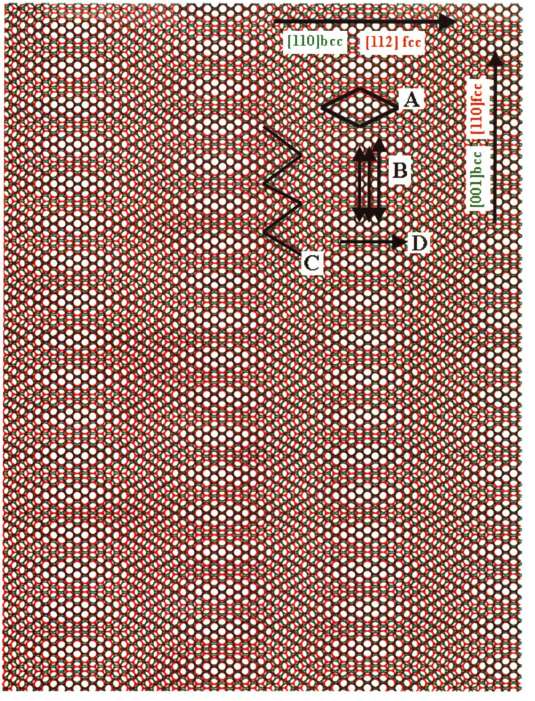

Figure 4-2(c) Unrelaxed overlaps of Cu(111) on Nb(110) in the N-W orientation relationship (Cu[101] || Nb[100]). For simplicity, perfect (defect free) Nb and Cu layers are assumed.

These diamond-shaped areas have higher energy compared with other areas and are unfavorable areas for nucleation. The regions between the diamond-shaped areas form zig-zag fringes (see C on the figure). In these areas, the Cu atoms sit in or near the troughs (valleys) between three Nb atoms (good atomic matching = favorable areas for nucleation). There are also fringes formed between the corner of these diamonds, parallel to $[110]_{bcc}$ and $[112]_{fcc}$ direction (see D on figure 4.2 (c)) with relatively good atomic matching.

In Figure 4-2 (d), the Nb and Cu planes (Figure 4.2 (a), (b)) have been superimposed in the KS orientation relationship for comparison to the NW orientation relationship. Similar to the NW orientation relationship, the diamond-shaped areas are unfavorable areas for nucleation. In both cases the fringe patterns are created due to existence of misfit dislocations (edge, screw, and mixed dislocations) [6, 28]. However, there are more misfit dislocations per unit area ($\therefore$ higher misfit strain energy) in an epitaxial film with the KS orientation relationship than those with the NW orientation relationship (same epitaxed metal pair: see 4 c&d). Bruce and Jaeger [28] have shown that favorable epitaxial relationships are those having a smaller misfit strain energy ($\therefore$ fewer misfit dislocations per unit area). In (111)fcc / (110)bcc (similar to (111)Cu on (110)Nb) epitaxed metal pairs, the NW orientation relationship is generally favorable over the KS orientation relationship.

4.2.2 Nucleation: The nucleation and growth of fcc materials on bcc substrates have been investigated by many researchers [2, 3, 6, 28]. However, the epitaxial nucleation of fcc thin films on bcc substrates is not well understood. Bauer and van der Merwe [3],

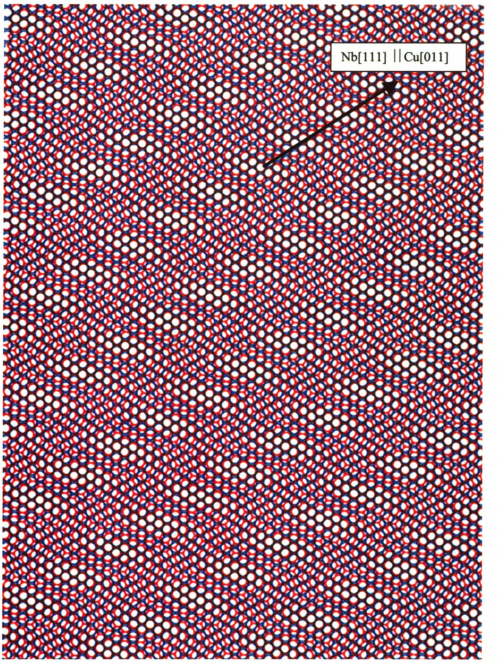

Figure 4-2 (d) Unrelaxed overlaps of Cu(111) on Nb(110) with consideration of K-S relationship (Cu[011] || Nb[111]).

have theoretically predicted that at elevated temperatures (in structures similar to Nb/Cu), the first (and possibly second) Cu layers grow pseudomorphically, aligning exactly with the top Nb layer. Starting with the second or third layer, the atomic distributions of Cu are similar to the (111)fcc plane with the NW orientation relationship [3]. From the third layer, three-dimensional (3-D) nucleation occurs within the SK growth mode (layer + island) [3]. At room temperature, quasi-FM (layer by layer) growth has been experimentally observed and reported [3, 29].

In the SK growth mode (at elevated temperature), formation of coherent (dislocation free) islands are energetically favored over incoherent (dislocated) islands [28]. These coherent islands are lattice-matched near their bases, but are largely strain-relieved near their top and sidewalls. Further deposition leads to the growth of islands and eventual coalescence to a continuance film [30]. Theoretical work by Drucker et al. [31] reported that coherent islands are energetically favorable up to a critical size (<100 nm). Further growth of these islands can cause a coherent-to-incoherent transition via the introduction of misfit dislocations.

4.2.3 Twin Formation: In the growth of fcc(111) metals on bcc(110) metals, formation of twins within the fcc(111) layer is a common phenomenon and has been reported by many researchers [3, 8, 9, 23, 32]. As was discussed in the pervious section, the first fcc(111) layer (i.e. Cu(111)) grows pseudomorphically on the top bcc(110) (i.e. Nb(110)) layer, then starting with the second or third layer, the atomic distributions of Cu are similar to the (111) plane [3]. This first fcc(111) Cu layer becomes a buffer layer for arriving Cu atoms. The formation of twins will take place on the top of this fcc(111) Cu

layer. The formation of twins in Cu(111) was observed using scanning tunneling microscopey (STM) [13, 15], which showed that the Cu(111) coherent islands form at one of two possible three-fold sites [12, 15, 22]. One of these three-fold islands follows the correct stacking (ABCABC) while the second island forms a different stacking (ACBACB). Schematic representaions of the side and top views of the stacking sequence (twins) are shown in Figure 4-3.

The orientation relation between the Cu(111) twins and the Nb substrate is the NW orientation [3]. Upon further film growth, no additional twin orientations form. This is due to the fact that the rotation angle is a rational multiple of 2π [3]. The presence of two variant twin morphologies in crystalline superlattices (such as Cu/Mo, Cu/Nb) has been discussed theoretically by Bauer and van der Merwe [3]. These twins have also been experimentally observed by a number of researchers in MBE or sputter deposited Co/Cu(111) multilayers using XRD, LEED, STM, and HREM [8, 12, 15, 19, 23, 31]. These papers, however, do not report on the distribution and size of twins in the epitaxial Cu films.

4.2.4 Nature of Twin Boundaries: To study boundaries between the two twin variants in epitaxial Cu films, high-resolution transmission electron microscopy is required. This requirement is beyond the scope of this study; however, there have been theoretical and experimental studies on twin grain boundaries in copper [33-36]. These studies will be used in this section to illustrate the relationships between twin and grain boundaries. Twinning is intrinsic to the growth of fcc(111) Cu and occurs with $\Sigma = 3$ coincidence-site lattice (CSL) orientation. The twin boundaries that form during growth can be

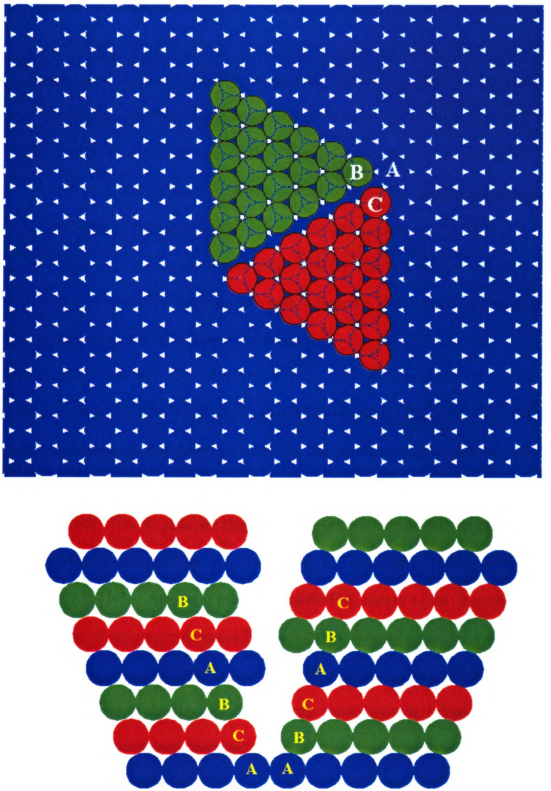

Figure 4.3 Schematic representations showing top and side views of the stacking sequences (twins) in (111) fcc.

categorized into three groups [33]:

a) Coherent twin boundary (CTB): The grain boundaries align themselves with a common {111} plane of both grains. These are relatively low interface energy (~ 0.022Jm^{-2}) boundaries with no mobility.

b) Incoherent twin boundary (ITB): The grain boundaries are not parallel to any {111} plane in either adjacent grains. This is an incoherent Σ(3) twin boundary. The interface film energy of an ITB is around 0.5 Jm^{-2}.

c) Symmetric incoherent twin boundary (SITB): This is a special case where the grain boundary plane coincides with a common {211} plane of both grains. The energy of SITB is around 0.84 Jm^{-2}.

Medlin et al. [36] have investigated the nature of twin boundaries in copper by depositing epitaxial Cu films on a single crystal Cu substrates. The results showed that the twin boundaries in this homo-epitaxial Cu are incoherent Σ(3) twin boundaries. However, the boundaries are complex, containing nanometer (1.4 to 3 nm) thick slabs with 9R stacking. The 9R slabs are rhombohedral, generated from the fcc structures by creating an intrinsic fault on every 3rd {111} plane. This produces a stacking sequence of ABC-BCA-CAB [34]. Atomistic models and HRTEM images of the incoherent Σ(3) twin boundaries of copper are shown in Figure 4.4 [36]. The 9R structure is very fragile and defects in the form of stacking faults can be generated during HRTEM observation.

The above review of the fundamental concepts should provide a foundation for the understanding of experimental characterization and the results obtained from AFM and EBSP characterization analysis.

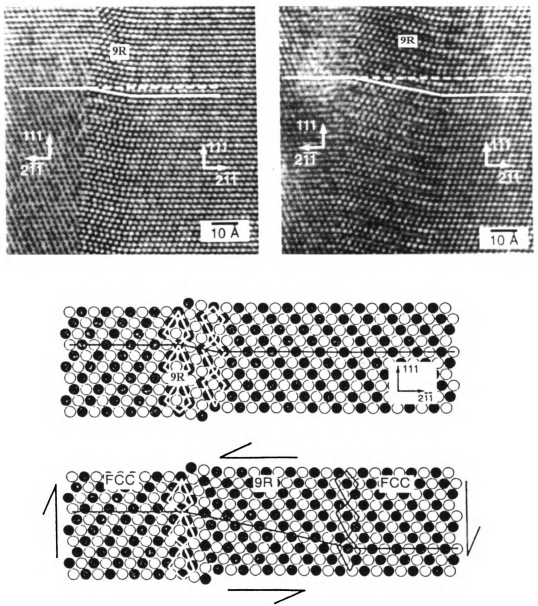

Figure 4.4 a) HRTEM images of incoherent Σ(3) twin boundaries in Cu, imaged along [011]. The 9R stacking faults are labeled, containing four or five layer defects. b) Embedded atom method atomistic simulations of the structure of the Cu boundaries [36].

4.3 SPUTTER DEPOSITION OF Cu FILMS

As described in the Chapter 2, the high temperature heater was removed after post deposition annealing of the Nb contact layer to cool the substrate to desired temperatures (90°C - 350°C). Meanwhile, the low temperature heater was warmed-up to the desired deposition temperature and mounted on the substrate. Typically, the heater switching processes took approximately 10 minutes. After the target deposition temperature was achieved, the Cu film was deposited.

4.4 RESULTS

4.4.1 AFM Analysis

Cu samples with film thicknesses ranging from 20 nm to 300 nm were grown on 250 nm of epitaxial Nb at substrate temperatures of 90°C, 150°C, and 350°C. The majority of the Cu films were subsequently post deposition annealed at 350°C, with a few annealed at 250°C and 500°C. The surface topography of each film was examined using AFM. Note that the surface topography measurement is a confusing issue and depends how one will defines a roughness. The following are examples of different kinds of surface roughnesses:

a) Small grains (islands) with shallow terraces.

b) Small grains (islands) with deep terraces.

c) Large grains (islands) with shallow terraces.

d) Large grains (islands) with deep terraces.

There are two parameters in the given examples; depth of terraces and size of grains (islands). If the depth of terraces is the important parameter, then the Root Mean Square

(RMS) Roughness, which is the standard deviation of the Z (Height) values, becomes the critical parameter (see Appendix 4.B). In this study, while the image RMS roughnesses for all samples have been measured, the sizes of grains (or islands) and the depth of terraces have also been considered for defining a surface roughness. For example, in case of having two surfaces with similar depth terraces but different island size, the surface with smaller size islands will be considered rougher.

In general, the growth temperature, film thickness, deposition rate, and substrate topography affected the morphology of the sputtered Cu films. The results of AFM analysis are categorized as follows:

- Surface topography of the as-grown samples.
- Effect of post deposition annealing on the film surface topography.
- Effect of film thickness on the film surface topography.
- Effect of deposition rates on the film surface topography.
- Effect of deposition techniques on the film surface topography.

4.4.1.1 As-Grown Cu Films

The as-grown films consisted of eighteen Cu films which were grown at 90°C, 150°C, 350°C, 400°C, and 475°C. Selected AFM results from these films are categorized as a function of film thickness.

300 nm thick samples: AFM images and line trace surface analyses of 300 nm thick Cu films grown at 90°C, 150°C, and 350°C are shown in Figure 4.5. The image RMS roughness in images a, b, and c are about 4, 4.5, and 20 nm, respectively. The Cu film grown at 90°C has a very granular appearance, suggesting small collimated islands

The Effect of Deposition Temperature on Surface Topography of
300 nm Thick Cu Films as Grown at 25°C, 150°C, 350°C.

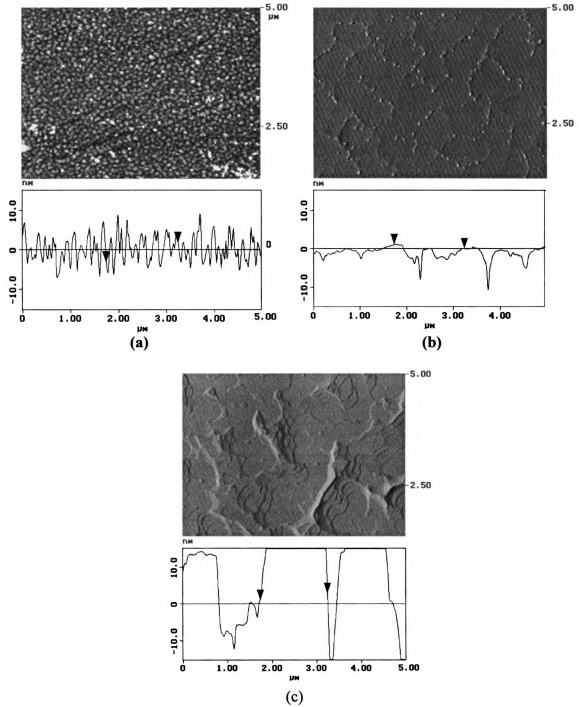

Figure 4.5 Atomic force-microscopy images and line trace surface analyses showing the surface topography of 300 nm thick Cu films deposited onto 20 nm thick Nb film at substrate temperatures of a) 25°C, b) 150°, and c) 350°C. The line trace surface analyses shows the image RMS roughness are about 4, 4.5, and 20 nm, respectively.

(~ 80 nm) in this film. At higher temperatures, the films have different surface profiles. Smoother surfaces are observed, but some deep troughs exist, suggestive of better coalescence of islands (than those grown at lower temperature) and formation of large size islands on the surfaces of these films.

150 nm thick samples. Three Cu films with a thickness of 150 nm were compared. These films were deposited at substrate temperatures of 150°C, 350°C, 475°C on 250 nm thick epitaxial Nb. AFM images and line trace surface analyses of these Cu films are shown in Figure 4.6. The image RMS roughness of these films are 1.3, 23.3, and 2.6 nm, respectively. It appears that the high temperature deposition produced much larger islands and that island coalescence is occurring more often than that in the lower temperature deposited films.

75 nm thick samples. The AFM images and line trace surface analyses of three Cu films with thickness of 75 nm are shown in Figure 4.7. These Cu films grown at substrate temperatures of 150°C, 250°C, 430°C with image RMS roughness of 1.5, 12, and 20 nm, respectively.

20 nm thick samples: There were two 20 nm thick Cu films that were in the as-grown category. These were grown at substrate temperatures of 250°C and 350°C. The AFM images and line trace surface analyses of these two samples are shown in Figure 4.8. The image RMS roughness of these are 5.5 nm and 10 nm, respectively.

The AFM analysis results from the as-grown films revealed that sputter deposition of Cu films with lower substrate temperature generally results in a smoother surface topography. However, samples deposited at higher substrate temperature generally have deeper valleys (trough). The exception was in the case of Figure 4.6(c) (grown at 475°C),

The Effect of Deposition Temperature on Surface Topography of
150 nm Thick Cu Films as Grown at 150°C, 350°C, and 475°C.

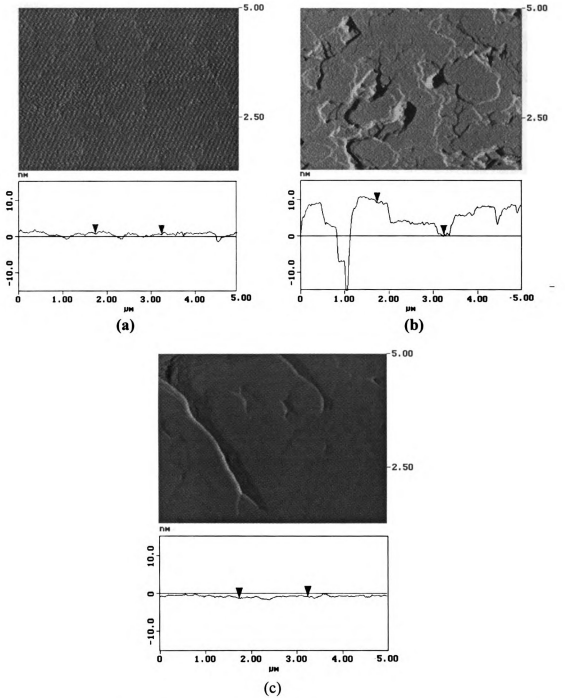

Figure 4.6 Atomic-force-microscopy images and line trace surface analyses showing the surface topography of 150 nm thick Cu films deposited at substrate temperatures of: a) 150°C , b) 350°C; and c) 475°C with image RMS roughness of about 1.3, 23, and 2.6 nm, respectively.

The Effect of Deposition Temperature on Surface Topography of
75 nm Thick Cu Films as Grown at 150°C, 250°C, and 430°C.

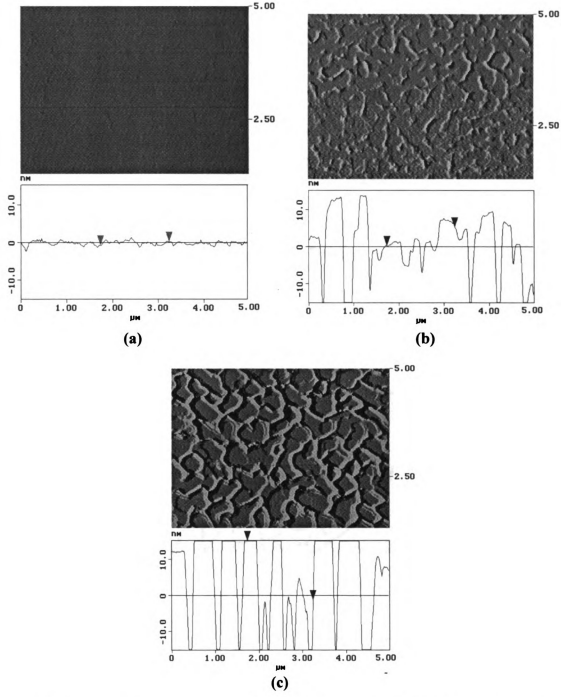

Figure 4.7 Atomic-force-microscopy images and line trace surface analyses showing the surface topography of 75 nm thick Cu films deposited at substrate temperatures of: a) 150°C , b) 250°C; and c) 430°C with image RMS roughness of about 1.5, 12, and 20 nm, respectively.

The Effect of Deposition Temperature on Surface Topography of
20 nm Thick Cu Films as Grown at 250°C, and 350°C

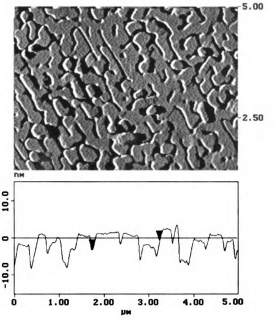

(a)

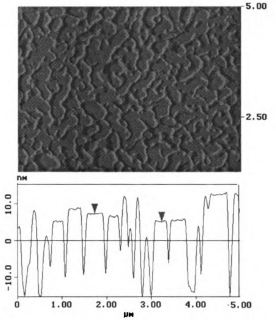

(b)

Figure 4.8 Atomic-force-microscopy images and line trace surface analyses showing the surface topography of 20 nm thick Cu films deposited at substrate temperatures of: a) 250°C and b) 350°C with image RMS roughness of about 5.5 and 10 nm, respectively.

which has larger sized islands, and very few shallow troughs. These islands had a better chance to coalesce in this temperature range.

4.4.1.2 Effect of Film Thickness

In this section, the effect of film thickness on the surface topography of the sputter deposited Cu films is examined. The first group consisted of four Cu films deposited at a substrate temperature of 350°C on epitaxial Nb. AFM images and surface analysis of these Cu films with thicknesses of 20, 100, 170, and 300 nm are shown in Figure 4.9. The image RMS roughness are 9.9, 28, 23.3, and 28.7, respectively. The image RMS roughness results suggest that the thinnest Cu film (20 nm) had smoother surface morphology. However, the AFM images suggest that thinner films have smaller islands (~0.3 μm compared to ~1.0 μm), but by considering the number of island per unit area, the thinner films are rougher. As examples, on thicker films (100 and 170 nm) the island sizes increased while the troughs become deeper (especially in 100 nm thick film). The images of the 300 nm film in part (d), however, had the roughest surface topography compared to rest of the samples with a mixed island size and many deep troughs. The second group consisted of three Cu films deposited at 150°C and post deposition annealed at 350°C. Figure 4.10 shows AFM images and the line trace surface analyses of: a) 20 nm, b) 200 nm, 250 nm Cu films deposited on epitaxial Nb at 150°C. The image surface roughnesses were 4.5, 5.7, and 8.5 nm, respectively. In this group of Cu films, the island sizes and trough depths increased with increasing film thickness.

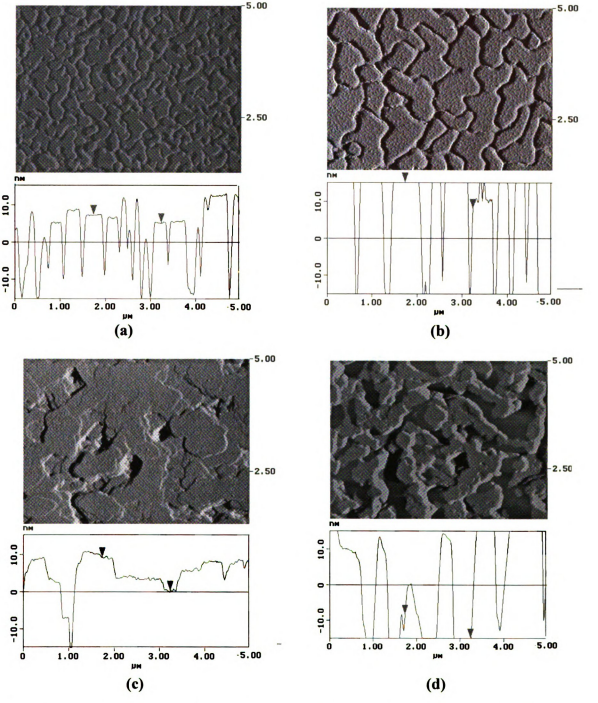

Figure 4.9 Atomic-force-microscopy images and line trace surface analyses showing the surface topography of: a) 20 , b) 100, c) 170, and d) 300 nm Cu films; grown at 350°C on a 250 nm epitaxial Nb buffer layer. The line trace surface analysis shows the image RMS roughness are about 10, 28, 23, and 28 nm, respectively.

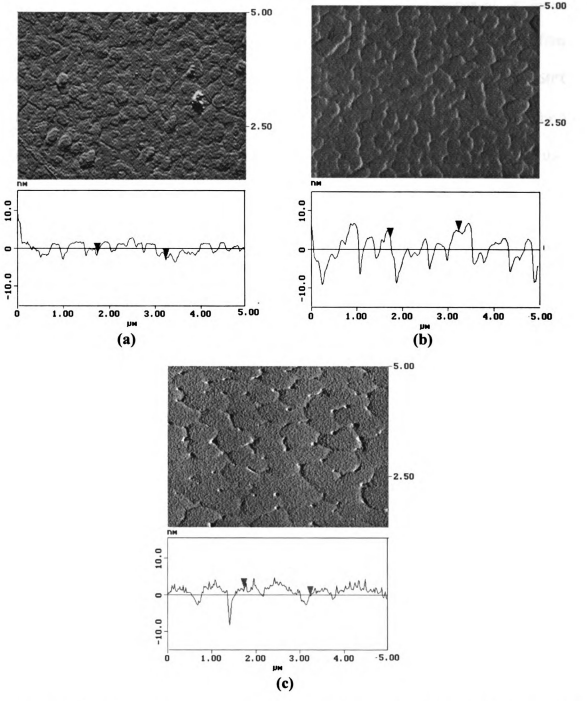

Figure 4.10 Atomic-force-microscopy images and line trace surface analyses showing the surface topography of: a) 20, b) 200, c) 250 nm Cu films; grown at 150°C and post deposition annealed at 350°C. The line trace surface analysis shows the image RMS roughness are about 4.5, 5.7, and 8.5 nm, respectively.

4.4.1.3 Effect of Post Deposition Annealing

Some of the Cu films were subsequently post deposition annealed at several temperatures to examine the effect of annealing on the topography of the sputtered films. The first group of samples consisted of four 300 nm thick Cu films deposited at 150°C. Three of these films were post deposition annealed at 250°C°, 350C°, and 500C° for 30 minutes. Figure 4.11 shows the AFM images and line trace surface analysis of these films. The image RMS roughnesses are approximately 4.5, 8.8, 6.3, and 3.6.nm, respectively. Films with AFM images in part (b), (c), and (d) were deposited during the same sputter deposition run using similar substrates (from same wafer). These images appeared to be rougher than image in part (a). The AFM image of the sapphire substrate used for these three films showed rough surface topography and pre-deposition annealing of Al_2O_3 at 1200°C did not smooth the surface. However, by comparing these three samples, it seems that when the annealing temperature increased to 500°C, the surface roughness decreased.

Two additional samples were deposited at a substrate temperature of 350°C and one of them was post deposition annealed at 500°C. In Figure 4.12, AFM images and surface analysis of the 300 nm thick Cu films grown at 350°C before and after post deposition annealing at 500°C for 30 minute are shown. The film surface roughness decreased to about 6 nm from 28 nm, as shown in Figure 4.12 (a). The AFM images of these two films shows a clearer picture of the effect of post-deposition annealing on the Cu films. In image (b), there are large, continuous, smooth islands with some troughs. This is an indication of the effect of post-deposition annealing.

The Effect of Post Deposition Annealing on Surface Topography of 300 nm thick Cu Films Grown at 150°C

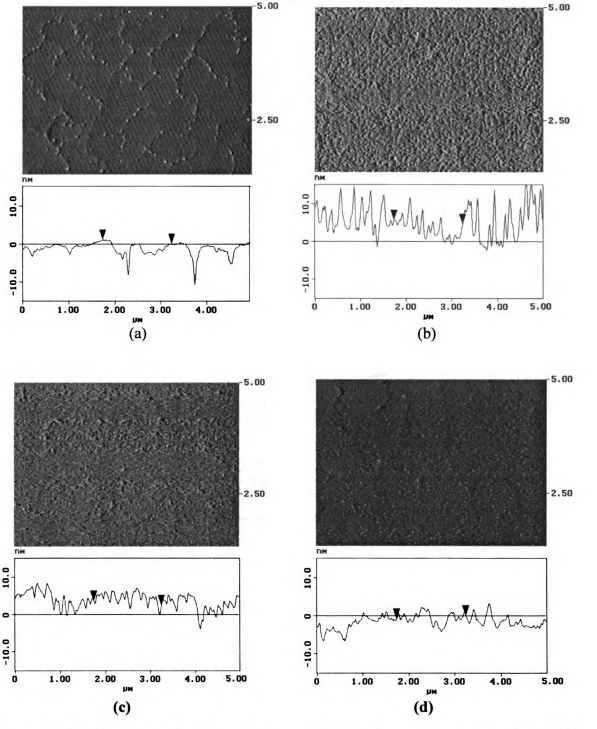

Figure 4.11 The effect of post deposition annealing on the surface topography of 300 nm thick Cu films. The post deposition annealing temperatures were a) as grown =150°C, b) 250°C, c) 350°C, and d) 500°C, respectively. The line trace surface analysis shows the image RMS roughness are about 4.8, 8.8, 6.3, and 3.6 nm, respectively.

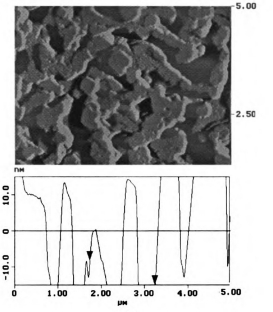

(a)

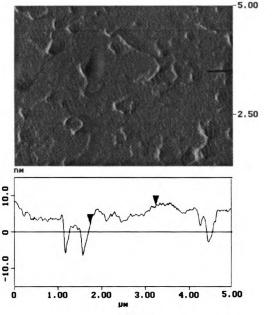

(b)

Figure 4.12 Atomic force-microscopy images and line trace surface analyses showing the surface topography of 300 nm thick Cu films deposited at a substrate temperatures of 350°C and post deposition annealed at: a) as grown and b) 500°. The line trace surface analyses shows the image RMS roughness are approximately 28 and 6.5, respectively.

4.4.1.4 Effect of Deposition Rate:

As discussed in the Chapter 1, epitaxial films fabricated by MBE have very smooth surfaces and these films are typically grown with a deposition rate of 0.1-0.5 Å/s. Therefore, in this study the effect of the deposition rate (DR) on the surface topography of epitaxial films grown by sputter deposition was of interest. Three Cu films were deposited with different deposition rate conditions:

a) Start and finish with a low DR = 1 Å/s.

b) Start and finish with DR = 4.1 Å/s.

c) Start and finish with a high DR = 7 Å/s.

These films were grown at 150°C and post deposition annealed at 350°C. Figure 4.13 shows AFM images and line trace surface analyses of 200 nm Cu films with the respective image RMS roughness of approximately 1.5, 5.7, and 4.8 nm for 1 Å/s, 4.1 Å/s, and 7 Å/s. The Cu film deposited with low deposition rate (1 Å/s) appeared to have large size islands and some holes. The Cu films grown with 4.1 Å/s, and 7 Å/s deposition rate had rougher surface topographies with smaller islands, and possibly collimated grain formation in Cu film with 7 Å/s deposition rate. These results are consistent with theoretical predictions [37], which indicate that increasing the deposition rate results in smaller islands.

4.4.1.5 Effect of Deposition Techniques

Compared to MBE, sputtering deposition is a relatively high-energy deposition technique. To allow a comparison of the epitaxial sputtered samples grown in the present work, a 300 nm thick Cu film, grown by MBE, was provided by the University of Leeds-

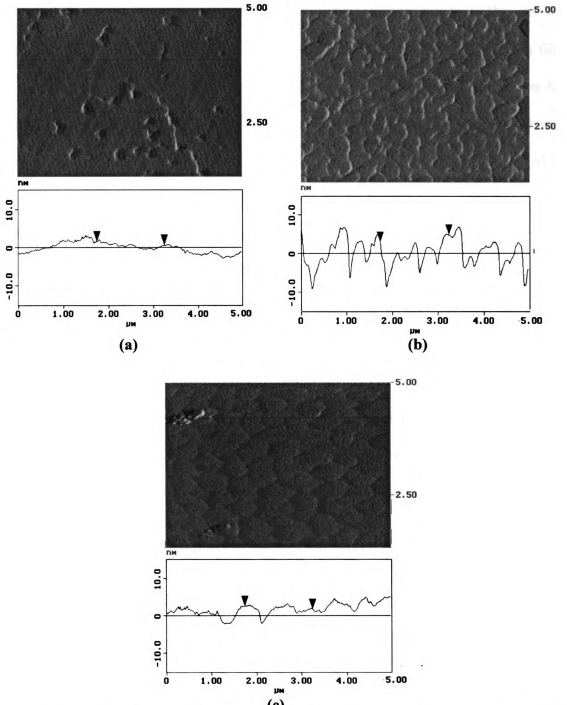

Figure 4.13 Atomic-force-microscopy images and line trace surface analyses showing the surface topography of 200 nm epitaxial Cu films grown at 150°C and post deposition annealed at 350°C with deposition rate of: a) 1, b) 4.1, and c) 7 Å/s on a 250 nm epitaxial Nb buffer layer. The line trace surface analyses shows the image RMS roughness are about 1.5, 5.7, and 4.8 nm , respectively.

England. This sample was grown on a 100 nm epitaxial Nb film (grown at 950°C prior to deposition of the Cu film) at a substrate temperature of 350°C. The surface topography of this sample was compared with a 300 nm thick sputter deposited Cu film onto 250 nm epitaxial Nb film at the same temperature of 350°C. The deposition rate for the sputter deposited sample was 4.1 Å/s (1 Å/s for first few monolayers and gradually increased to 4.1 Å/s). The growth rate for the MBE grown film was 0.5 Å/s. AFM images and surface analyses of these two films are shown Figure 4.14. The image RMS roughnesses are about 23 and 46 nm, respectively. The AFM image in Figure 4.14(b) indicates that the MBE grown film had larger islands when compared with the sputter deposited sample, with smoother island tops and deeper grooves between these islands.

4.4.2 EBSP Analysis

Up to this point the surface topographies of sputter deposited Cu films have been discussed; however, the surface topography does not provide information about the orientation and epitaxy of the deposited films. To generate orientation information, a second characterization technique, EBSP, was carried out. The EBSP technique was used to examine the crystallographic nature of the Cu films that were investigated using AFM. The results of the EBSP data analysis have been categorized in a similar way to the AFM results.

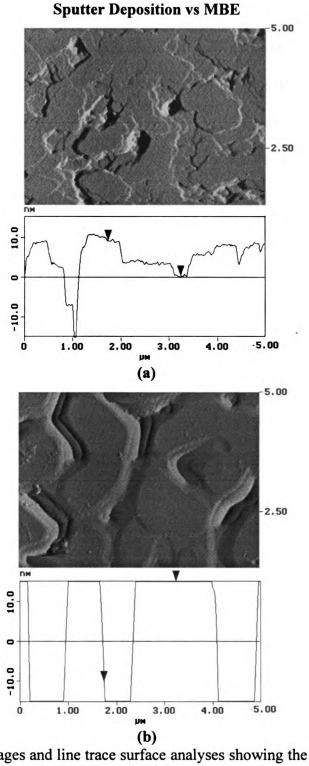

Figure 4.14 AFM images and line trace surface analyses showing the surface topography of: a) 300 nm Cu film sputter deposited at 350°C on a 250 nm epitaxial Nb buffer layer, b) 300 nm Cu film; grown at 350°C by MBE technique on a 100 nm epitaxial Nb buffer layer. The image RMS roughnesses are about 23 and 46 nm, respectively. The deposition rates were a) start with 1Å/s for first few monolayers and then 4.1 Å/s and b) 0.5 Å/s.

4.4.2.1 EBSP Patterns of Cu Films

EBSP and different variants EBSP data was collected randomly from different locations on each sample. The pole figures obtained from the EBSP data of the Cu films revealed that two different orientation variants were present in all of the films analyzed. Both variants display <111> growth normals, consistent with growth occurring on the close-packed {111} planes in the fcc Cu. The two variants differ by a multiple of 60° rotation about this (111) normal, indicating that while the first epitaxial Cu plane is the same for each variant, the subsequent stacking of additional {111} planes occurred by two different stacking orders, ABCABC versus ACBACB. Thus, the two variants are oriented in a Σ(3) twin relationship, but have incoherent boundaries (ITB). In Figure 4.15, an EBSP and corresponding pole figures of a 300nm thick sputter deposited Cu film are presented. In this figure, each of the patterns was captured from an individual variant (twin). Because of the orientation relationship between these two variants, a number of relatively strong Kikuchi bands (such as {131} and {311}) in the EBSP pattern are common to both orientations, thus the two orientations are distinguished by differences in other Kikuchi bands or poles such as I = [101], II = [011], and III = [001].

EBSP and twin boundaries. After observation of twin variants in the epitaxial Cu films, it was of interest to determine the effective resolution of the EBSP (effective interaction volume) on the twin boundaries. To study this issue, an approximate location of a twin boundary was selected; the electron beam was then slowly scanned over the selected sample area. A series of patterns were collected during the scan, as shown in Figure 4.16. These patterns show the transition from one variant to the other. The Kikuchi bands in the EBSP pattern (Figure 4.16 (a)) from one the variants (only I = [101] pole can be seen)

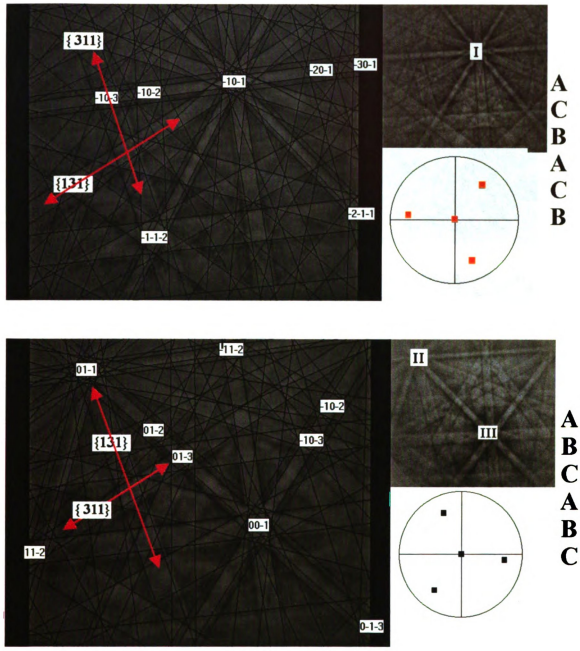

Figure 4.15 Indexed EBSPs and corresponding pole figures from a 300nm epitaxial Cu film sputtered at 350°C onto a 250 nm of epitaxial Nb substrate showing the two (111) orientation variants.

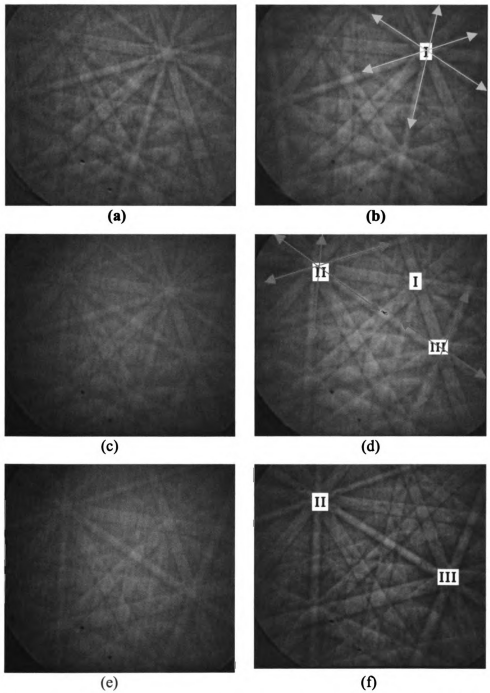

Figure 4.16 Changes in the Kikuchi bands of EBSP patterns obtained from 300 nm thick epitaxial Cu film as the sample was moved across a twin boundary. In part (a) and (b) the EBSP patterns are from one of the variants. In parts (c) and (d) the Kikuchi bands contributed from both variant were present. In parts (e) and (f), only the Kikuchi bands from other variant are distinguishable.

showing no evidence of bands from the other variant. As the electron beam approached the twin boundary, a collection of Kikuchi bands from both variants, with relatively the same intensities, appeared (all three poles I, II, and III can be seen in Figures c and d). By moving further away from the first variant and boundary, only the Kikuchi bands that originated from the second variant (II and III poles) are distinguishable in the EBSP pattern (Figure 4.16(f)). Therefore, scanning the electron beam over a fixed area (for example 10 μm) of a sample and using several different step sizes (such as 0.1, 0.2, 0.5, 0.8, 1.0, 1.5, and 2 μm) could provide a relative effective interaction volume (resolution of the EBSP) within the epitaxial Cu films. A typical effective interaction volume for Cu in this study was found to be approximately 0.8-1.2 μm. After tilting the sample about 70 degrees from its horizontal position, the effective interaction volume increased to approximately 2.3 to 3.5 μm in one direction as shown in Figure 17. As the result of this measurement, a step size of 1 μm was chosen to be used for most of this study. The detail of step size measurement is given in appendix 4.B.

Indexing of the EBSP patterns. All patterns which originated from individual variants were easily indexed using the Channel 4 software. However, EBSP patterns which contained bands from both variants (at twin boundaries) usually remain unsolved during indexing, resulting in blank points on the orientation map at the twin boundaries. An example of this behavior is shown in Figure 4.18. In this figure, an orientation map and corresponding pole figure showing two (111) orientation variants. The light green areas (blank points) around the twin boundaries are unsolved orientations. These unindexed areas (noise) could be removed using the Channel 4 software which substitutes the

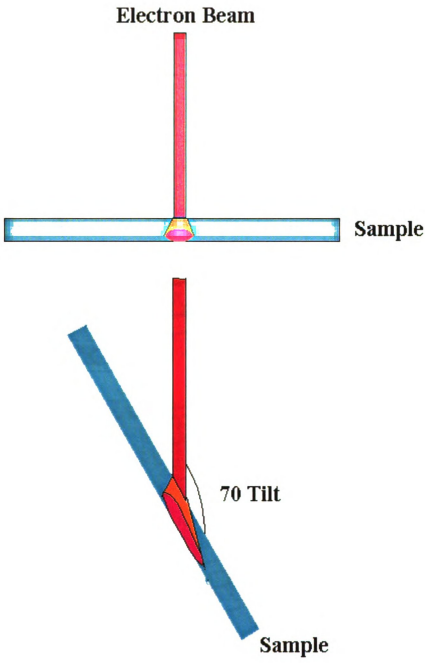

Figure 4.17 Effect of tilting on electron beam size on the surface of the sample (effective beam size) and on the interaction volume within the sample.

Orientation Map of 300 nm Thick Epitaxial Cu Film

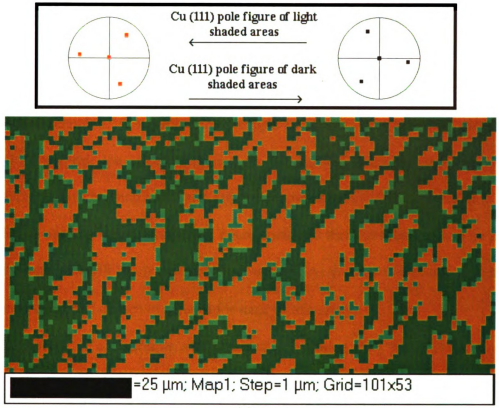

(a)

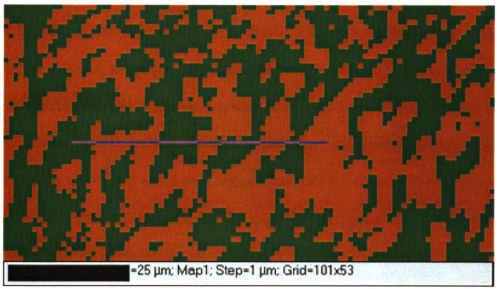

(b)

Figure 4.18 EBSP (111) pole figures and orientation map of the two (111) orientation variants present in the 300 nm epitaxial Cu film. In figure (a), the orientation map as recorded by computer is shown. In the figure (b), the same map after noise was removed by Channel 4 software.

unindexed point with the orientation of a nearest neighbor (with larger variant size. Figure 4.18(b)).

EBSP and Orientation map of variants distribution To measure the size and distribution of the variants in the epitaxial Cu films, the samples were mapped using stage control scanning. To resolve the changes in variants size and their distribution within the Cu films, the effective interaction volume and scanning step size become crucial factors. By choosing a step size larger than the effective interaction volume, some of the details such as variants size, twin boundaries, and their distribution will be missed during the scan and will result in a meaningless map. As described in previous section, a step size of 1 μm was chosen to be used for most of this study.

Film uniformity. To determine a representative scanning size, the uniformity of the variants distribution in sputter deposited epitaxial Cu films was investigated by performing long range scans. The result of a 2000 μm x 100 μm scan size of one of the epitaxial Cu film is shown in Figure 4.19. By comparing these long-range scans with many smaller (100 μm x 100 μm) scans size on the epitaxial Cu films, it was observed that the variants displayed a similar behavior with a random distribution without any particular morphological patterns evident. Therefore, a smaller scanned area (for example100 μm x 100 μm) could be a representative of the variants distribution within the epitaxial film. It should be noted that the data taken for Figure 4.19 totaled 144 hours (6 days and nights) of electron microscope time. The smaller scanned areas usually took between 5 to 10 hours of electron microscope time.

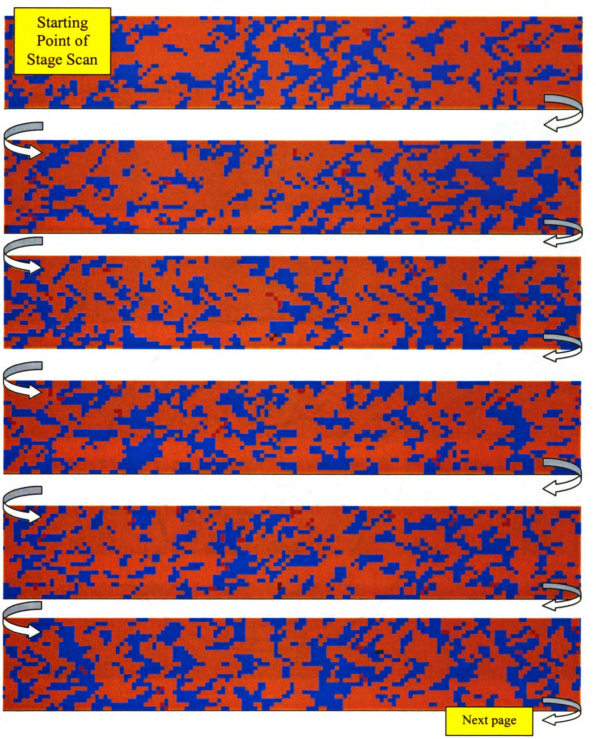

Figure 4.19 Orientation map of the distribution of two twin variants in a 200000 μm^2 area (2000 μm x 100 μm) of a 300 nm epitaxial Cu film grown onto 250 nm of epitaxial Nb. The green areas are from unsolved patterns, and all other color spots are improperly indexed. Note that these maps were connected in one piece in the original map.

Long Range Distribution of Twin Variants

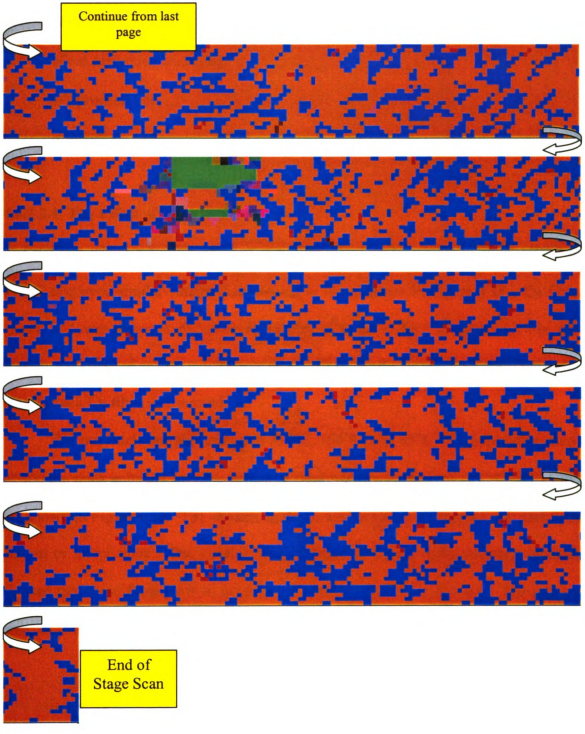

4.4.2.2 Effect of growth parameters on the variant size and their distributions.

In this section, the effects of the following parameters will be presented.

- Growth temperature.
- Film thickness.
- Post deposition annealing.
- Deposition rate.
- Deposition technique.

4.4.2.2.1 The Effect of Growth Temperature

Cu films which were deposited at a substrate temperature ranging from 150°C to 475°C displayed similar variant distributions to those shown in Figure 4.17. Cu films grown at lower temperature, however, display different variant distributions. In this section, the effect of growth temperature on size of twin variants and their distribution for 300nm thick Cu films is discussed.

300 nm thick samples grown at 350°C, 150°C, and 90°C The orientation maps of 300 nm thick epitaxial Cu films grown at substrate temperatures of 350°C and 150°C are shown in Figure 4.20. The variants in these two maps did not display any particular pattern or morphology. The variants sizes, determined by the linear intercept method, showed that these films have an average twin variant size of 4 ± 0.5 μm. The relative areas of the two twin variants varied between 45% and 55%.

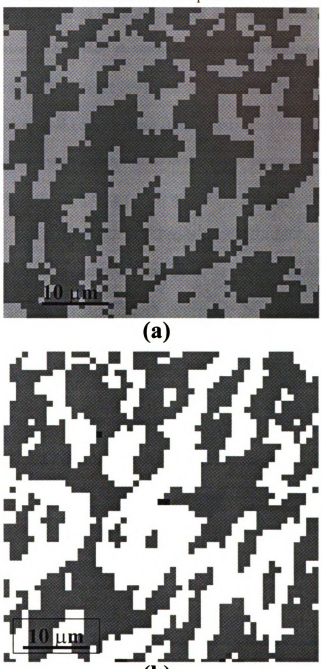

Figure 4.20. Orientation map of the 300 nm thick epitaxial Cu films grown onto 250 nm epitaxial Nb at a substrate temperature of a) 350°C and b) 150°C.

In a typical magnetic multilayer or spin-valve, only the first Nb and consecutive Cu layer are deposited at elevated temperatures (to ensure the epitaxy). The rest of magnetic and non-magnetic layers (such as Cu spacer) must be deposited at low temperature to reduce the interdiffusion. Therefore, to study the quality of epitaxial Cu films grown at low temperature, a few Cu films were deposited onto epitaxial Nb at 90°C and the EBSP result was analyzed. A typical EBSP pattern (unindexed) from these samples is shown in Figure 4.21. In this figure, the Kikuchi bands in the EBSP pattern do not have very sharp band edges (compared to those in figure 4.15) and has slight degradation. By comparing Figures 4.22 (b & d); some of the Kikuchi bands in (b) (Cu film grown at high T) are clearer and the band edges are sharper than those in (d) as pointed by arrows. This difference suggests the existence of strain in the Cu film that was grown at room temperature [38]. To measure the size and distribution of the variants in Cu films grown at 90°C, stage control scanning was used. However, after careful observation of the patterns during the scanning, it was noticed that the patterns did not change during the scanning processes and had relatively the same appearance. It was also noted that these EBSP patterns are very similar to those that were collected from grain boundaries that was shown in section 4.5.1 (see Figure 4.22 (b & d). As explained in that section, the analysis of these types of EBSP patterns revealed that both variants coexist within the EBSP interaction volume.

Therefore, without consistent band indexing, the patterns are unsolvable and it is impossible to use EBSP to fully characterize the variant size and distribution in the Cu films grown at this temperature (90°C) range. However, it can be concluded that the Cu films grown 90°C onto epitaxial Nb substrate were epitaxial, possessing two different

EBSP of a Cu Film Grown at 90°C Temperature

Figure 4.21 Electron backscatter pattern obtained from a 300 nm Cu film grown onto epitaxial Nb film at 90°C. This pattern shows some degradation compared to patterns from Cu film grown at 350°C.

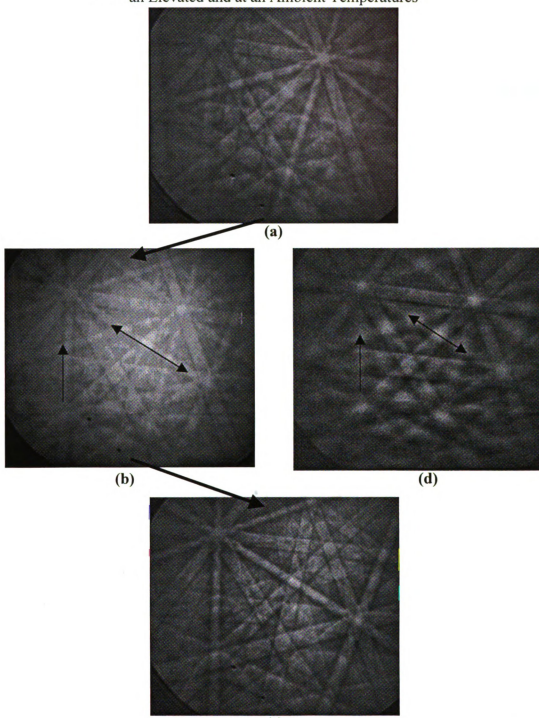

Figure 4.22 (a), (b), and (c) changes in the Kikuchi bands of EBSP patterns of a 300 nm thick epitaxial Cu film deposited at 350°C as sample was moved across a boundary (see figure 4.16). (a) and (c) are individual twin variants. (b) and (d) contains bands from both variants

(111) orientation variants. The results also suggest that the sizes of these variants (twins) are smaller than the effective interaction volume and they simultaneously contribute crystallographic information to EBSPs [39].

Grain sizes --- AFM vs. EBSP. In section 4.4.1.1 (AFM results), the surface topography of the epitaxial Cu films grown at room temperature and 350° were shown in Figure 4.5-(a) and (c). It was a point of interest to establish a relationship between the size and distribution of islands from AFM images and size and distribution of the twin variants in the EBSP orientation map of a sample. An AFM image of a 300 nm thick Cu film grown at 350°C was superimposed on a corresponding EBSP orientation map. In Figure 4.23, the AFM image and EBSP variants distribution map of this sample is shown. The result of this comparison revealed that there is no correlation between the size and distribution of the islands in the AFM image and the size and distribution of the twin variants in the EBSP orientation map.

4.4.2.3 The Effect of film thickness -- Limit of EBSP

As noted in section 4.4.1.2 of the AFM results, the surface roughness of epitaxial Cu films typically increase as the film thickness increases (regardless of growth temperature). Despite this increase, the twin variant morphology and size does not appear to be a strong function of film thickness for films between 150 to 300 nm. However, as the Cu film thickness decreases, the backscattered electron interaction volume extends into the Nb buffer layer. Thus, the diffracted electrons from the Nb significantly contribute to the electron backscatter diffraction patterns of the thin films,

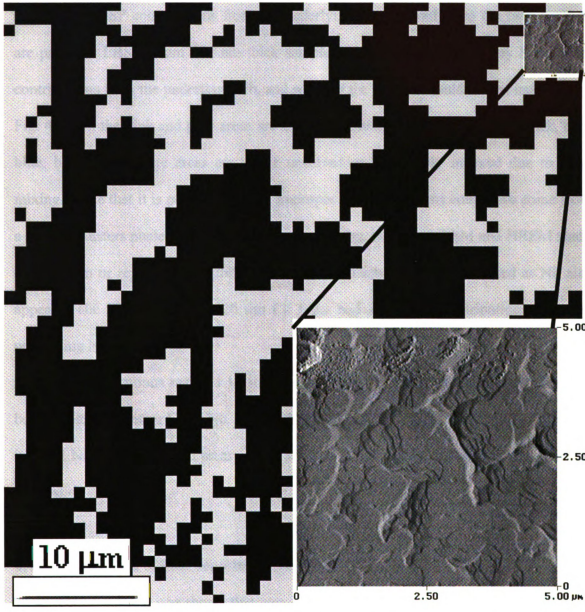

Figure 4.23 An AFM image of a 300 nm thick Cu film deposited at 350°C, superimposed on the orientation map of the same sample. This comparison shows there is no correlation between the size islands (on AFM image) and size of twin variants (on EBSP map).

creating confusion in the indexing processes. This behavior is illustrated in Figure 4.24, which shows orientation maps of 250, 100, and 20 nm thick films.

In general, epitaxial Cu films with a thickness greater than 150 nm did not have significant EBSP contributions from the underlying Nb, and only two Cu twin variants are present. EBSPs from 100 nm thick samples were partially affected by backscatter contributions from the underlying Nb, and some of the patterns could not be indexed. In Fig. 4.24(b), the pink and gray areas are the two Cu twin variants, the green, black, dark blue, blue, and orange areas are either unsolved or improperly indexed due to band mixing. Note that it is possible that the improper indexed patterns could also come from a few Cu clusters nucleated with different orientations, but only a TEM and HREM study can confirm or reject this possibility. A few brown spots that were indexed as Nb also appear. The EBSPs from the 20 nm Cu films had significant contributions from the underlying Nb.

These contributions resulted in some of the patterns being unresolvable, but others being indexed as either Cu or Nb. In Fig. 4.24(c), the brown areas correspond to properly indexed Nb, while the blue areas were solved as Nb, but were indexed in the different orientation.

4.4.2.4 The Effect of Post deposition annealing

In section 4.4.3, it was shown that post annealing affects the surface topography of the sputtered Cu films. However, EBSP results from all of the post deposition annealed samples showed that post deposition annealing generally does not affect the twin morphology and variant orientation distributions. This was the case regardless of the

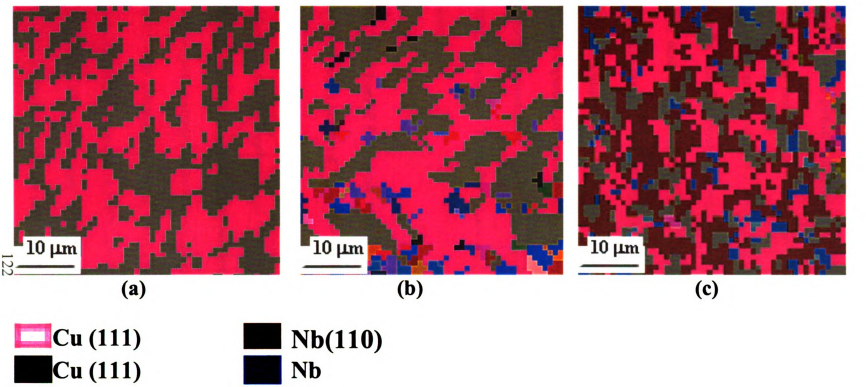

Figure 4.24. Orientation maps of (a) 250, (b) 100, and (c) 20 nm Cu films grown on a 250 nm epitaxial Nb film at a substrate temperature of 350°C. The orientation maps in (b) and (c) displayed a few different variants as indicated on maps (as different color), which shows contributions from the underlying Nb.

sputter deposition temperature. As an example, orientation maps for two 300 nm thick epitaxial Cu films grown at a substrate temperature of 350°C, one of which (b) had been post deposition annealed at 500°C, are shown in Figure 4.25. These films have an average twin variant size of 4.1 and 3.7 μm, respectively. The relative areas of the twin variants for both films varied between 45% and 55%.

EBSP analysis of the epitaxial Cu films grown at 150°C and post deposition annealed at 500°C also revealed two different (111) orientation variants. However, the distribution map of these sample shows some grain (variant) growth compared to an as-grown film (at 150°C). In Figure 4.26, orientation maps for two 300 nm thick epitaxial Cu films grown at a substrate temperature of 150°C, one of which (b) had been post deposition annealed at 500°C, are shown. These films have an average twin variant size of 5.6 and 7.1 μm, respectively.

4.4.2.5 The Effect of Deposition Rate

As discussed in section 4.4.1.4, the surface topography of the sputtered Cu films was affected by deposition rate. A low deposition rate (1 Å/s) produced larger islands with smoother film surfaces (compared to those grown at higher deposition rate). EBSP results of these epitaxial films grown at deposition rates of 1 Å/s, 4.1 Å/s, and 7 Å/s, however, revealed similar orientation maps in all samples. Orientation maps of 200 nm Cu films deposited with a deposition rate of 1 Å/s and 7 Å/s at a substrate temperature of 150°C and post deposition annealed at 350°C are illustrated in Figure 4.27. The quality of the EBSP patterns of sample with deposition rate of 1 Å/s was very good, but slight degradation was noted in sample with growth rate of 7 Å/s. Grain sizes in the films

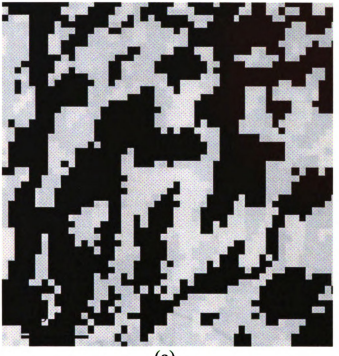

(a)

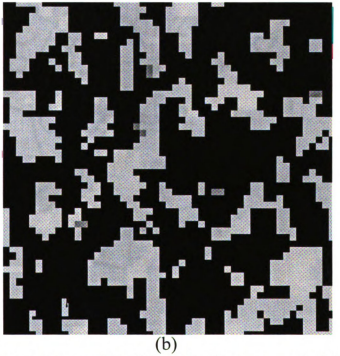

(b)

Figure 4.25 a) Orientation map of the 300 nm Cu film grown onto 250 nm epitaxial Nb at a substrate temperature of 350°C. b) Orientation map of the 300 nm Cu film grown onto an epitaxial Nb film at a substrate temperature of 350°C and post deposition annealing of 500°C for 30 min.

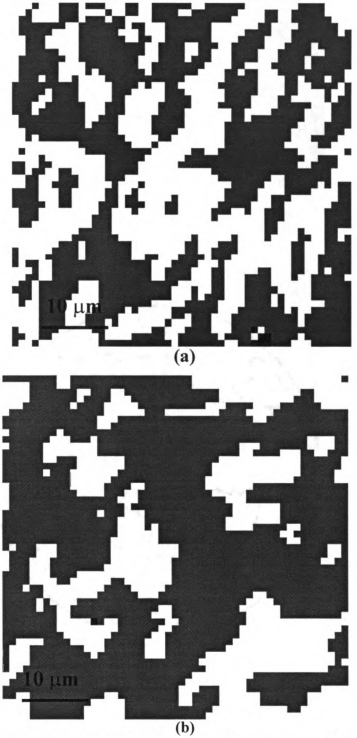

Figure 4.26 a) Orientation map of the 300 nm Cu film grown onto 250 nm epitaxial Nb at a substrate temperature of 150°C. b) Orientation map of the 300 nm Cu film grown onto an epitaxial Nb film at a substrate temperature of 150°C and post deposition annealing of 500°C for 30 min.

(a)

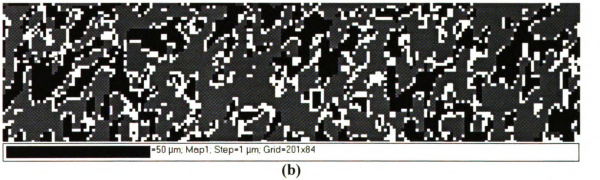

(b)

Figure 4.27. Orientation maps of two 300 nm thick epitaxial Cu films grown at 150°C and post deposition annealed at 350°C with deposition rates of: a) 1Å/s and b) 7Å/s. The white areas on both maps are due to unsolved patterns (mostly on grain boundaries).

deposited with different deposition rates were determined by the linear intercept method. These films have an average twin variant size of epitaxial film grown with deposition rate of 1 Å/s and 7 Å/s are 2.8 and 4.9 μm, respectively. The relative areas of the twin variants were similar to the previous cases, which varied between 45% and 55%. Table 4.3 summarizes the grain size and relative areas of the twins in all the epitaxial Cu films studied.

4.4.2.6 The Effect of Deposition Technique

The epitaxial Cu film grown by MBE (at Leeds University) also revealed the existence of two variants. Figure 4.28 shows the similarity of the orientation maps of 300 nm thick epitaxial Cu films (MSU and Leeds) grown onto epitaxial Nb substrates. The average grain sizes in these films were 4.1 and 3.5 μm, respectively. The relative areas of the twin variants that varied between 45% and 55%, were similar to the previous cases.

Table 4.3

Summary of Average Grain (twin) Sizes
(Statistical: Intercept Method)

Run & Sample #	Element	Thic-kness (nm)	Growth /Anneal T°C	Scan length (μm) X x Y x Step Size	% Twins Area	Grain size (μm ± 1 μm)
17-2	Cu	300	350/500	10x10x1		4
18-1		80	350/No	10x10x1	N/A	TS
18-2		80	430/No	50x40x0.1	N/A	TS
18-3		20	250/No		N/A	TS
18-4		20	350/No		N/A	TS
19-1		20	150/250		N/A	TS
21-1		300	350/No	100x52x1	51%, & %48,& %1UnSolved (US)	4.3
21-2		300	350/No	100x36x1 2000x26x0.5	55%, & 45% 49%, %32, %19US	4.5 5.3
21-3		250	150/350	50x82x1	55%, & 45%	4.7
22-3		300	250/350	100x50x1		-----
22-4		100	350/No	100x70x.5	44%, &36%, 20% US	4.8
23-1		300	150/No	50x50x1	53%, & 46% 11% US	7
23-2		300	150/250	50x50x1	59%, & 41%	-----
23-3		300	150/350	2000x23x1	57%, & 43%	3.5
23-4		300	150/500	50x50x1	70%, & 30%	4-6
26-1		72	150/No			TS
26-2		150	150/No	50x20x1		4.7
26-3		300	350/500	50x80x1		4.6
29-1		200	150/350	100x100x1		2.6
29-2		200	150/350	200x49x1		6.6
29-3		200	150/350	100x200x1		4.8
30-1		300	350	200x73x1		4.5

TS = Sample is Thinner than 150 nm and there are band contributions from the buffer layer. NA = In all films grown at low temperature, the grain distributions are not detected by EBSP techniques, thus the grain sizes are Not Available.

Orientation Maps of Sputter Deposited vs MBE Sample

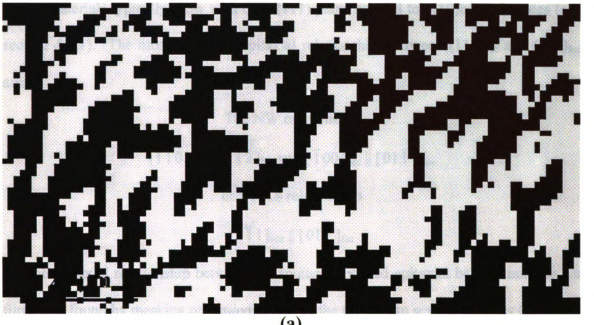

(a)

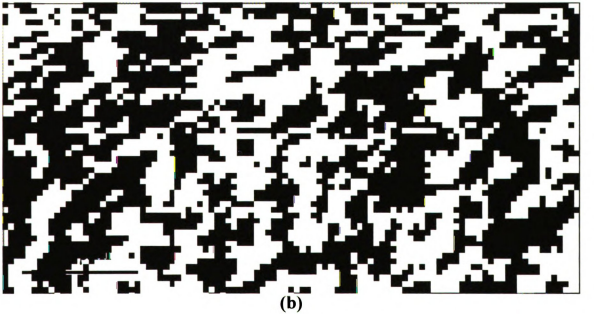

(b)

Figure 4.28 Orientation map of the distribution of two variants in 300 nm epitaxial Cu film grown onto: a) A 250 nm of epitaxial Nb using dc sputtering. b) A 100 nm of epitaxial Nb using the MBE technique. (The MBE facility is located at University of Leeds England).

4.5 ORIENTATION RELATIONSHIP BETWEEN Cu AND Nb

fcc materials typically grow with their (111) plane parallel to (110)bcc substrates (see section 4.2.1). The most favorable epitaxial relationships between $(110)_{bcc}$ and $(111)_{fcc}$ are:

The NW relationship

$$[1\bar{1}0]_{bcc} \parallel [1\bar{1}2]_{fcc} \text{ and } [\bar{1}00]_{bcc} \parallel [01\bar{1}]_{fcc},$$

or the KS relationship

$$[1\bar{1}1]_{bcc} \parallel [01\bar{1}]_{fcc}$$

The epitaxial relationship between the sputter deposited epitaxial bcc Nb and fcc Cu films was found by masking or removing part of the Cu film in several samples (grown at different deposition runs)
and collecting EBSP data from adjacent sections of Nb and Cu. The resulting {100}, {110}, and {111} pole figures were used to plot the stereographic projections of both the Nb and the Cu. Figure 4.29 shows a typical example of the stereographic projections of epitaxial (110)Nb and (111)Cu films. By superimposing the Cu stereographic projection on the Nb, it can be seen that $(110)_{bcc}$Nb $\parallel$ $(111)_{fcc}$Cu, with $[1\bar{1}0]_{bcc}$Nb $\parallel$ $[1\bar{1}2]_{fcc}$ Cu and $[\bar{1}00]_{bcc}$Nb $\parallel$ $[01\bar{1}]_{fcc}$ Cu, which is the NW relationship. This is different from that observed in the polycrystalline Nb-$(Cu\text{-}Co)_x$ multilayers sputter deposited at room temperature in our lab [40]. In that study, HREM image analyses of polycrystalline multilayers showed that the Nb-Cu orientation relationship was close to the KS relationship $(110)_{bcc}$Nb $\parallel$ $(111)_{fcc}$Cu with $[1\bar{1}1]_{bcc}$Nb $\parallel$ $[01\bar{1}]_{fcc}$Cu. The KS relationship was also observed in polycrystalline Nb/Cu multilayers by Mitchell et al. [41] using selected area electron diffraction patterns.

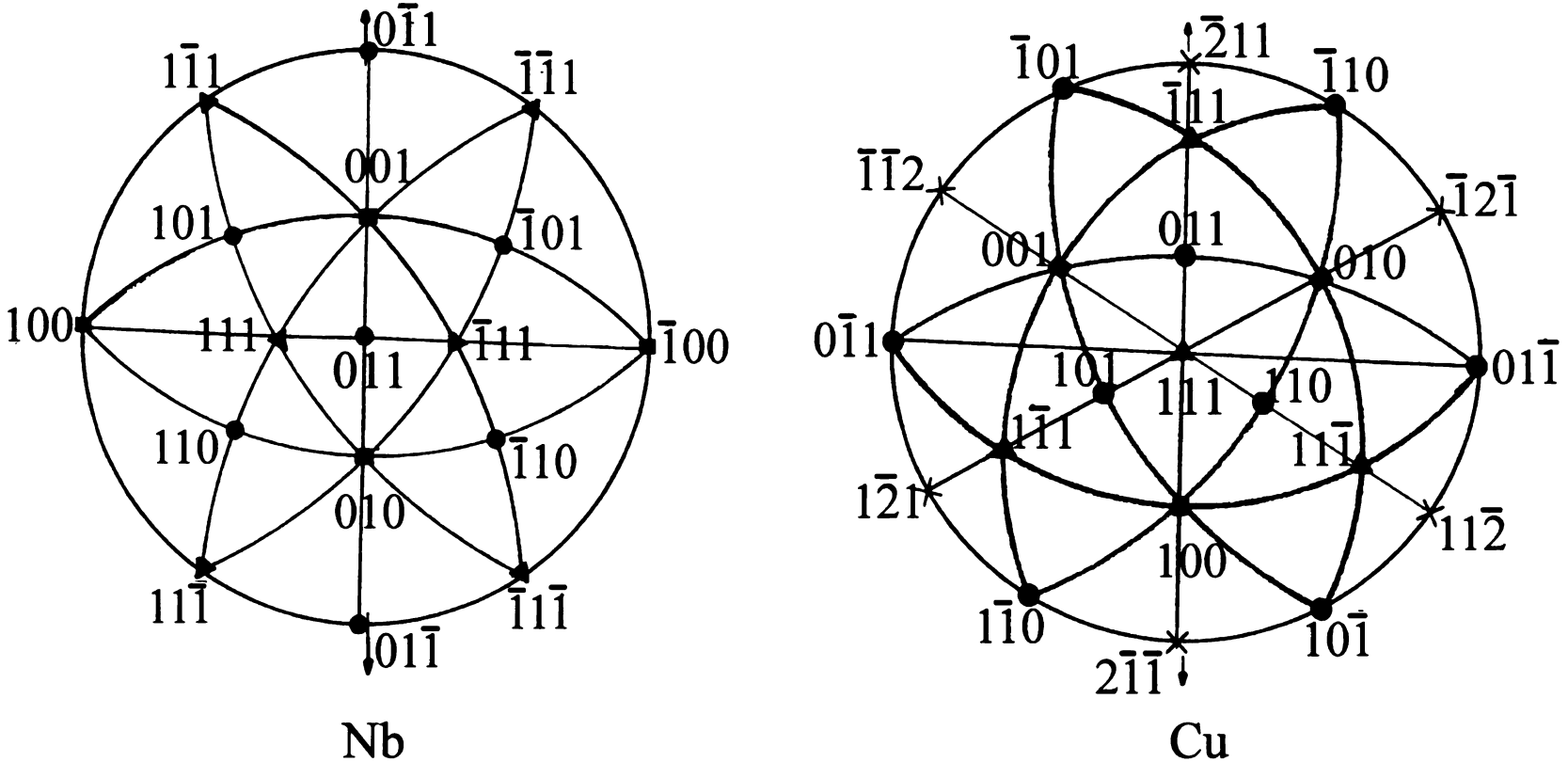

Figure 4.29 Stereographic projections of the epitaxial Nb and Cu films. The epitaxial relationship between the bcc Nb and fcc Cu variants was found to be the Nishiyama-Wasserman (N-W) relationship: $(110)_{bcc}Nb \,||\, (111)_{fcc}Cu$ with $[1\ \bar{1}\ 0]_{bcc}Nb \,||\, [1\ \bar{1}\ 2]_{fcc}Cu$.

4.6 SUMMARY

In this chapter, the nucleation and growth of epitaxial Cu film was reviewed. Cu films fabricated on epitaxial Nb substrates using sputter deposition were characterized using AFM and EBSP techniques. The AFM results showed that the surface topography is strongly affected by the temperature and surface quality of the substrates. Most of AFM results were reproducible. EBSP results revealed that all Cu films grown at a temperature higher than 150°C display 2 in-plane epitaxial variants corresponding to two stacking sequences of {111}fcc planes. The distributions of these twin variants were random. There was no correlation between the relative size of the twin variants and their distributions in the EBSP orientation map and the size of the islands and their distributions in the AFM image. These epitaxial Cu films take on the NW epitaxial relationship with respect to the Nb underlayer. The EBSP analysis of Cu films grown onto epitaxial Nb at room temperature revealed that two different orientation variants are present with a very small grain size. However, owing to degradation of the associated EBSPs and presence of the Kikuchi bands from both (111) twins variants in EBSP patterns, mapping of the orientation distributions was not possible.

Appendix 4.A

Summary of the sputtered Cu films grown on epitaxial Nb film in this study

Run # / Sample #	Type of Film	Growth Temperature
8-03	Nb / Cu 250 / 120 nm	750 °C / 350°C Both deposited using HTH
8-05	Nb / Cu 250 / 120 nm	750 °C / 450°C Both deposited using HTH
15-01	Nb / Cu 250 / 150 nm	658 °C / 350°C HTH / LTH Nb deposited using HTH Cu deposited using LTH
15-02	Nb / Cu 250 / 150 nm	654 °C / 475°C HTH / LTH
15-03	Nb / Cu 250 / 150 nm	654 °C / 250°C HTH / LTH
16-02	Nb / Cu 250 / 100 nm	730°C / 400°C HTH / LTH
17-02	Nb / Cu 250 / 150 nm	730 °C / 400°C HTH / LTH
18-01	Nb / Cu 250 / 80 nm	725°C / 250°C HTH /LTH
18-02	Nb / Cu 250 / 80 nm	725 °C / 430°C HTH /LTH
18-03	Nb / Cu 250 / 20 nm	750°C /250°C HTH /LTH
18-04	Nb / Cu 250 / 20 nm	750°C / 350°C HTH /LTH
19-01	Nb / Cu 250 / 20 nm	750°C / (150°C-Annealed at 250 °C) HTH /LTH
21-01	Nb / Cu 250 / 300 nm	735 °C / 350°C HTH /LTH
21-02	Nb / Cu 250 / 200 nm	735 °C / 350°C HTH /LTH
21-03	Nb / Cu 250 / 250 nm	735°C / 150°C-Annealed at 350Ann HTH /LTH
22-03	Nb / Cu 200-300 nm	750°C / 250 °C-Annealed at 350°C HTH /LTH

22-04	Nb / Cu 200-100 nm	750°C / 350°C-Annealed at 350°C HTH /LTH
23-01	Nb/ Cu 250 / 300 nm	750°C / 150 °C-Annealed at 150°C HTH /LTH
23-02	Nb / Cu 250 / 300 nm	750°C / 150°C - Annealed at 250°C HTH /LTH
23-03	Nb / Cu 250 / 300 nm	750 °C / 150 °C-Annealed at 350°C HTH /LTH
23-04	Nb / Cu 250 / 300 nm	750 °C / 150°C-Annealed at 500°C HTH /LTH
26-01	Nb / Cu 200 / 80 nm	750°C / 150 °C HTH /LTH
26-02	Nb / Cu 200 / 150 nm	750 °C / 150°C HTH /LTH
26-03	Nb / Cu 200 / 300 nm	750°C / (350-Annealed at 500) °C HTH /LTH
29-01	Nb / Cu 200/200 nm	750°C - (150-Annealed at 350) °C DR (4.1 A°/s)
29-02	Nb / Cu 200/200 nm	750°C - (150-Annealed at 350) °C Low DR (1 A°/s)
29-03	Nb / Cu 200/200 nm	750°C - (150-Annealed at 350) °C High DR (7 A°/s)
30-01	Nb / Cu 250/300 nm	750°C - 350°C Start with low DR
Leeds3K	Nb / Cu 20 / 300 nm	950 °C / 350°C
Leeds1K	Nb / Cu 20 / 300 nm	950 °C /350°C
Test	Cu on Si 300 nm	Room temperature

All of Nb buffer layers are post deposition annealed at 950°C for 20 minutes.
HTH = High temperature heater

LTH = Low temperature heater

DR = Deposition rate

Appendix 4.B

Effective Interaction Volume and Scanning Step Size

To obtain orientation distribution maps from the sputtered films, stage scanning or electron beam scanning was required. However, for scanning a large film area, stage scanning is more convenient. To collect reliable and relatively accurate orientation distribution maps, the scanning step size must be small enough to overlap the effective interaction volume during the scan. The proper scan size was found using the following procedure.

a) The electron beam was used to scan a selected sample area (an electron beam scan is more reproducible than a stage scan).

b) An area (10 μm x 1 μm) that contained a twin boundary was selected.

c) This area was scanned several times with different scanning step sizes (0.1– 2 μm) using the Channel 4 software.

d) The orientation maps that corresponded to each scanning step size were compared (size of each twin and location of the twin boundary).

In this study, 10 μm of an epitaxial Cu film was first scanned with step sizes of 2, 1.5, 1, 0.8, 0.5, 0.25, and 0.1 μm. The resulting orientation maps are shown in Figure 4.C.1. In all cases, four twin boundaries were identified. The size of twins was similar in the maps with the step size of 0.1 to 1 μm. However, in the scans with small step size (0.1 μm), Kikuchi bands from both variants were present at twin boundaries. At these twin boundaries, the Kikuchi bands could be indexed as either one of the twins. This causes uncertainty on the size of immediate twins. The orientation maps with step sizes of 2 and

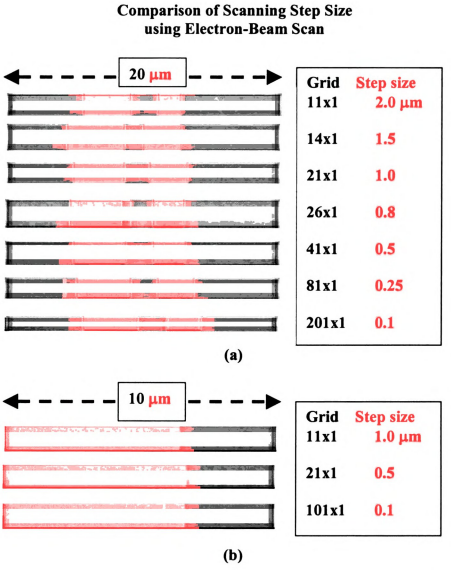

Figure 4.B.1 (a) Comparison of orientation maps obtained form 20 μm x 1 μm area of 300nm thick epitaxial Cu film, using different electron beam scanning step size. A 50μm aperture was used for these scans. (b) 10 μm x 1 μm area of different location on the same film and without aperture. All other parameter were the same during scans.

1.5 μm showed different sizes of twins, suggesting that the actual twin boundaries were missed. Using these results and many visual observations of the EBSP patterns during these scans, the step size of 1 μm was selected for this study. However, a few areas were scanned using 1 and 0.5 μm step sizes to ensure reproducibility of the orientation distribution maps.

Note that these orientation maps are qualitatively correct and they do not represent the exact twin distribution in these epitaxial Cu films.

4.7 REFERENCES:

1. Metallurgy and metallurgical engineering series, second addition, P.M. Hansen, McGraw-Hill book company, New York, (1958).
2. Ivan K. Schuller, Phys. Rev. Lett. **44**, 1597 (1980).
3. E. Bauer and Jan H. van der Merwe, Phys. Rev. B **33**, 3657 (1986).
4. A. Cebollada, J. L. Martinez, J. M. Gallego, J. J. de Miguel, R. Miranda, S. Ferrer, F. Batallan, G. Fillion, and J. P. Rebouillat, Phys. Rev. B **39**, 9726 (1989).
5. A. Cebillada, R. Miranda, C. M. Schneider, P. Schuster, and J. kirschner, J. Magn. Magn. Mat. **102**, 25 (1991).
6. M. Kato, Mat. Sci. engr. A1**46**, 205 (1991).
7. W. F. Egelhoff Jr. and M. T. Kief, Phys. Rev. B **45**, 7795 (1992).
8. D. Greig, M. J. Hall, C. Hammond, B. J. Hickey, H. P. Ho, M. A. Howson, M. J. Walker, N. Wiser, and Wright, J. Magn. Magn. Mat. **110**, l239 (1992).
9. K. Bröhl, P. Bödeker, N. Metoki, A.Stierle, and H. Zabel, J. Crystal Growth, **127**, 682 (1993).
10. A. Schreyer, K. Bröhl, J. F. Anker, C. F. Majkzak, Th. Zeidler, P. Bödeker, N. Metoki, and H. Zabel. Phys. Rev. B **47**, 15334 (1993).
11. M. J. Hall, B. J. Hickey, M. A. Howson, M. J. Walker, J. Xu, D. Greig, and N. Wiser. Phys. Rev. B **47**, 12785 (1993).
12. P. Bödeker, A. Abromeit, K. Bröhl, P. Sonntag, N. Metoki, and H. Zabel, Phys. Rev. B, **47**, 2353 (1993).
13. J. de la Figuera, J. E. Prieto, C. Ocal, and Miranda, Phys. Rev. B, **47**, 13043 (1993).

14. M. A. Howson, B. J. Hickey, J. Xu, D. Greig, P. Rhodes, and N. Wiser, Phys. Rev. B **49**, 9560 (1994).

15. J. Camarero, L. Spendeler, G. Schmidt, K. Heinz, J. J. de Miguel, and R. Miranda, Phys. Rev. Lett. **83**, 2448 (1994).

16. G.R. Harp and S.S. P. Parkin, Appl. Phys. Lett. **65**, 3063 (1994).

17. N.J. List, W.P. Pratt Jr, M.A. Howson, J. Xu, M.J. Walker, and D. Greig, J. Magn. Magn. Mater. **148**, 342 (1995).

18. G. R. Harp and S.S.P. Parkin, Thin Solid Films **288**, p. 315, (1996).

19. J. Camarero, T. Graf, J. J. de Miguel, G. Miranda, W. Kuck, M. Zharnikov, A. Dittschar, C. M. Schneider, and J. Kirschner, Phys. Rev. Lett. **76**, 4428 (1996).

20. H. T. Hardner, M. B. Wiessman, B. Miller, R. Loloee, S.S.P. Parkin, J. Appl. Phys. **79**, 7751 (1996).

21. D. J. Smith, A.R. Modak, T.A. Rabedeau, and S.S.P. Parkin, Appl. Phys. Lett., **71**. 1480 (1997).

22. J. Cmarero, J. Ferrion, V. Cros, L. Gomez, A. L. Vazquez de parga, J. M. Gallego, J. E. Prieto, J. J. de Miguel, and R. Miranda, Phys. Rev. Lett. **81**, 850 (1998).

23. X. W. Zhoh and H. N. G. Wadley, Acta Mater. **47**, 1063 (1999).

24. F. J. Himpsel, J. E. Ortega, G. J. Mankey, and R. F. Willis, Advances in Phusics, 47 511 (1998)

25. Z. Nishiyama, Sci. Rept. Tohoku Univ. **23**, 368 (1934).

26. G. Wasserman, Arch. Eisenhuttenwesen **16,** 647 (1933).

27. G. Kurdjumow and G. Sachs, Zeir. Physik1 **21**, 961 (1930).

28. L. A. Bruce and H. Jaeger, Phil. Mag. A, **38**, 223 (1978).

29. A. Bauer, J. Phys.: Condens. Matter **11**, 9365 (1999).

30. H. M. Koduvely and A. Zangwill, Phys. Rev. B, **60**, R2204 (1999).

31. J. Drucker, Phys. Rev. B, **48**, 18203 (1993).

32. S. C. Jain, A. H. Harker, and R. a. Cowley, Phil. Mag. A, **75**, 1461 (1997).

33. U. Wolf, F. Ernst, T. Muschik, M W. Finnis, and H. F. Fischmeister, Phil. Mag. A, **66**, 991 (1992).

34. T. Muschik, W. Laub, U. Wolf, M. W. Finnis, and W. gust, Acta metall. mater. **41**, 2163 (1993).

35. A. Scmidt, F. Ernst, M. W. Finnis, and V. Vitek, Phys. Rev. lett. **75**, (2160 (1995).

36. A. L. Medlin, G. H. Campbell, and C. B. Carter, Acta Mater. **46**, 5135 (1998).

37. M. Ohring, The Materials Science of Thin Films, Academic Press, Inc. San Diego CA (1992).

38. A. J. Wilkison, and D. J. Dingly, Acta metall. Mater. **40**, 3357 (1992).

39. R. Loloee, P. Duxbury, Private communications.

40. H. Geng, J. W. Heckman, W. P. Pratt Jr, J. Bass, F. J. Espinosa, S. D. Conradson, D. Lederman, and M. A. Crimp, J. Appl. Phys., **86**, 4166 (1999).

41. T. E. Mitchell, Y. C. Lu, A. J. Griffin, M. Nastasi, and H. Kung, J. Am. Ceram. Soc., **80**, 1673. (1997).

42. P. RAI-Choudhury, Handbook of Microlithography, Micromachining and Microfabrication, , V.1, page 205, SPIE Press, London, (1997).

43. J. S. Greeneich, J. Appl. Phys., **45**, 5264 (1974).

44. N. Samoto, R. Shimizu, H. Hashimoto, I. Adesida, E. Wolf, and S. Nama, J. Vac. Sci. Technol. B. **1** 1367 (1983).

CHAPTER 5

GROWTH OF Co AND Py FILMS ON EPITAXIAL Cu

5.1 INTRODUCTION:

In chapters 3 and 4, the details of the growth of epitaxial Nb(110) and Cu(111) were presented. The next step towards making epitaxial magnetic multilayers and spin-valves in a preferred (111) orientation is to deposit Co or Py films onto the epitaxial Cu(111) layer.

In this chapter, the nucleation and growth of Co and Py are first reviewed, followed with the details of sputter deposition of the Co and Py films. Also included in this chapter are the results of the AFM and EBSP characterization of the sputter-deposited Co and Py films (grown at 460°C and 90°C). A discussion of the growth process of these sputter deposited films, based on the AFM and EBSP analysis, concludes this chapter.

5.2 GROWTH OF Co FILMS ON EPITAXIAL Cu(111)

5.2.1 Nucleation and Growth --- a Review:

Background Co is an allotropic metal that can grow with either a fcc or hcp crystal structure, depending on the nucleation sites and growth conditions. At room temperature, bulk Co exists with an hcp crystal structure, while at 417°C, it undergoes structural phase transition to an fcc crystal structure.

In thin films, the situation is more complicated. During hetero-epitaxial growth of Co on Cu(111), the growing Co layers have the freedom to continue to stack either with the

substrate in an fcc sequence or in the hcp sequence. The hcp sequence is more favorable energetically at room temperature.

Before reviewing the nucleation and growth of Co on a Cu(111) substrate, a demonstration of the geometrical relation between Co and Cu(111) will help form a biases for the nucleation and growth discussion. In Figure 5.1, a superimposed atomic arrangement (unrelaxed) of Co(111) and Cu(111) with a 2% lattice mismatch is shown. In this figure an orientation relationship of Co(111)<110> || Cu(111)<110> is shown. The areas where Co atoms coincide with Cu atoms appear with complete circles (light areas) and they are unfavorable areas for nucleation (as described in chapter 4). The darker areas are coherent and are convenient sites for nucleation of coherent islands.

Nucleation, growth, and twin formation: The nucleation, growth, and structural characterization of Co films on epitaxial $Cu(111)_{fcc}$ substrates (grown at room temperature) have been investigated by many researchers [1-12].

Heinz et al. [2] have investigated the crystallography of ultra-thin Co films grown epitaxially on Cu(111). They reported that from the lattice misfit point of view (2%), a pseudomorphic growth of Co ($Co(111)_{fcc}$) was expected. However, their results did not agree with the expectation due to the freedom of the fcc or hcp stacking. LEED studies showed that up to 2 ML of cobalt films largely copies the fcc stacking of the substrate. The growing film is increasingly dominated by hcp stacking when this thickness is exceeded.

Tonner et al. [5] have also reported similar results using angle-resolved x-ray-photoelectron diffraction and LEED. They found that the initial growth of Co (with

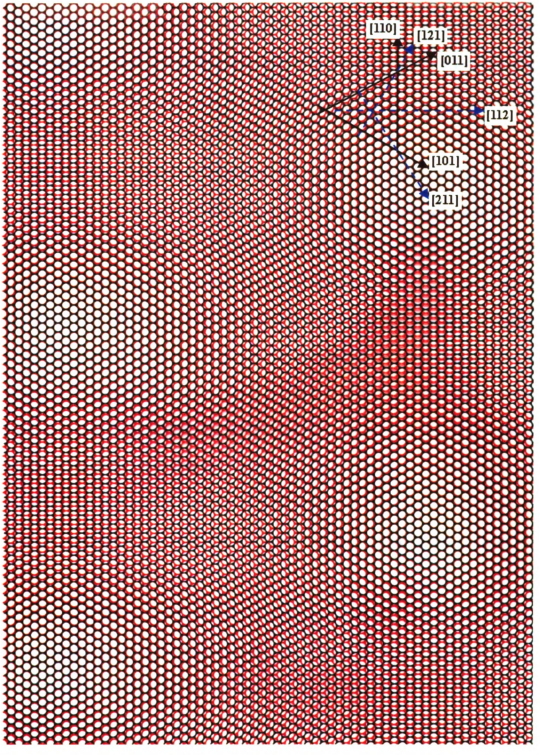

Figure 5.1. A superimposed atomic arrangement (unrelaxed) of Cu/Co with about 2% lattice mismatch. The lighter areas are coincidence sites between Co and Cu atoms. The darker areas are coherent with a large coherency length and are convenient sites for nucleation of coherent islands.

the substrate maintained near room temperature) is in the metastable fcc phase. The first two monolayer Co atoms continue the stacking sequence of the fcc(111) Cu substrate through a layer-by-layer and pseudomorphic growth mode. After these two layers up to 10 ML (~2.5 nm), about 50% of the Co atoms still continue the fcc(111) (ABCABC...) and 50% undergo a change of stacking to hcp (ABAB...).

The growth and structure of Co thin films on Cu(111) substrates have also been investigated by Kief and Egelhoff [6] using x-ray-photo electron, Auger electron forward scattering, LEED, and RHEED. They noted that, growth of Co on Cu(111) at room temperature is generally not a layer-by-layer FM growth mode. Also, there was much larger portion of fcc stacking than hcp stacking in the films grown at room temperature.

In a STM study of the growth of fcc Co on Cu(111) at room temperature, de la Figuera et al. [7] reported that the growth is not layer-by-layer and the first Co monolayer does not wet the Cu substrate. Rather it grows in the form of bilayer islands. The existences of large (30 Å) triangular Co islands were found to nucleate at each atomic terrace with two orientations, rotated 60° with respect to each other. Both orientations have equal probability and similar island size. These Co twins could coincide on Cu twins or grow independently.

Bröhl et al. [8] have used the RHEED to study epitaxial growth of Co films on Cu(111). They reported that at a substrate temperature below 100°C the Co films grow on Cu(111) pseudomorphically in the metastable fcc phase up to 20 nm.

Unfortunately, these reviews do not provide a clear picture of the nucleation, growth and twin formation of the epitaxial Co films fabricated at low temperature (below 100°C). Nucleation and growth are simpler at a high temperature (460°C). Co films

grow with a fcc structure, however, there is significant interdiffusion and alloying between Co and Cu (about 10% miscibility at 400°C) [2, 13].

Most of the samples in the reviewed articles were fabricated using MBE. There are a few reports in which the samples were fabricated by different techniques such as sputtering deposition or pulsed laser deposition [1,6]. Similar to those discussed above, there were no clear and consistent conclusion of how the epitaxial $Co(111)_{fcc}$ nucleates and grows as well as how far the fcc layer can grow.

For this study, EBSP has been used to identify the orientation (in fcc phase or possible hcp phase) of 20 nm to 150 nm sputter deposited Co films. In the next two sections, the experimental results of AFM surface topography analysis and EBSP orientation distribution analysis are presented. Based on the results from these two sections, the growth process in the sputter deposited Cu film for this study will be discussed. Note that due to limitation of EBSP for thin films, the Co films that were deposited for this study are much thicker than those that have been reviewed.

The crystallographic and physical properties of Co are summarized in Table 5.1.

5.2.2 Sputter Deposition of Co Films

As described in the Chapter 4, after post deposition annealing of a Cu layer, the low temperature heater was either removed to cool the substrate to about room temperature or warmed up to a higher temperature (460°C) for high temperature deposition of Co or Py films.

Table 5.1

CRYSTALLOGRAPHIC DATA

Element:	Co- Cobalt	Co-Cobalt
Crystal system:	Hexagonal – hcp	Cubic – fcc
a = b = c =	0.2507 nm 0.2507 nm 0.4069 nm	0.3544 nm 0.3544 nm 0.3544 nm
Unit cell volume:	0.0221 nm^3	0.0445 nm^3
# of atom in unit cell:	4	4
Atomic radius:	Co = 0.125 nm	Co = 0.125 nm
$d_{(h,k,l)}$	$d_{(0001)}$ = 0.2171 nm	$d_{(111)}$ = 0.2046 nm
Symmetry elements:	A single 6-fold rotation axes	Four 3-fold rotation axes
Melting point:	1495 °C	1495 °C

5.2.3 AFM Analysis:

Co samples with film thicknesses ranging from 20 nm to 150 nm were grown on 20 nm of epitaxial Cu films at substrate temperatures of 80°C and 460°C. The surface topography of each film was examined using AFM. In general the growth temperature, film thickness, and substrate topography affected the morphology of the sputtered Co films. The results of AFM analysis are categorized as follows:

- Effect of substrate temperature on surface topography of the Co films.
- Effect of film thickness on surface topography of the Co films.

5.2.3.1 Effect of substrate temperature on surface topography of the Co films

All of the Co films were grown on 20 nm epitaxial Cu(111) substrates. One set of Cu substrates was deposited at 350°C and the second set was deposited at 150C° and post deposition annealed at 350C°.

20 nm thick samples The surface morphology of the 20 nm Co films deposited at 460°C and 80°C was hardly affected by the substrate temperature. Figures 5.2(a) and (b) show the atomic-force-microscopy images and line trace surface analyses of 20 nm thick Co films. These Co films have been grown on a 20 nm epitaxial Cu film (grown at 350°C) at substrate temperatures of 460°C and 80°C. The image RMS roughness of Co films deposited at above temperatures were similar, approximately 16 nm. The surface topography of these two samples is very similar, with similar island sizes.

100 nm thick samples Despite the fact that the 100 nm thick Co films were deposited on a similar substrate to that used for the 20 nm thick samples, they show a significantly different surface topography. In Figure 5.3, 100 nm Co films grown at

AFM Images of 20 nm Thick Co Film
Deposited at Substrate Temperature of 460°C and 80°C.

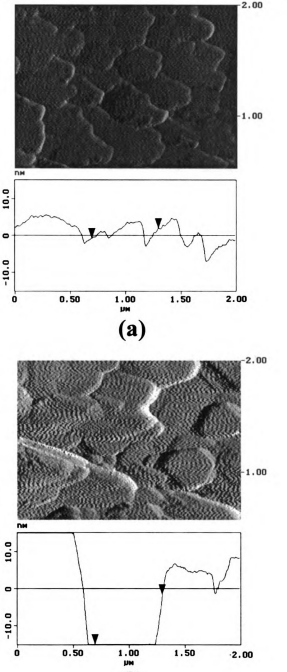

Figure 5.2 Atomic-force-microscopy images and line trace surface analyses showing the surface topography of 20 nm thick Co films grown on 20 nm epitaxial Cu(111) (grown at 350°C) at substrate temperature of: a) 460°C and b) 80°C. The image RMS roughnesses of both films are about 16 nm.

AFM Images of 100 nm Thick Co Film
Deposited at Substrate Temperature of 460°C and 80°C

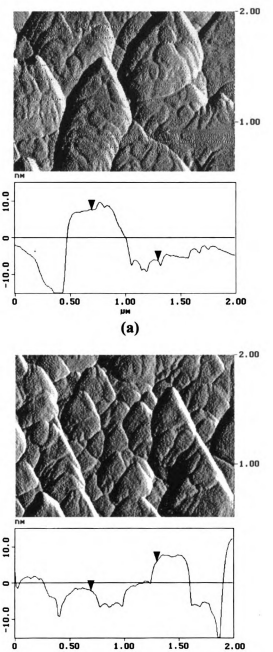

Figure 5.3 Atomic-force-microscopy images and line trace surface analyses showing the surface topography of 100 nm thick Co films grown on 200 nm epitaxial Cu(111) (grown at 350°C) at substrate temperature of: a) 460°C and b) 80°C. The image RMS roughnesses are about 11 and 4 nm, respectively.

460°C and 80°C are shown. The images RMS roughness are about 11 nm and 4 nm, respectively. The islands are similar in shape but larger in the film deposited at 460°C.

150 nm thick samples Also, two 150 nm thick Co films were deposited on epitaxial Cu films at substrate temperatures of 80°C and 460°C. AFM images and line trace surface analyses of 150 nm Co films grown at 460°C and 80°C are show in Figure 5.4. The image RMS roughness of these two Co films were about 2.6 and 3 nm, respectively. Note that these two samples were fabricated during a separate run and on a different sapphire substrate (with different surface profile) than the previous samples. The 150 nm thick Co film deposited at high temperature (460°C) has a smoother surface than low temperature deposited Co film.

The overall results of the AFM studies (for all thiknesses) revealed that the films grown at 460°C mostly have larger island sizes and smoother surfaces. This is possibly due to larger nucleation sites and coalescence between the islands. In section 5.2.3, the orientation of these films will be investigated using EBSP.

5.2.3.2 Effect of film thickness on surface topography of the Co films.

Since these Co films were deposited at separate sputtering runs on substrate with different surface profile, the comparison of the surface topographies as a function of thickness cannot be completely assessed and has therefore been omitted.

5.2.4 EBSP Analysis

The EBSP technique was used to examine the crystallographic nature of the sputtered Co films. The results of the EBSP data analysis have been categorized in a similar way to the AFM analysis.

AFM Images of 150 nm Thick Co Film
Deposited at Substrate Temperature of 460°C and 80°C.

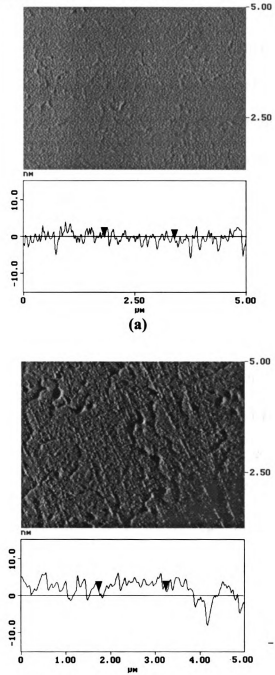

Figure 5.4 Atomic-force-microscopy images and line trace surface analyses showing the surface topography of 150 nm Co films grown on 20 nm epitaxial Cu(111) (grown at 150°C and post deposition annealed at 350°C) at substrate temperatures of: a) 460°C and b) 80°C. The image RMS roughnesses of about 2.6 and 3.1 nm, respectively.

5.2.4.1 Temperature dependence, 80°C vs. 460°C

As discussed in Chapter 4 (Section 4.5.2.2 Limit of EBSP), EBSPs from 100 nm thick (and thinner) samples were partially affected by backscatter contributions from the underlying Nb, and some of the patterns could not be indexed. In the case of Co films, this same problem exists for 20 and 100 nm thick samples. Presumably, for films thinner than 150 nm the underlying epitaxial Cu (and Nb in 20 nm Cu thick films) will contribute significantly to the patterns, but since Co and Cu may have the same crystal structure and very similar lattice parameters, the EBSP patterns from the Co and underlying Cu can merge and be indistinguishable. Therefore, only the EBSP study of 150 nm thick Co films is discussed.

EBSP data was collected randomly from different locations on both 150 nm thick Co films. Similar to the epitaxial Cu films, the pole figures obtained from the EBSP data of the 150 nm thick Co films grown at 460°C revealed that two different orientation variants were present. Both variants display <111> growth normals, consistent with the growth occurring on the close-packed {111} planes in the fcc Co. Electron backscatter patterns of the Co films were very sharp for samples grown at a substrate temperature of 460°C. The pole figure obtained from the EBSP data of the 150 nm Co films grown at 80°C, however, revealed only one orientation variant. There was also substantial pattern degradation for the samples grown at a substrate temperature of 80°C. Figure 5.5 shows EBSP patterns of these two 150 nm thick epitaxial Co films grown on 20 nm epitaxial Cu at substrate temperatures of 460°C and 80°C. In figure (a) a sharp pattern from one of the variants is shown. The two orientations were distinguished by a change in the Kikuchi bands in the pattern. However, after careful observation of the patterns during

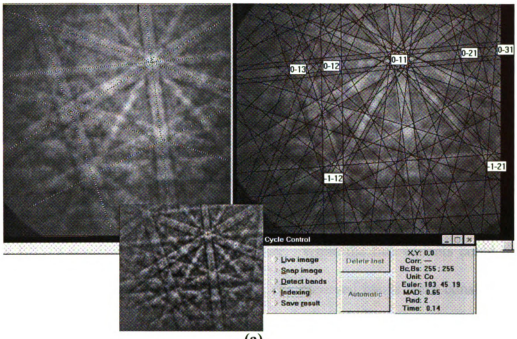

(a)

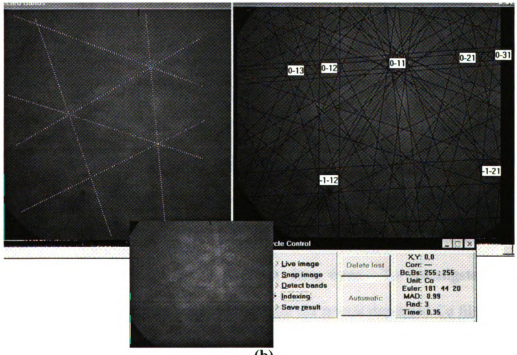

(b)

Figure 5.5 EBSPs from 150 nm epitaxial Co films deposited on 20 nm epitaxial Cu films (grown at 150°C and post deposition annealed at 350°C) at substrate temperatures of: (a) 460°C and (b) 80°C.

the scanning, it was noticed that the patterns did not change during the scanning processes and had relatively the same appearance (as shown in figure 5.5(b)). The presence of these bands in the EBSP patterns indicate that both variants coexist within the EBSP interaction volume and the indexing software does not reliably distinguish between these bands.

All patterns from the 150 nm thick Co films grown at 460°C were easily indexed as consistent with the fcc structure and, under no circumstances, did any of the Co films display EBSPs consistent with the hcp structure. While the two variants could not be distinguished in 150 nm film grown at 80°C, the observed bands were consistent with two fcc variants and no obvious evidence of the hcp structure was found.

To measure the size and distribution of the variants in the epitaxial Co films grown at 460°C, the samples were mapped using stage control scanning. An orientation distribution map of 150 nm thick Co film grown on a 20 nm thick epitaxial Cu film with a substrate temperatures of 460°C is shown in Figure 5.6.

The epitaxial Co films grown at 460° have a similar twin distribution to epitaxial Cu (grown at an elevated temperature). However, based on the reviewed articles [1-12] for the case of Co films grown at 80°C, there is a possibility of the existence of hcp Co clusters along with two fcc(111) variants in these films. To investigate this issue, HRTEM is needed to identify and to characterize the sputter deposited Co films, which is beyond the scope of the present study.

The average grain size of the twin variants in the epitaxial Co film grown at 460°C, was approximately 5 μm with a relative grain area varying between 42% and 58%.

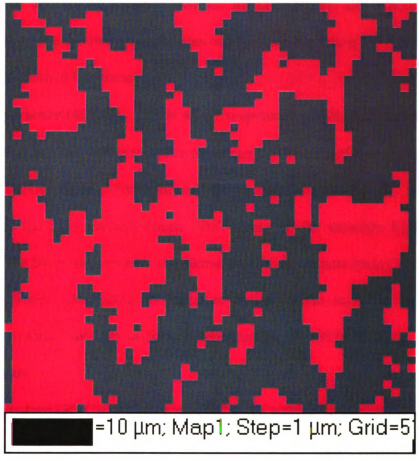

Figure 5.6. Orientation map of a 150 nm epitaxial Co film grown at 460°C on 20 nm epitaxial Cu film (grown at 150°C and post deposition annealing of 350°C) showing the distribution of the twin variants.

5.2.5 Growth Process

Based on the information obtained from the literature review and experimental AFM and EBSP results, the following conclusions can be made regarding the growth processes in the sputter deposited Co films:

At high temperature (460°C): This is a hetero-epitaxial growth (Co grows on Cu with same orientation but has different lattice parameter). The size of islands appear on the surface topography (from AFM analysis, for example figure 5.3(a)), and size and distribution of the twin variants (from EBSP analysis, for example figure 5.6), are suggestive of the SK growth mode. The formation of two variants (twin) is similar to the epitaxial Cu films. According to literature review, these twins could follow the underlayer Cu twins structures or form independently. A HRTEM study is needed to resolve this issue.

At low temperature (80°C): At low temperature, the arriving atoms do not have enough time to find or move toward a step edge or nucleated sites. Rather nucleation take place spontaneously as an island on top of each other. This causes the formation of a misfit distortion network within the film and thus a rougher surface and strain within the film. The smaller size islands seen in surface topography (see figure 5.3 (b)) and the existence of very small twin variants (not resolved in EBSP) as well as pattern distortion, are supportive of the given conclusion which was obtained from the literature review. The distortion of the EBSP patterns would be the result of such strain. Again HRTEM study is needed for possible clarification.

5.3 GROWTH OF Py FILMS ON EPITAXIAL Cu(111)

5.3.1 Nucleation and Growth --- a Review:

Background Permalloy (Py) is often substituted for Co in magnetic multilayers and is one of the ideal and frequently used ferromagnetic materials in both types of hybrid and exchange-biased spin-valves. Py is an alloy of Ni and Fe ($Ni_{.8}Fe_{.2}$) with a fcc derivative $L1_2$ structure. A typical exchange-biased spin-valve can be grown in either of the following orders.

- Nb-Cu-FeMn-Py-Cu-Py : note the first Py must be deposited on FeMn.
- Nb-Cu-Py-Cu-Py-FeMn : note the first Py must be deposited on Cu.

In polycrystalline samples, the order is not very critical. However, in epitaxial samples the substrate (buffer layer) may be a crucial issue.

The growth of Py on Cu(111) (or FeMn(111)) should accrue by simple, hetero-epitaxial growth of an fcc metal on top of another fcc metal, with relatively small lattice mismatch (1.3%). Therefore, a well-defined pseudomorphic layer-by-layer growth up to a large number of monolayers is expected [2]. Unfortunately, the nucleation and growth of Py has not been investigated by researchers.

In the next two sections, the experimental results of the AFM surface topography analysis and EBSP orientation distribution analysis are presented. The growth process then will be discussed based on the outcomes of the AFM and EBSP analyses.

The crystallographic and physical properties of Py and Cu are summarized in Table 5.2.

Table 5.2

CRYSTALLOGRAPHIC DATA

Alloy or Element:	Py™-Permalloy	Cu-Copper
Crystal system:	Cubic – fcc $L1_2$	Cubic – fcc
a = b = c	0.352 nm	0.36148 nm
Unit cell volume:	0.0447 nm^3	0.0467 nm^3
# of atom in unit cell:	4	4
Atomic radius:	Py = *NA	Cu = 0.128 nm
$d_{(h,k,l)}$	$d_{(111)}$ = 0.205 nm	$d_{(111)}$ = 0.2078 nm
Symmetry elements:	Four 3-fold rotation axes	Four 3-fold rotation axes
Melting point:	1480 °C	1083 °C

*NA : Py ($Ni_{80}Fe_{20}$) has a fcc derivative $L1_2$ structure and the dose not have a single value for the atomic radius.

5.3.2 AFM Analysis

For this study, a few 200 nm thick Py films were deposited on 20nm epitaxial Cu films at substrate temperatures of 350°C and 90°C. The surface topography of each film was examined using AFM. The surface topographies of the sputtered Py films were affected by the growth temperature and substrate topography. The results of the AFM analysis are categorized as follows:

- Effect of the substrate temperature on the surface topography of the Py films.
- Effect of the buffer layer on the surface topography of the Py films.

Effect of the substrate temperature on surface topography of the Py films.

The AFM analysis showed that Py films had surface morphologies similar to epitaxial Co films. Two sets of 200nm thick Py films were deposited at 350°C and 90°C on 20 nm thick epitaxial Cu films. The epitaxial Cu films were grown at a substrate temperature of 150°C and post deposition annealed at 350°C. Figure 5.7 shows atomic-force-microscope images and corresponding line trace surface analyses of 200 nm thick Py films grown on 20 nm epitaxial Cu film at substrate temperatures of 350°C and 90°C. The Py sample grown at 350°C has relatively large islands, while the sample grown at 90°C seems to be very rough with very small grains. In Figure 5.8, the AFM images and the corresponding line trace surface analyses of 200 nm thick Py films grown on 20 nm epitaxial Cu films at substrate temperatures of 350°C and 90°C (deposited during different sputtering runs) are shown. The Py sample grown at 350°C has relatively smooth surface topography, while the sample grown at 90°C seems to be rougher with many small interconnected islands.

AFM Images of 200 nm Thick Py Films
Deposited at Substrate Temperatures of 350°C and 90°C.

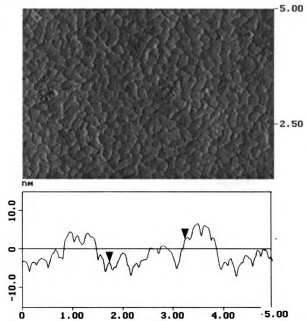

(a)

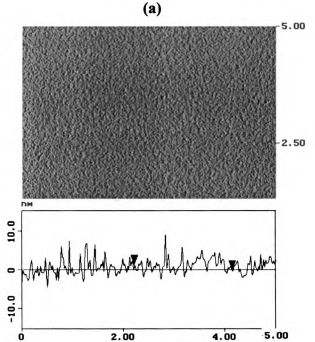

(b)

Figure 5.7 AFM images and line trace surface analysis of 200 nm thick Py films deposited on 20 nm epitaxial Cu films at substrate temperatures of 350°C and 90°C. The epitaxial Cu films were deposited at 150°C and post deposition annealed at 350°C.

AFM Images of 200 nm Thick Py Films
Deposited at Substrate Temperatures of 350°C and 90°C.

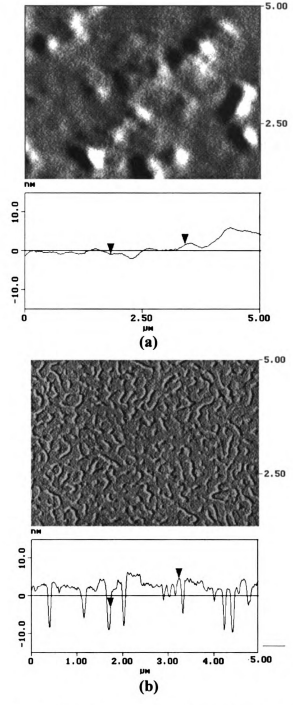

Figure 5.8 AFM images and line trace surface analyses showing the surface topography of 200 nm Py films grown on 20 nm epitaxial Cu(111) (grown at 150°C and post deposition annealed at 350°C) at substrate temperature of: a) 350°C and b) 90°C. The image RMS roughnesses are about 2 and 9 nm, respectively.

Effect of buffer layer on surface topography of the Py films.

To investigate the effect of buffer layer on epitaxial Py films from crystallographic point of view one sample was grown with 8 nm of FeMn deposited on a 20 nm epitaxial Cu film at a substrate temperature of 90°C prior to the deposition of 200 nm thick Py film. The AFM results showed that the 200 nm Py deposited on the 8 nm of FeMn had a very smooth surface compared to those deposited directly on a Cu substrate. An AFM image and line trace surface analysis of 200 nm thick Py films deposited on Cu film (grown at 150°C and post deposition annealed at 350°C) (a) and FeMn film (b) are shown in Figure 5.9.

5.3.3 EBSP Analysis

Similar to the EBSP analysis of Co film, the EBSP analyses of Py films grown at a substrate temperature of 350°C revealed that two different variants are also present in these films. Both variants display <111> growth normals, consistent with growth occurring on the close-packed {111} planes in the fcc Py. These epitaxial Py films have similar variant distributions to those of the epitaxial Cu and Co films. Figure 5.10 shows EBSP patterns of these two 200 nm thick epitaxial Py films grown onto 20 nm epitaxial Cu at substrate temperatures of 350°C and 90°C. In figure (a), a sharp pattern from one of the variants is shown. Similar to Cu and Co, the two orientations were distinguished by a change in the Kikuchi bands in the pattern. In figure 5.11 an orientation map of the distribution of the two variants in a 200 nm thick epitaxial Py film deposited at 350°C is shown. The average twin size in epitaxial Py films grown at high temperature was about 5 μm, and a typical relative grain area varies between 44% and 56%.

AFM Images of 200 nm Thick Py Films
Deposited on Different Buffer Layer

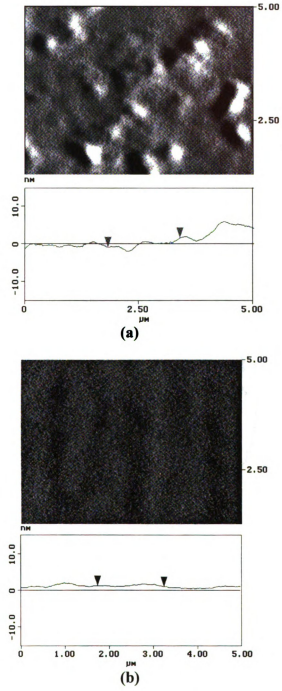

Figure 5.9 Atomic-force-microscopy images and line trace surface analyses showing the surface topography of 200 nm Py films grown at 90°C on a) 20 nm of epitaxial Cu(111) (grown at 150°C and post deposition annealed at 350°C and different substrate than in figure 5.6). b) 8 nm of FeMn. The RMS roughnesses are about 2 and 0.9 nm, respectively.

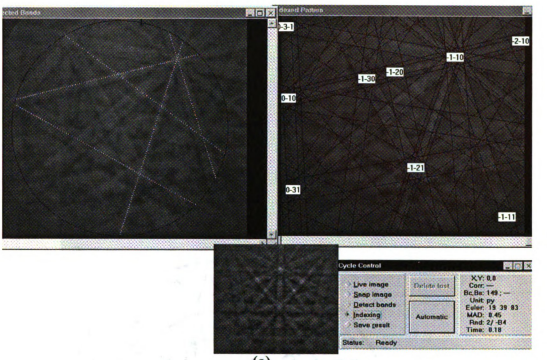

(a)

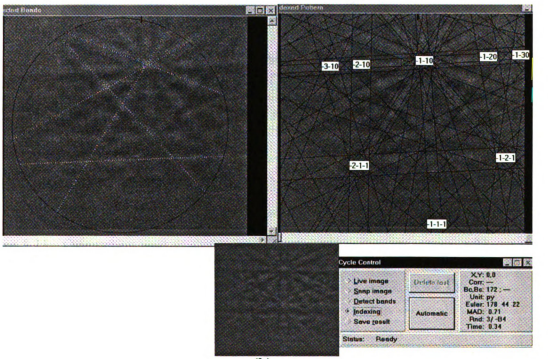

(b)

Figure 5.10 EBSPs from 200 nm thick epitaxial Py films deposited on 20 nm thick epitaxial Cu films (grown at 150°C and post deposition annealed at 350°C) at substrate temperatures of: (a) 350°C and (b) 90°C.

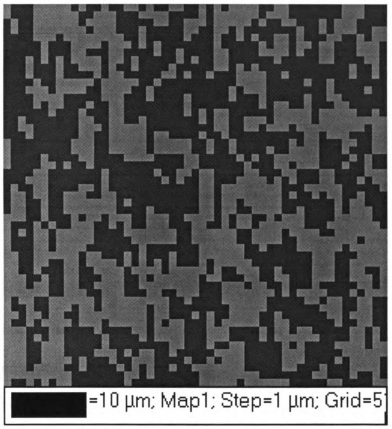

Figure 5.11. Orientation map of 200 nm thick epitaxial Py film grown on a 20 nm thick epitaxial Cu film (grown at 150°C and post deposition annealing of 350°C) at a substrate temperature of 350°C showing the distribution of the twin variants in the Py.

The EBSPs of Py films grown at a substrate temperature of 90°C showed significant pattern degradation, which is similar to that observed in the Co films (figure5-10(b)). However, all of the patterns were easily indexed for the fcc structure. The distortion and degradation of patterns is again likely caused by strains in the film resulting from an increase in the numbers of misfit dislocations, threading dislocations, and point defects. Since the two orientation variants are distinguished by a change in the Kikuchi bands in the patterns, mapping of the two orientation variants was not successful for 90°C films, however, because of pattern degradation and presence of Kikuchi bands from both variants.

Effect of the buffer layer on Py film EBSPs of Py films grown on Cu at 350°C and 90°C are shown in part (a) and (b) of Figure 5.12. An EBSP of Py film deposited on FeMn at room temperature is shown in part (c) of the same figure. In the case of Py/FeMn, EBSP patterns from the Py film grown onto 8 nm of FeMn at room temperature were relatively clear and sharp. This increase in Py film pattern sharpness indicated that there was less strain in the Py film grown on FeMn film than those grown on Cu film [14].

The released of strain in Py film deposited on FeMn buffer layer had been also observed by Tang et al.[14], using HRTEM and XRD. Their results revealed that the misfit strain between the FeMn layer and Py is released by the formation of a dome shape on the FeMn surface rather than by the formation of misfit dislocations at the interface between the two layers.

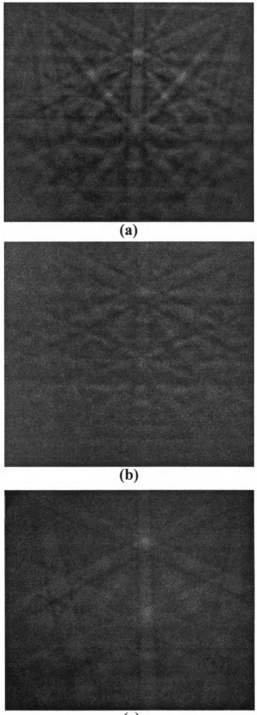

Figure 5.12 EBSPs from 200 nm epitaxial Py films deposited on 20 nm epitaxial Cu (grown at 150°C and post deposition annealed at 350°C) at substrate temperature of: (a) 350°C and (b) 90°C. (c) a EBSP pattern of a 200 nm epitaxial Py film deposited on 8 nm of FeMn (grown at 90°C) at a substrate temperature of 350°C.

5.4 DISCUSSION

Unfortunately, in all three cases of Cu, Co, and Py films grown at an ambient temperature (below 100°C), the indexing software does not reliably distinguish between mixed Kikuchi bands, which originated from both variants. There was also some degree of distortion in all three cases. However, the distortions of the EBSP patterns of Co and Py grown at 90°C were more severe than those in Cu films grown at 90°C. There are a few possible factors that could cause such a distortion. Among them are surface energy of each layer, lattice mismatch between two consecutive layers, and atomic radius of each deposited material. Each of these factors could affect the interface energy, the nucleation and growth rates of the islands, and the density and type of dislocations and point defects.

The surface energy, lattice mismatch, and atomic radius of Nb, Cu, Co, Py are tabulated in table 5.3 for comparison. To have more data for comparison, two Ag films have also been grown on epitaxial Nb substrate, similar to Cu films, one at 350°C and the second one at 90°C. Ag has different surface energy, lattice mismatch (with Nb), and atomic radius than Cu or Co. The value of surface energy, lattice mismatch, and atomic radius of Ag are also included in the table 5.3. The details of this experiment are given in appendix 5.A. EBSP analyses of the epitaxial Ag films grown at 350°C revealed two different (111) orientation variants, and the NW epitaxial relationship with the Nb substrate. The variant distributions were compared to those found in the epitaxial Cu films grown at 350°C. Again, the variants did not display any particular pattern or morphologies. The EBSP patterns of Ag film grown at a substrate temperature of 90°C showed some degradation, more similar to Co and Py cases.

Table 5.3

Comparison of Lattice Mismatch, Atomic Radius, and Surface Energy of Nb, Cu, Ag, Co, and Py

System	Surface energy	Lattice mismatch	Atomic radius
Nb - Cu	3 – 1.9 J/m^2	12 %	0.143 nm - 0.128 nm
Nb - Ag	3 – 1.3 J/m^2	1%	0.143 nm - 0.144 nm
Cu - Co	1.9 – 2.7 J/m^2	2%	0.128 nm - 0.125 nm
Cu - Py	1.9 – ~2.7 J/m^2	1.3%	0.128 nm -

Comparisons of different variables in Table 5.3 suggest that the surface energy of a given material are effecting the EBSP patterns. It seems that when the surface energy of the overlayer is greater than surface energy of the substrate, the degradation in the EBSP will appear.

5.5 SUMMARY

In this chapter, the nucleation and growth of two ferromagnetic materials (Co and Py) on epitaxial Cu film were reviewed. All of the sputter deposited films were characterized using AFM and EBSP techniques. The AFM results demonstrated that the surface topography is affected strongly by the temperature and surface quality of the substrates. EBSP results revealed that all Co and Py films grown at high temperature display two in-plane epitaxial variants corresponding to two stacking sequences of {111}fcc planes. The EBSP analysis of Co and Py samples grown at 90°C revealed that two different orientation variants are present. However, due to degradation of the associated EBSP patterns and presence of Kikuchi bands from both variants, mapping of the orientation distributions was not possible.

APPENDIX 5.A

Ag has a fcc structure and the Ag/Nb lattice mismatch is 1% with an atomic radius difference of 0.7% (see table 5.4). Ag can grow with the NW or KS epitaxial relationship onto an epitaxial Nb substrate. A properly superimposed atomic arrangement (unrelaxed) of Ag on Nb (with the NW relationship) is shown in Figure 5.A.1.

Similar to growth of epitaxial Cu films, a few Ag films were grown on 250 nm epitaxial Nb at substrate temperatures of 350°C and 90°C. The EBSP results of Ag films grown at 350°C and 90°C were similar to the epitaxial Cu. Figure 5.A.2 illustrates the EBSPs of epitaxial Ag grown at 350°C and 90°C. Figure 5.A.3 shows the orientation distribution map of 300 nm epitaxial Ag grown on 250 nm epitaxial Nb. The epitaxial relationship between the sputter deposited epitaxial bcc Nb and fcc Ag films, was found by removing part of the Ag film and collecting EBSP data from an adjacent section of Nb and Ag. The resulting (100), (110), and (111) pole figures were used to plot the stereographic projection of both Nb and Ag. By superimposing the Ag stereographic projection on the Nb, the result suggests that $(110)_{bcc}Nb \parallel (111)_{fcc}Ag$, with $[1\ \bar{1}\ 0]_{bcc}Nb \parallel [1\ \bar{1}\ 2]_{fcc}Ag$ and $[\ \bar{1}\ 0\ 0]_{bcc}Nb \parallel [0\ 1\ \bar{1}]_{fcc}Ag$, which agrees with the NW relationship.

Table 5.4

CRYSTALLOGRAPHIC DATA

Element:	Nb–Niobium-Columbium	Ag-Silver
Crystal system:	Cubic – bcc	Cubic – fcc
a = b = c =	0.33067 nm 0.33067 nm 0.33067 nm	0.4086 nm 0.4086 nm 0.4086 nm
Unit cell volume:	0.0359 nm^3	0.0682 nm^3
# of atom in unit cell:	2	4
Atomic radius:	Nb = 0.143 nm	Ag = 0.144 nm
$d_{(h,k,l)}$	$d_{(110)}$ = 0.2337 nm	$d_{(111)}$ = 0.2359 nm
Symmetry elements:	Four 3-fold rotation axes	Four 3-fold rotation axes
Melting point:	2469 °C	962 °C

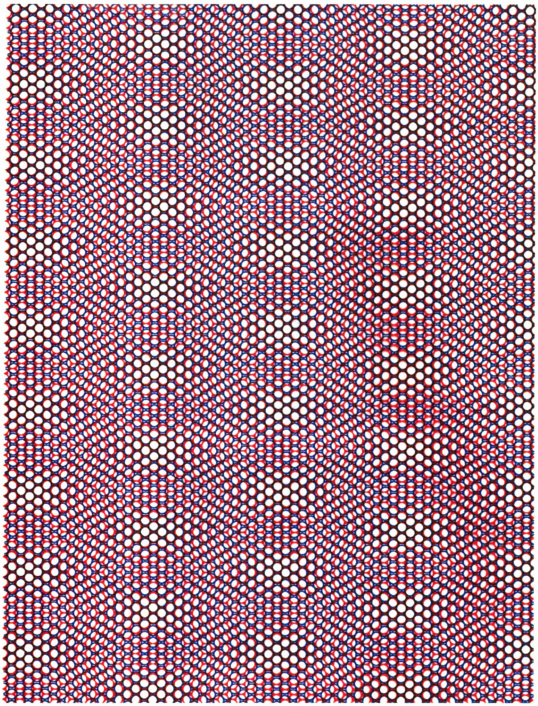

Figure 5.A.1. A superimposed atomic arrangement (unrelaxed) of fcc Ag (111) on bcc Nb (110) (with N-W relationship and 1.1% mismatch).

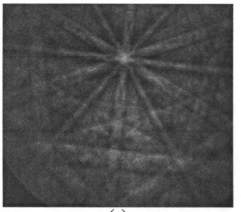

(a)

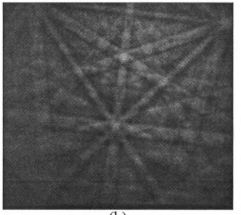

(b)

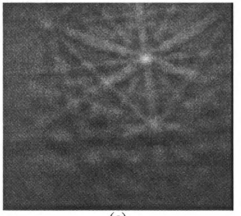

(c)

Figure 5.A.2 EBSP patterns of a 300 nm epitaxial Py film deposited on 200 nm epitaxial Nb at substrate temperature of: (a) & (b) 350°C and (c) 90°C. Patterns in part (a) & (b) are the EBSPs of twin areas.

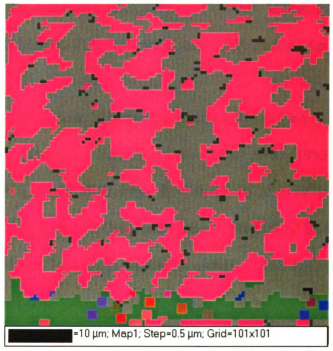

Figure 5.A.3. Orientation maps of 200 nm epitaxial Ag films grown on epitaxial Nb at substrate temperature of 350°C. The green areas are unsolved points (loss of EBSP signal).

5.5 REFRENCES:

1) M. Zheng, J. Shen, J. Barthel, P. Ohresser, Ch V Mohan, and J. Krischner, J. Phys.:Condens. Matter **12** 783 (2000).

2) K. Heinz, S. Müller, and L. Hammer, J. Phys.: Condens. Matter, **11**, 9437 (1999).

3) D J. Smith, A.R. Modak, T.A. Rabedeau, and S.S.P. Parkin, Appl. Phys. Lett., **71**. 1480 (1997).

4) G.R. Harp and S.S.P. Parkin, Thin Solid Films **288**, 315 (1996).

5) B. P. Tonner, Z.L. Han, and J. Zang, Phys. Rev. B, **47**, 9723 (1993).

6) M. T. kief and W. F. Egelhoff, Jr, Phys. Rev. B, **47**, 10785 (1993).

7) J. de la Figuera, J. E. Prieto, C. Ocal, and Miranda, Phys. Rev. B, **47**, 13043 (1993).

8) K. Bröhl, P. Bödeker, N. Metoki, A.Stierle, and H. Zabel, J. Crystal Growth, **127**, 682 (1993).

9) P. Bödeker, A. Abromeit, K. Bröhl, P. Sonntag, N. Metoki, and H. Zabel, Phys. Rev. B, **47**, 2353 (1993).

10) J. Camarero, L. Spendeler, G. Schmidt, K. Heinz, J. J. de Miguel, and R. Miranda, Phys. Rev. Lett. **83**, 2448 (1994).

11) J. Camarero, T. Graf, J. J. de Miguel, G. Miranda, W. Kuck, M. Zharnikov, A. Dittschar, C. M. Schneider, and J. Kirschner, Phys. Rev. Lett. **76**, 4428 (1996).

12) Ch. Rath, J. E. Prieto, S. Müller, R. Miranda, K. Heinz, Phys. Rev.B, **55**, 10791 (1997).

13) T. Lyman, Metals Handbook, The American Society for Metals, (1958)

14) L. Tang, D. E. Laughlin, and S. Gangopadhyay, J. Appl. Phys., **81**, 4906 (1997).

15) A. J. Wilkison, and D. J. Dingly, Acta metall. Mater. **40**, 3357 (1992).

CHAPTER 6

MAGNETO-TRANSPORT PROPERTIES OF EPITAXIAL MAGNETIC FILMS AND SPIN-VALVES

This chapter focuses on the magnetic and magneto-transport properties of epitaxial Py based spin-valves. The effect of spin-valve growth conditions on important device properties, including: (a) exchange bias field, (b) coercive field, and c) establishment of a well defined antiparallel state, have been investigated. To develop a better understanding of the magneto-transport properties of epitaxial Py based spin-valves, this chapter will first present an overview of magnetic properties of single Py films with and without an FeMn buffer layer. After this foundation is established, the magnetic characterization of single *epitaxial* Py films and the magneto-transport and magnetic characterization of epitaxial spin-valves are presented. In each of these sections, a brief introduction will be followed with the experimental procedures and results. This chapter concludes with a brief summary.

6.1 MAGNETIC PROPERTIES OF FEROMAGNETIC FILMS

Hysteresis Curves:

In ferromagnetic materials, the application of a sufficiently large external field in the direction opposite to the initial direction of magnetic domains will force the domains to reverse their direction. By continuously changing the external magnetic field from a large positive value to a large negative value and back to the original positive field, a

magnetic hysteresis loop will be created. Figure 6.1(a) depicts a typical ferromagnetic hysteresis loop. The coercive field, H_C, (points C and E) is the field at which the total magnetization M is zero. If the hysteresis loop is not symmetric about zero, H_C is usually defined as half the width of the hysteresis loop measured at M=0.

Pinning of the Ferromagnetic Layer:

If a ferromagnetic layer is placed next to an antiferromagnetic layer, the magnetization of the ferromagnetic layer can be "pinned" in a chosen direction by cooling the bilayer from above the Neel temperature of the antiferromagnet to room temperature in a sufficient large magnetic field. The pinning direction of the pinned ferromagnetic layer is referred to as the easy axis. The exchange anisotropy (known as 'unidirectional exchange-bias' [1]) due to pinning between the antiferromagnetic and ferromagnetic layers leads to a shift of the magnetization hysteresis loop along the magnetic field axis by H_E the exchange–bias field, and also usually increases the coercive field, H_C, in the hysteresis loop (see Figure 6.1(b-blue) [1-4]. After pinning, it is energetically favorable for the ferromagnetic layer to point in one particular direction, imposed by interfacial coupling with the adjacent antiferromagnetic layer. To overcome this energy, an external magnetic field, equal to H_E is required. Defining H_1 and H_2 as shown in Figure 6.1 (b), the exchange bias field, H_E, and the coercive field, H_C, of the pinned layers are given by:

$$H_E = \frac{H_1 + H_2}{2} \quad \text{and} \quad H_C = \frac{H_1 - H_2}{2}.$$

Berkowitz et al. [2] showed that the exchange-bias field is inversely proportional to the thickness of the pinned ferromagnetic layer: $H_E \propto \frac{1}{t_{FM}}$.

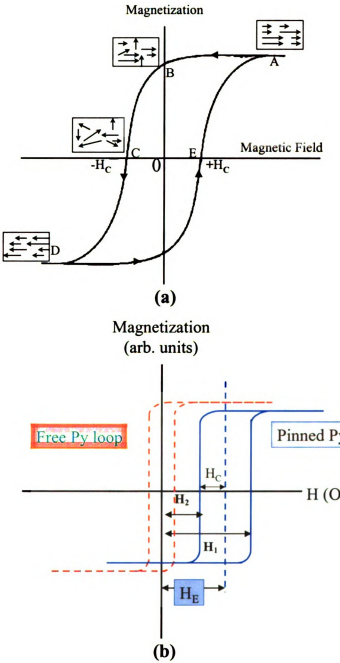

Figure 6.1. (a) A typical hysteresis loop of a ferromagnetic material (such as Fe, Co, Ni or their compounds). (b) Magnetization hysteresis loops for a free Py layer (red) and a Py-FeMn bilayer (blue) after pinning. The exchange-bias field (H_E) and the coercive field (H_C) of the pinned Py are indicated in the figure.

Several theoretical models predict that the exchange-biased field should increase if the antiferromagnetic layer contains small domains [5-9]. The random-field model by Malozemoff [8, 9] shows that small domains are typically produced by crystal disorder within the antiferromagnetic layer. This model also predicts that H_E increases with interfacial disorder, while a perfect crystalline antiferromagnetic layer and smooth interface with the ferromagnetic layer can reduce the exchange bias [9].

6.2 MAGNETIC PROPERTIES OF *EPITAXIAL* Py FILMS

6.2.1 Introduction

The crystallographic characterization of 200 nm thick epitaxial Py films sputter deposited on epitaxial Cu and FeMn films was discussed in chapter 5. These Py films were grown at 350°C or 90°C on 20 nm thick epitaxial Cu buffer layers or on 8 nm thick FeMn films In the present section, the magnetic properties of these Py layers are discussed.

From a magnetic point of view, Py is a soft ferromagnetic alloy because only a small external field is needed to rotate its magnetic moment. If a thin Py film is deposited on an antiferromagnetic material (such as FeMn), it can be pinned as described in section 6.1 (see section 6.1 and Figure 6.1(b- blue) [2-4].

6.2.2 Experimental Procedures

As described in chapter 2, an MPMS Quantum Design magnetometer was used to measure the magnetization of the epitaxial Py films deposited in this study to carry out

these measurements. A small portion (5 mm x 5mm) of a sample was cut and placed in the magnetometer, with the plane of the film parallel to the applied field.

Magnetic anisotropy in epitaxial Py films was studied by measuring the magnetization of these samples at zero and 90 degrees to the direction of the applied field. Note that the samples had to be taken out of magnetometer to be rotated 90 degrees around the axis perpendicular to the surface of the film.

The magnetization measurements were carried out at a temperature of 12 K. At this temperature the Nb buffer layer is not superconducting and does not affect the magnetization measurements. Details about the transport and magnetic properties of epitaxial Nb buffer layer are given in appendix 6.A

6.2.3 Results

6.2.3.1 Magnetic Properties of Epitaxial Py Films deposited on Epitaxial Cu Film.

The magnetization hysteresis loops of two sputter deposited epitaxial Py films (200 nm thick) grown at 350°C and 90°C as a function of magnetic field are shown in Figure 6.2(a). The coercive field of the epitaxial Py film grown at high temperature is small (approximately 12 Oe), while the H_C of the sample grown at ambient temperature (90°C) is much larger, about 50 Oe. This difference may suggest that the epitaxial Py film deposited at 90°C has lower crystalline quality and/or may have significant strain most likely due to structural defects. Recall that the electron backscattered patterns (EBSPs) of epitaxial Py films grown on epitaxial Cu films at 350°C were very sharp, while the EBSPs of samples grown at 90°C were distorted in a manner consistent with strain caused by misfit dislocations, threading defects, and point defects (see section 5.3.3).

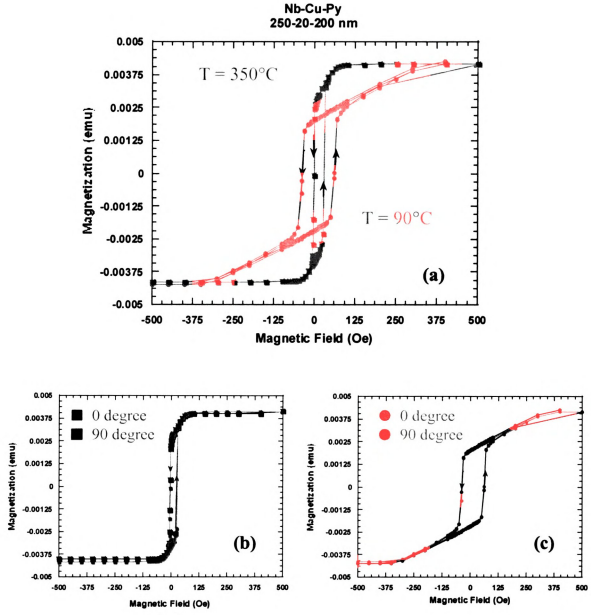

Figure 6.2 The magnetization hysteresis loops of 200 nm thick epitaxial Py films grown on 20 nm thick epitaxial Cu at substrate temperatures of 90°C (red) and 350°C (green). a) The coercivity (H_c = half width of magnetization loop) increases from 12 to 50 Oe for samples grown at low temperature (90°C). b & c) Comparison of the hysteresis loops of both samples when the samples are rotated 90 degrees with respect to the first orientation within the sample plane. The hysteresis loops overlapped for both samples, therefore there are no magnetocrystalline anisotropy in theses two epitaxial Py films.

Magnetic anisotropy:

The magnetic anisotropy (in particular, magnetocrystalline anisotropy) of these two epitaxial Py films was measured by comparing the magnetization of each film for two in-plane orientations. The difference in magnetic properties in different directions in magnetic materials is called magnetic anisotropy. Magnetocrystalline anisotropy is the tendency of the spins in the ferromagnetic materials to align in a particular direction imposed by the crystal lattice. Similarly, shape anisotropy is the tendency for these spins to align due to sample shape. In cubic magnetic materials, there should be no in-plane magnetocrystalline anisotropy in the (111) plane [10]. Therefore, the magnetic properties of a magnetic film with [111] growth direction should not be different if measured in the [110] and $[1\bar{1}2]$ directions. The results of such measurements are shown in Figure 6.2(b &c). The overlapping hysteresis loops for 200 nm thick epitaxial Py films grown at either 350°C or 90°C reveal no magnetocrystalline anisotropy for either epitaxial Py film.

6.2.3.2 Magnetic Properties of an Epitaxial Py Film deposited on an Epitaxial FeMn Film.

In Figure 5.12(c) of section 5.3.2, the effects of the epitaxial Cu and FeMn buffer layers on the crystallography of the epitaxial Py films were discussed. It was shown that the strain in the Py-FeMn bilayer is lower than that observed in the Py-Cu bilayer. Here it will be shown that the epitaxial Py film grown on a FeMn film also exhibited different magnetic behavior than that grown on a Cu film. Magnetization measurements were performed at 12 K on a 200 nm thick epitaxial Py film grown at a substrate temperature of 90°C on 8 nm thick FeMn. The magnetization hysteresis loops for this sample are

shown in Figure 6.3(a). The coercive field (H_C) was 7.5 Oe in one direction but decreased to 4 Oe when it was rotated 90 degrees. These low coercivity fields suggest that the ferromagnetic (Py) layer grown on an FeMn film contains less strain compared to the Py grown on Cu film (compare 4 Oe and 7.5 Oe for Py on FeMn to 50 Oe for Py on Cu) but also suggest the possibility of a magnetic anisotropy.

The data of Figure 6.3(a) have two distinguishing characteristics. (1) The hysteresis loop collected at zero degrees (green) is slightly shifted from zero field. (2) The magnetizations are the same in the two different directions, but the saturation and coercive fields are different. Generally, the presence of different saturation and coercive fields in hysteresis loops for different directions in the film is an indication of magnetic anisotropy. A shift in the hysteresis loop could also be caused by an exchange-bias field between the Py and FeMn layers (as described in section 6.1). However, as no external magnetic field was applied and the Py layer is relatively thick, H_E should be very small [2]. One possible source of this anisotropy is that the small fringe magnetic field of the sputtering gun magnets produced a weak exchange-bias interaction between the FeMn and Py layers, resulting in some degree of inadvertent pinning occurred during growth. To determine if this in fact occurred, this sample was taken through the usual pinning procedure (pinned along the zero direction), and the magnetization measurements were again performed. The resulting magnetization hysteresis loops are shown in Figure 6.3(b). The hysteresis loop collected at zero degrees again has a small shift, but the coercive fields (about 4 Oe) are now the same in both perpendicular directions. Considering the thickness of this Py film, this small shift suggests a very weak local exchange bias field between the epitaxial Py and its epitaxial FeMn buffer layer.

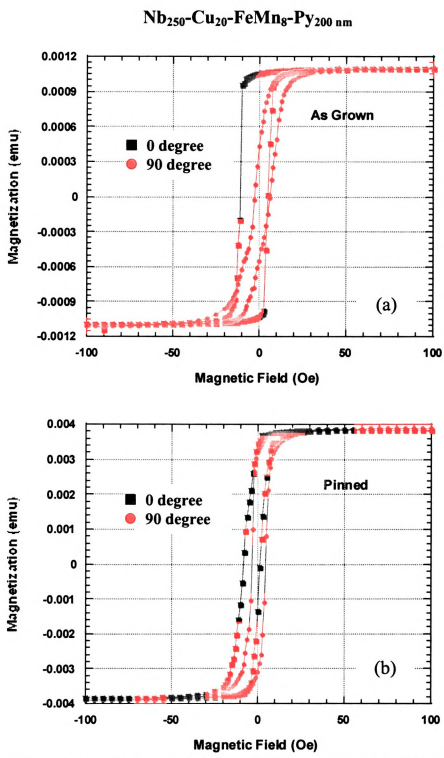

Figure 6.3 The magnetization hysteresis loops of a 200nm epitaxial Py film grown onto 8 nm epitaxial FeMn at room temperature a) As grown, b) Pinned. The green loops correspond to the applied field along a selected axis and the red loops are with the sample rotated 90 degrees with respect to the first within the sample plane. Note that zero degree in (b) is along the easy axis (pinning direction) and applied field.

Summary:

The results of the magnetic characterization of the epitaxial Py films reveal that:

1) The Py samples grown at an ambient temperature (90°C) on an epitaxial Cu buffer layer have much larger coercive fields than those grown at an elevated temperature (350°C). This is likely due to the presence of significant strains in the epitaxial Py films grown at low temperature.
2) The Epitaxial Py film deposited at 90°C on an FeMn buffer layer shows significantly smaller coercive field than a similar film grown at 90°C on Cu. This difference may be associated with lower strain in the epitaxial Py film, which is in agreement with the results obtained from crystallographic characterization.
3) There is no magnetic anisotropy in the epitaxial Py films grown on Cu buffer layer regardless of growth temperature. However, the magnetic anisotropy seen in the epitaxial Py film grown on FeMn buffer layer is due to existence of the exchange bias anisotropy.

6.3 MAGNETIC PROPERTIES OF EPITAXIAL Py BASED SPIN-VALVES

6.3.1 Introduction

In section 6.2, the magnetic properties of epitaxial Py films were studied. In this section the results of CPP-MR magneto-transport and magnetization measurements will be presented for the epitaxial Py-based exchange-biased spin-valve samples (EBSV).

One of the advantages of magnetic spin-valves over magnetic multilayers is that in spin-valves only a small field is needed to produce the GMR effect with a sharp switching response. There are two types of spin-valves, hybrid spin-valves (such as

Co/Cu/Py) and exchange-biased spin-valves (such as FeMn/Py/Cu/Py). A brief discussion of hybrid and exchange-biased spin-valves is given in Appendix 6.B. In this study, magnetic and magneto-transport properties of epitaxial Py-based exchange-biased spin-valves (EBSV) are discussed.

An EBSV consists of two ferromagnetic layers (such as Py, NiCoFe, or Co), separated by a non-magnetic layer (such as Cu, Ag), with one of the ferromagnetic layers directly exchange-coupled (pinned: see section 6.1) to an adjacent antiferromagnetic layer (such as FeMn, NiO, CoO). The pinning direction is referred to as the easy axis. The unpinned ferromagnetic layer separated by the non-magnetic layer is referred to as the free layer.

Parallel and Antiparallel States: Major and Minor Loops: In a typical CPP-MR measurement, the pinned spin-valve is mounted on a measuring device inside a magnet coil in such a way that the easy axis is in the direction of the negative field of the coil. By measuring the resistance of the spin valve as a function of magnetic field (changing the applied field from the initial negative field continuously, toward zero and then to the positive direction, and then reversing it back to the initial negative field) an exchange-biased hysteresis loop is obtained. There are two types of hysteresis loops: minor loops and major loops. The difference between major and minor hysteresis loops can be best described by referring to the schematic diagram of an ideal exchange-biased hysteresis loop, shown in Figure 6-4(a). This figure is divided into several regions, which are described below:

Regions 1 and 10: In the presence of a few hundred Oe of negative magnetic field (parallel to the biasing direction) the magnetic moments (spins) of both the pinned and

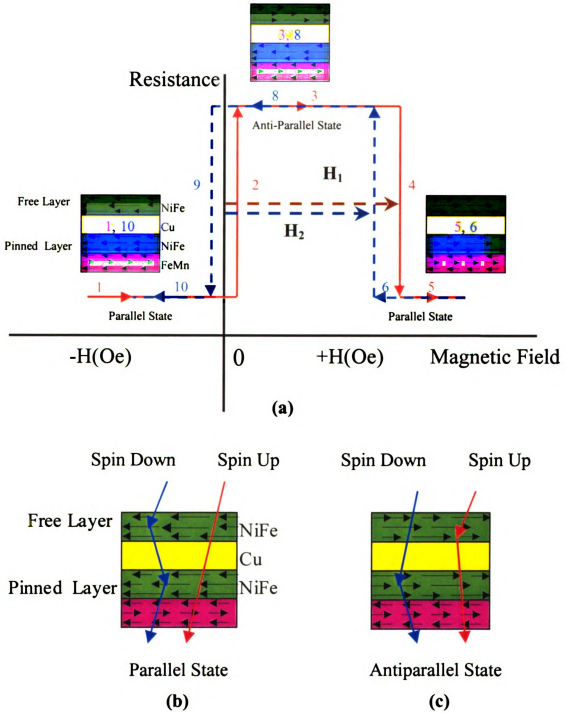

Figure 6.4 Schematic diagram of an exchange-biased hysteresis loop of an ideal spin-valve. (a) Illustration of the orientation of the spins in both the pinned and free ferromagnetic layers for both the parallel and antiparallel state. (b and c) illustrate the scattering of spin up and spin down electrons in both the free and pinned ferromagnetic layers.

free ferromagnetic layers line up parallel in the direction of the easy axis (biasing direction). This is a *parallel state.* Electrons in one of the two electron channels (spin up or spin down, see Figure 6.4(b)) experience relatively little scattering, thus the resistance of the sample is a minimum.

Regions 3 and 8: Upon changing the magnetic field continuously from the biasing direction, (first toward zero and then positive) the magnetic moments in the free ferromagnetic layer will switch from parallel to antiparallel with respect to the magnetic moments in the pinned ferromagnetic layer at a few Oe. Upon completion of the rotation of the moments in the free layer, the spin-valve will be in the *antiparallel state* and the resistance of the spin-valve should remain constant to form a plateau. This is now an intermediate scattering situation for electrons with either spin up or down (scattering in both channels, see figure 6.4(c)) and the resistance of the sample is a maximum. At this stage one can investigate either a minor loop or a major loop.

Minor loop: By changing the magnetic field from the middle of the antiparallel state plateau back to the original negative field, a *minor hysteresis loop* will result. A minor loop is a hysteresis loop produced purely by the rotation of the magnetic moments in the free ferromagnetic layer and is a way to magnetically evaluate that layer. In Figure 6.4(a), the path through points 1→2→3→8→9→10 represents a minor hysteresis loop.

Major loop, regions 5 and 6: Starting in region 3, further positive increases in the magnetic field will rotate the pinned ferromagnetic layer until the moments in that layer align themselves parallel to the moments in the free ferromagnetic layer. This process creates a second parallel state of opposite orientation to the first one. In this second parallel state, the spin-valve again has minimum resistance (see figure 6.4(b)). Cycling

through the steps 1→2→3→4→5→6→7→8→9→10 (Figure 6-4(a)) yields a GMR spin-valve hysteresis "major loop" [1-4, 10-13].

Exchange-biased field (H_E): As described in section 6.1, the exchange-bias field (H_E) is due to the effect of an antiferromagnetic layer on an adjacent ferromagnetic layer which leads to the magnetization or magnetoresistance hysteresis loop shifting away from the origin. To calculate H_E and the coercive field (H_C) of the pinned layer for an exchange-biased spin-valve, two field values need to be measured; H_1 and H_2, as shown on Figure 6.4(a).

The following sections discuss the experimental procedures and the results of magneto-transport (CPP-MR), magnetic (magnetization) measurements, and magnetic anisotropy of a few epitaxial spin-valves. These results will be discussed and compared to those obtained from polycrystalline spin-valves in this and another [14] study. Note that, structural characterization studies on some of these spin-valve samples (one each with thick and thin layers) have been done by H. Geng et al. [16]. The results of those studies confirm that the EBSV layers were epitaxed, but with some defects.

6.3.2 Experimental Procedures

Fabrication of Epitaxial Spin-Valves for CPP Measurement:

The epitaxial Py based spin-valves were sputter deposited in an L-shape (1 mm x 8 mm) pattern as was shown in Figure 2-7(b) (see also figure 6.5). The top surface of each sample was usually gold coated for oxidation protection. A series of six 75 μm square pillars were then fabricated on each sample using photolithographic techniques (see Figure 6.5(a)). This microfabrication technique involved optical lithography, ion-milling

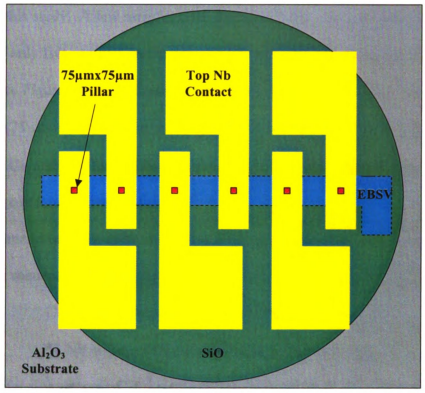

(a)

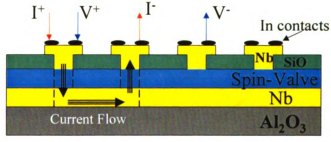

(b)

Figure 6.5 a) Sample geometry of the microfabricated exchange-biased spin-valve samples. b) A cross-sectional diagram showing the current flow and connections to the samples. The contact area between the top Nb, with I^+ and V^+ leads (current flow), and spin-valve is the area of the sample being measured [17].

or reactive ion etching (RIE), silicon monoxide evaporation, lift-off, and Nb sputtering.

Table 6.1 lists all of the exchange–biased Py based spin-valve samples sputter deposited in this study. A few samples were damaged during microfabrication; therefore, the results of only five samples are discussed. The CPP-MR of each pillar was measured separately (see Figure 6.5(b)) at liquid helium temperature (4.2 K). Note that the size of these pillars (75 μm x 75 μm) was much larger than the size of the twin variants seen in the epitaxial Cu and Py films identified using EBSP. Thus, each pillar is expected to contain a large number of twin variants.

All of the measured spin-valve samples (except one with a thinner pinned layer**) had the following sequence and thicknesses:

$$Nb_{250}\text{-}Cu_{20}\text{-}Py_{24}\text{-}Cu_{24}\text{-}Py_{24}\text{-}FeMn_{8}\text{-}Au_{15}\text{-}Nb_{250\ nm}$$

$$**\ Nb_{250}\text{-}Cu_{20}\text{-}Py_{24}\text{-}Cu_{24}\text{-}Py_{6}\text{-}FeMn_{8}\text{-}Au_{15}\text{-}Nb_{250\ nm}$$

The Nb film was deposited at a substrate temperature of 750°C and post deposition annealed at 950°C. The first Cu layer (20 nm thick) was then deposited at 150°C, and post deposition annealed at 350°C. The remaining layers were deposited at ambient temperature (90°C). The standard deposition rates for Nb, Cu, Py, and FeMn were 3, 3.4, 3.3, and 2.1 Å/s, respectively. For the first few samples, the Al_2O_3 substrates were cleaned in the sputtering room in an ultrasonic bath using acetone, then alcohol. Failure to achieve a good antiparallel state led to preparing the remaining samples in a clean room. In this new sample preparation technique, the substrate cleaning was changed to the following. The substrates were first cleaned in a combination of boiling deionized (DI) water and detergent (Alconox) in an ultrasonic bath. After rinsing in boiling deionized water, the substrates were rinsed and mechanically cleaned in acetone using

Table 6.1

Symmetrical EBSV Samples Prepared Using Photolithography

Sample	Type of Spin-valves	Growth Temperature
27-01 *Damaged*	Nb-Cu-[Py-Cu-Py-FeMn]-Au-Nb 250-20-[24-20-24- 8]-15-250 nm	750-(150 /350)-[100°C]. HTH-LTH-[No Heater]
27-02 *Damaged*	Nb-Cu-Py-[Cu-Py-FeMn]-Au-Nb 250-20-24-[20-24- 8]-15-250 nm	750-(150/350)-350-[100°C] HTH-LTH-[No Heater]
33-01	Nb-Cu-[Py-Cu-Py-FeMn]-Au-Nb 250-20-[24-25-24- 8]-15-250 nm	750-(150/350)-[80°C]. HTH-LTH-[No Heater]
33-02 *Damaged*	Nb-Cu-Py-[Cu-Py-FeMn]-Au-Nb 250-20-24-[25-24- 8]-15-250 nm	750-(150/350)-350-[90°C] HTH-LTH-[No Heater]
33-03 not included in this study	Nb-Cu-[Py-Cu-Py-FeMn]-Au-Nb 250-20-[12-20-12- 8]-15-250 nm	750-(150/350)-[90°C] HTH-LTH-[No Heater]
33-04 *Damaged*	Nb-Cu-[FeMn-Py-Cu-Py]-Au-Nb 250-20-[8 -12-20 -12]-15-250 nm	750-(150/350)-350-[80°C] HTH-LTH-[No Heater]
37-01 *	Nb-Cu-[Py-Cu-Py-FeMn]-Au-Nb 250-20-[24-25-24- 8]-15-250 nm	750-(150/350)-[90°C]. HTH-LTH-[No Heater]
37-02 *	Nb-Cu-[Py-Cu-Py-FeMn]-Au-Nb 250-20-[24-25-24- 8]-15-250 nm	750-(150/350)-[90°C] HTH-LTH-[No Heater]
37-03 *	Nb-Cu-[Py-Cu-Py-FeMn]-Au-Nb 250-20-[24-25-24- 8]-15-250 nm	750-(150/350)-[90°C]. HTH-LTH-[No Heater]
40-04 *	Nb-Cu-[Py-Cu-Py-FeMn]-Au-Nb 250-20-[24-25-6- 8]-15-250 nm	750-(150/350)-[90°C]. HTH-LTH-[No Heater]

Samples 27-01, 27-02, 33-02, and 33-04 were either damaged during lithographic fabrication or preparation.

*Deposition rates of Cu in sample 37-1, 37-2, and (37-3 & 40-4) are 9.8, 1.2, and 3.4Å/s, respectively.

cotton swabs, then rinsed in an isopropyl alcohol. The substrates were then washed with DI water and dried with flowing industrial grade nitrogen gas. The cleaned samples were transported to the sputtering room in closed containers.

Magnetization Measurements (Magnetic Anisotropy and Strain):

Similar to the magnetization measurement of epitaxial Py films, a small portion of an epitaxial sample was cut and placed in the magnetometer with the plane of the film parallel to the applied field. Note that the easy axis of the spin-valve must be parallel to the direction of applied field. To look for any magnetic anisotropy in the spin-valves, the sample was removed from the SQUID magnetometer and pinned at different angles (90-degree intervals), and the magnetization (minor loop) was measured again.

6.3.3 CPP-MR and Magnetization Measurements on Py-Based EBSV.

In this section the results of CPP-MR magneto-transport and magnetization measurements will be presented for the epitaxial Py-based exchange-biased spin-valve samples (EBSV), mostly from Nb_{250}-Cu_{20}-Py_{24}-Cu_{24}-Py_{24}-$FeMn_{8}$-Au_{15}-Nb_{250nm}. Here the FeMn is used to pin the magnetization of the adjacent Py layer. As described previously (see 6.3.1) such an EBSV should allow reliable production of both parallel and antiparallel magnetic states. The CPP-MR results will be compared with previous results for polycrystalline samples with 1 mm^2 area and examined as a function of deposition rate.

Samples with substrates cleaned in the sputtering room.

The substrates for the first set of EBSVs of the specified form were prepared in the sputtering room without an extensive cleaning (see section 6.3.2). The CPP-MR ($A\Delta R$) data from one of these samples is shown in Figure 6.6, where $A\Delta R(H)$ is defined as:

$$A\Delta R(H) = AR(H) - AR(P).$$

Where A is the area of the pillar, R(H) is the resistance of sample at a particular magnetic field, and R(P) is the resistance of sample at the parallel state.

These data have two disturbing characteristics. (1) As the field is swept to positive values, the data initially rise sharply as expected, but the data fall quickly back to the value of the parallel state, instead of forming a plateau when an antiparallel state is established. (2) $A\Delta R$ (1.3 $f\Omega m^2$) is only about half as large as the range of values (~2.7 $f\Omega m^2$) previously found for polycrystalline EBSVs of the same composition with area ~ $1mm^2$ [14]. Taken together, these behaviors strongly suggest that the sample has not reached a true antiparallel state.

Two phenomena might be responsible for failure to reach an antiparallel state.

a) Undesired ferromagnetic coupling between the pinned and free Py layers. Such coupling could occur, for example, due to the presence of pinholes in the Cu layer induced by either growth defects or the presence of residual dirt particles on the substrate surface before deposition.

b) Lack of good exchange-bias coupling between the pinned ferromagnetic layer and the FeMn.

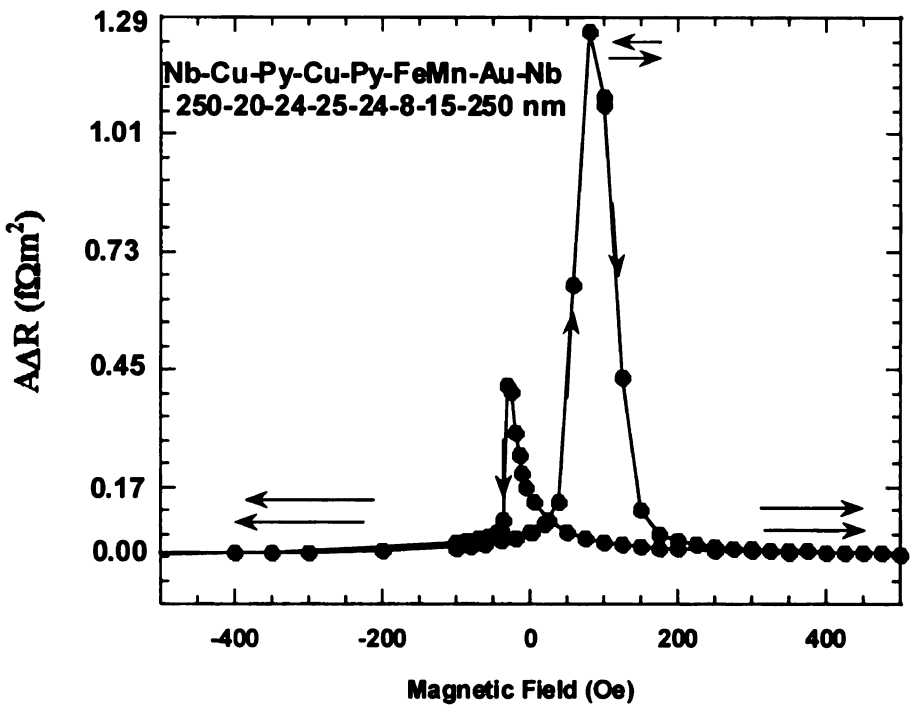

Figure 6.6 CPP Magnetoresistance hysteresis loop of a symmetrical Py based EBSV. The standard deposition rates for Nb, Cu, Py, and FeMn were 3, 3.4, 3.3, and 2.1 Å/s, respectively. In this sample, an anti-parallel state is not observed, suggesting that there is magnetic coupling between the free Py and pinned Py layers resulting in both of layers switching at the same time. The coupling between Py layers is probably caused by growth of pinholes due to a dirty substrate.

To attempt to distinguish between these two possibilities, two steps were taken. First a new procedure for substrate cleaning was devised, involving a more rigorous cleaning process and carrying out this process inside a clean room. Details were given in section 6.3.2. Second, to see if the lack of antiparallel state might be related to growth rate, a set of samples was prepared with different deposition rates.

Sample prepared with substrate cleaned in a clean room.

Using these cleaned substrates, a new set of epitaxial symmetrical EBSVs were grown. One of the samples (with standard Cu sputtering rate 3.4 Å/s) had the same sequence, deposition rates, and thicknesses as the previous sets. The result of CPP-MR measurement of this sample is illustrated in Figure 6.7. The first feature of the new data to note is that the falloffs from the nominal antiparallel states are much slower than in Figure 6.6. The second feature is that values of $A\Delta R$ for this sample: 2.6 $f\Omega m^2$, comparable to the values ~2.3 $f\Omega m^2$ previously found for polycrystalline samples with A ~ 1 mm^2 [15]. Together, these slower falloffs and agreement in $A\Delta R$s suggest that the problem of coupling between the free and pinned Py layers has been eliminated, and that its main source was inadequate cleaning of the substrates.

To investigate the effect of the deposition rates on the antiparallel state, three EBSV sample were deposited (including the previous sample). Figure 6.8 shows $A\Delta R$ for these three EBSV samples for which the substrates were also cleaned in a clean room. All three were prepared in a single run, but with different sputter deposition rates for Cu: 1.2 Å/s, 3.4 Å/s, and 9.8 Å/s. The deposition rates for the Nb, FeMn, and Py were kept the same as before. The values of $A\Delta R$ for all three samples: 2.8 $f\Omega m^2$ for Cu sputtering rate

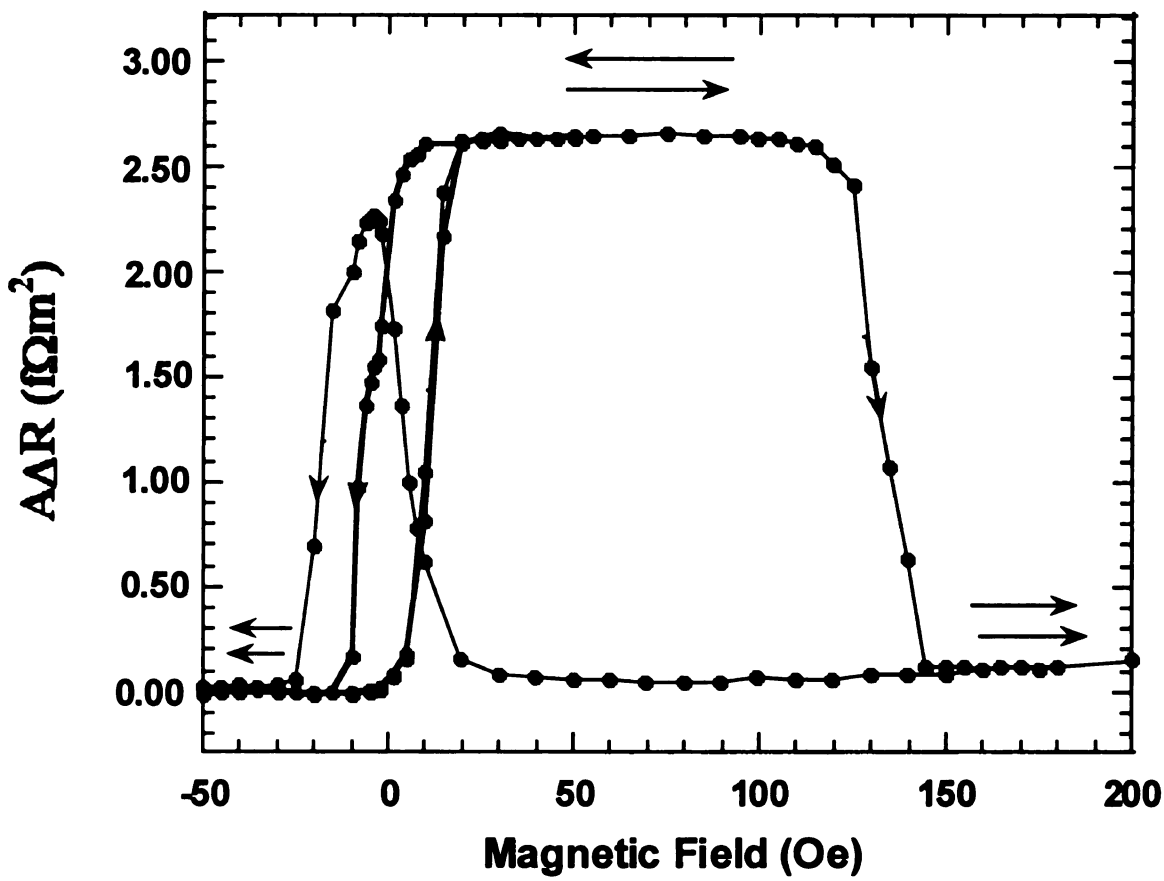

Figure 6.7 CPP-MR hysteresis loops of an epitaxial symmetrical EBSV: Nb_{250}-Cu_{20}-Py_{24}-Cu_{24}-Py_{24}-$FeMn_8$-Au_{15}-$Nb_{250\,nm}$ epitaxial spin-valves. Both major and minor (red) loops are shown. AΔR is about 2.6 fΩm^2.

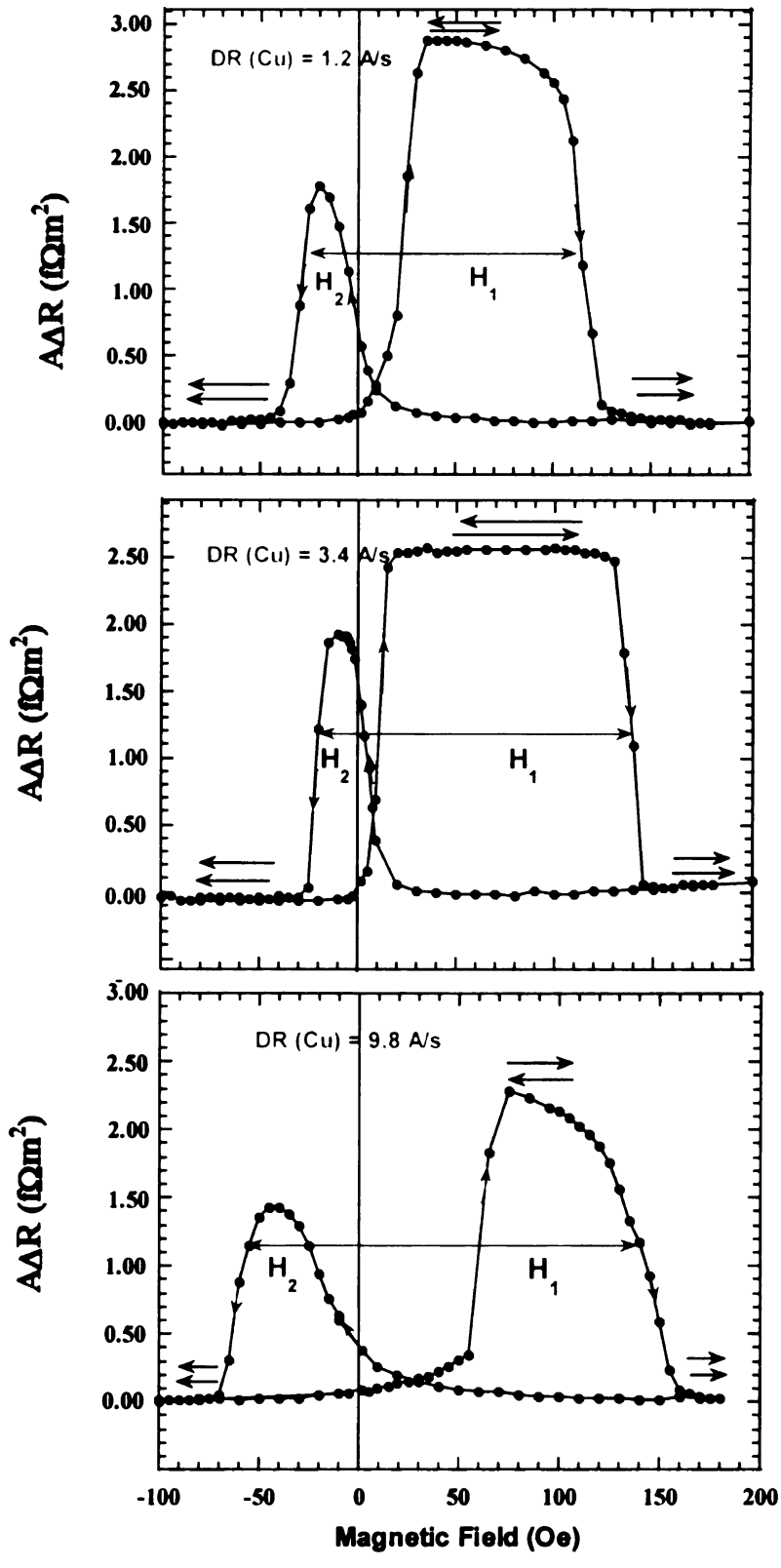

Figure 6.8 CPP-MR hysteresis loops of three epitaxial Py spin-valves: Nb_{250}-Cu_{20}-Py_{24}-Cu_{24}-Py_{24}-$FeMn_8$-Au_{15}-$Nb_{250\ nm}$. AΔR are 2.8, 2.6, and 2.3 fΩm^2 for sample deposited with Cu deposition rates of 1.2, 3.4, and 9.8 Å/s, respectively. All layers were deposited at 90°C except for the first Nb and Cu layers.

1.2 Å/s; 2.6 fΩm^2 for rate 3.4 Å/s; and 2.3 fΩm^2 for rate 9.8 Å/s, are similar to each other and also comparable to the values ~2.3 fΩm^2 for polycrystalline samples with A ~ 1 mm^2. Now looking at the difference between the CPP-MR behavior of these three samples in Figure 6.8, the 'standard' sputtering rate of 3.4 Å/s gives the best defined and flattest antiparallel 'plateau'. The free layer rotates in smallest field, about 15 Oe for rate = 3.4 Å/s, versus about 25 Oe for rate = 1.2 Å/s and about 70 Oe for rate = 9.8 Å/s. Also, the antiparallel state persists to higher field, about 130 Oe for rate = 3.4 Å/s, versus about 100 Oe for rate = 1.2 Å/s and only about 70 Oe for rate = 9.8 Å/s.

Defining H_1 and H_2 at the 'half-heights' of AΔR as shown in Figure 6.8, and following the standard procedure shown in section 6.1 to define the exchange bias field, H_E, and the coercive field, H_C, gives values that are listed in Table 6.2.

Table 6.2

Deposition rate (Å/s)	**1.2**	**3.4**	**9.8**
AΔR (f Ω m^2)	2.8	2.6	2.3
AP state persist fields (Oe)	100	130	70
Exchange-bias field (H_E, Oe)	51	73	60
Pinned layer coercive field (H_C, Oe)	61	67	80

Sample ion-milled with better 'cooling procedure', including search for magnetic anisotropy in the free Py layers.

The possibility that heating of the sample during the ion-milling process could affect the coercive field for the free layer, led to preparing and ion-milling of one set of samples using a procedure that was expected to keep the sample cooler during the ion-milling.

This procedure involved using a thin layer of high thermal-conductive silver grease between the back of the substrate and the Cu heat sink. The silver grease is UHV compatible and originally was provide for mounting the regular magnetron sputtering (Mini-Mac sputtering gun) target on the target holder for better electrical and thermal conductions.

Since the exchange-bias field decreases with increasing thickness of the 'pinned' layer [2], to achieve enhanced pinning the thickness of the pinned layer was reduced to 6 nm, giving an EBSV of the form (Nb_{250}-Cu_{20}-Py_{24}-Cu_{24}-Py_6-$FeMn_8$-Au_{15}-$Nb_{250\,nm}$).

Figure 6.9 shows the CPP-MR data from one such sample. This curve shows $A\Delta R$ = 1.4 $f\Omega m^2$ comparable to the value ~ 1.3 $f\Omega m^2$ previously found from a $1mm^2$ polycrystalline EBSV with the same layer thickness [15]. To look for the possibility of magnetic anisotropy in the EBSV, this samples was pinned in three different directions (0° ($[1\bar{1}0]$), 45°, and 90° ($[11\bar{2}]$)) and $A\Delta R$ was measured. The results of these measurements are shown in Figure 6.10. The coercive field of the minor loop is about 40 Oe when the sample is pinned along the $[1\bar{1}0]$ and the 45° directions. While the coercive field is about 46 Oe when the sample is pinned along the $[11\bar{2}]$, slightly larger than coercive field along $[1\bar{1}0]$ direction. This may be due to sample geometry. To determine if this was in fact a shape effect, the magnetization of a small 1 mm x 1mm section of this sample was measured in the $[1\bar{1}0]$ and $[11\bar{2}]$ directions (pinned before each measurement in the $[1\bar{1}0]$ and $[11\bar{2}]$ directions, respectively). The magnetization hysteresis loops, as shown in Figure 6.11, are essentially identical (note overlap) showing that there is no evidence of magnetic anisotropy in this sample.

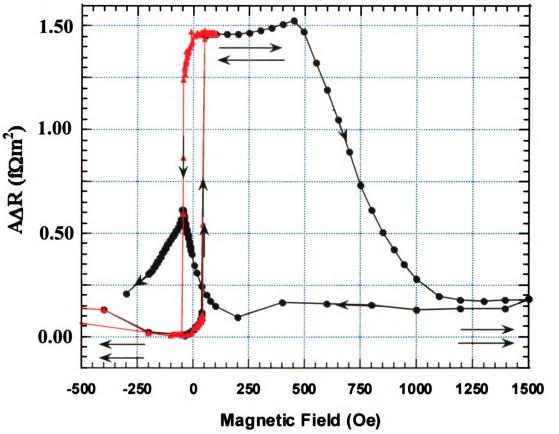

Figure 6.9 CPP-MR hysteresis loop of an epitaxial Py based EBSV: Nb_{250}-Cu_{20}-Py_{24}-Cu_{24}-Py_{6}-$FeMn_{8}$-Au_{15}-Nb_{250nm}. AΔR is about 1.4 fΩm^2.

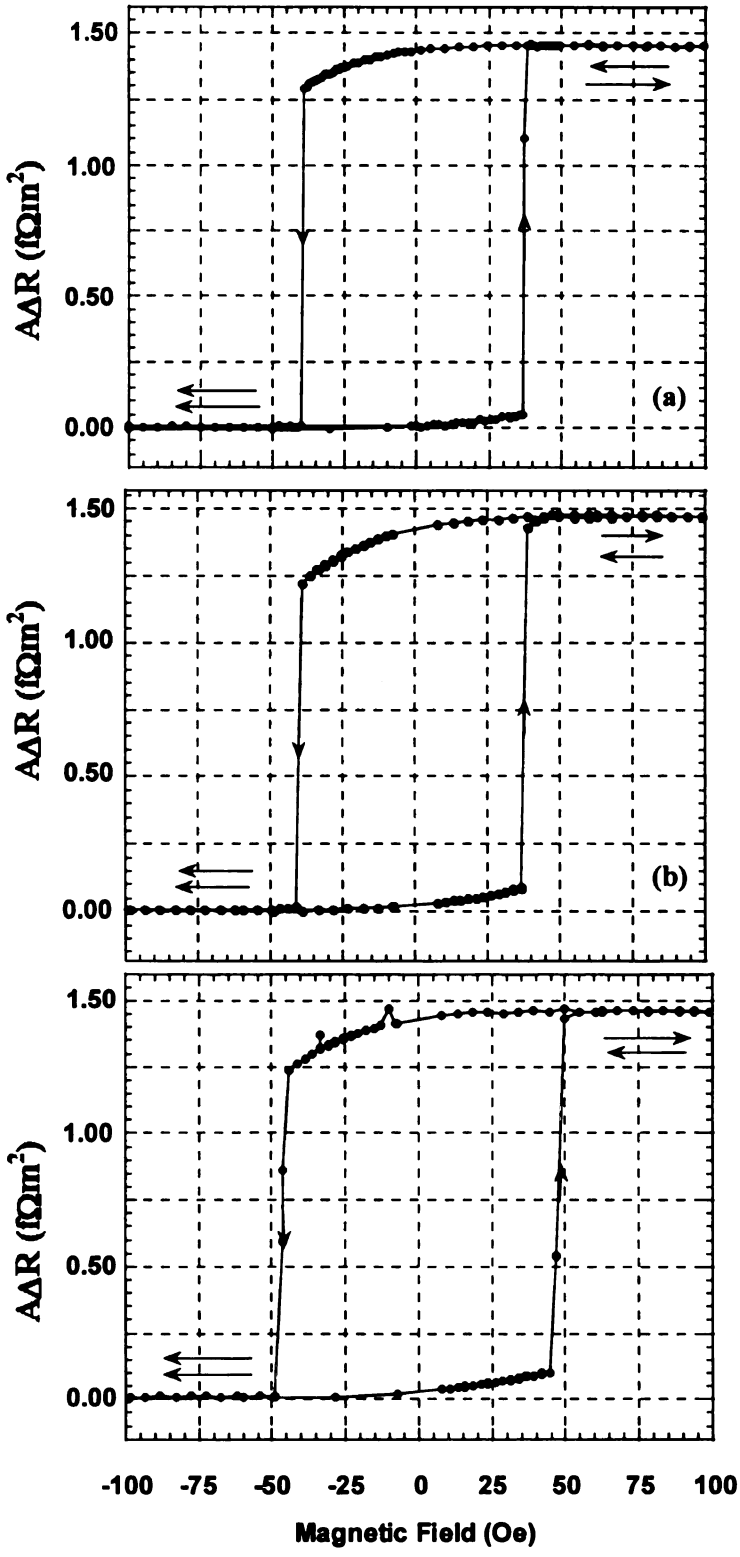

Figure 6.10 Minor hysteresis loops of an epitaxial EBSV ($Py_{(24)}$-$Cu_{(24)}$-$Py_{(6)}$-$FeMn_{(8nm)}$). The epitaxial EBSV sample was pinned at a) 0°, b) 45°, and 90°. Zero and 90°, corresponds to the [110] and [112] directions in the Py(111) plane. The similarity of coercive fields suggests that there is no magnetic anisotropy (except some shape effect) in this epitaxial EBSV.

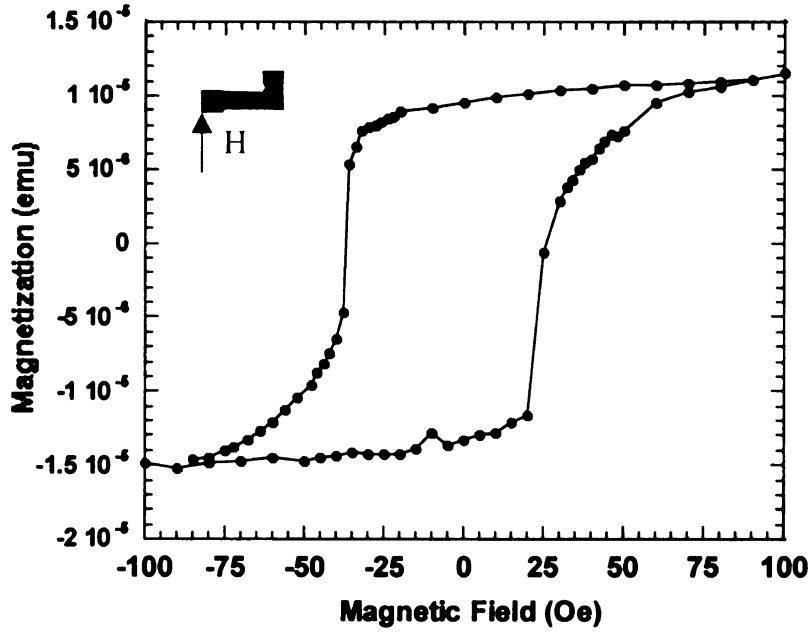

(a)

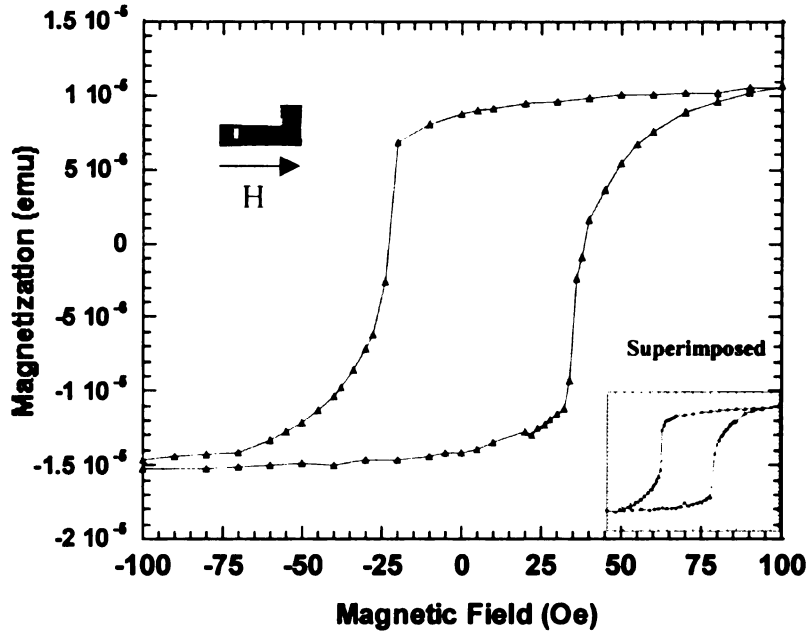

(b)

Figure 6.11 Magnetization hysteresis loops of a small section (blue) of the epitaxial EBSV (Cu_{20}-Py_{24}-Cu_{24}-Py_6-$FeMn_8$-Cu_{20nm}) pinned at a) 0° and b) 90° angles. The coercive field (30 Oe) and saturation fields are equal in both directions.

Summary: A set of Py based exchanged-biased spin-valve samples was prepared using improved substrate cleaning and improved sample cooling during the ion-milling. The data from these samples featured a sharp switch from the parallel to the antiparallel states with a well defined and flat antiparallel state plateau. The values of AΔR were also comparable to similar polycrystalline EBSVs.

6.3.3.3 Comparison of Polycrystalline and Epitaxial Samples:

The behavior of the epitaxial EBSV sample with a layering sequence of (Nb_{250}-Cu_{20}-Py_{24}-Cu_{24}-Py_{24}-$FeMn_8$-Au_{15}-Nb_{250nm}) (also see figure 6.7) was compared to two polycrystalline samples with identical layering sequences. One of the polycrystalline samples was sputter deposited at a substrate temperature of 90°C in the millimeter-sized CPP geometry (see Figure 1.5). The second polycrystalline sample was sputter deposited at a substrate temperature of -30°C in an L shape pattern and then photolithographicly fabricated, with a pillar area of 75 μm x 75 μm [14]. The CPP-MR results of both samples, along with the epitaxial sample, are shown in Figure 6.12. The values of AΔR, H_E, and H_C are tabulated in Table 6.3.

Table 6.3

	AΔR $f\Omega\,m^2$	H_E Oe	H_C Oe
Polycrystalline, 75 μm x 75 μm, T_{growth} = -30°C	2.4	175	55
Polycrystalline, 1mm^2 T_{growth} = 90°C	2.5	40	40
Epitaxial 75 μm x 75 μm T_{growth} = 90°C	2.6	73	67

While the values of AΔR for all three samples are similar, the coercive field, H_C, in the pinned Py layer of the polycrystalline sample deposited at -30°C is about three times smaller than that in the exchange–bias field in that sample. This polycrystalline sample displays a broad antiparallel state plateau for positive magnetic fields and returns just before the field come to zero (Figure 6.12(a)). In contrast, the values of H_C in both polycrystalline and epitaxial samples deposited at 90°C are very close to H_E. These two samples have well defined antiparallel state plateaus, but did not display return antiparallel state plateaus. This indicates that a growth temperature higher than 30°C may affect the quality of the FeMn and Py layers and thereby weaken the exchange-bias coupling between these two layers. As a result, the antiparallel state will not form during the return part of major hysteresis loops.

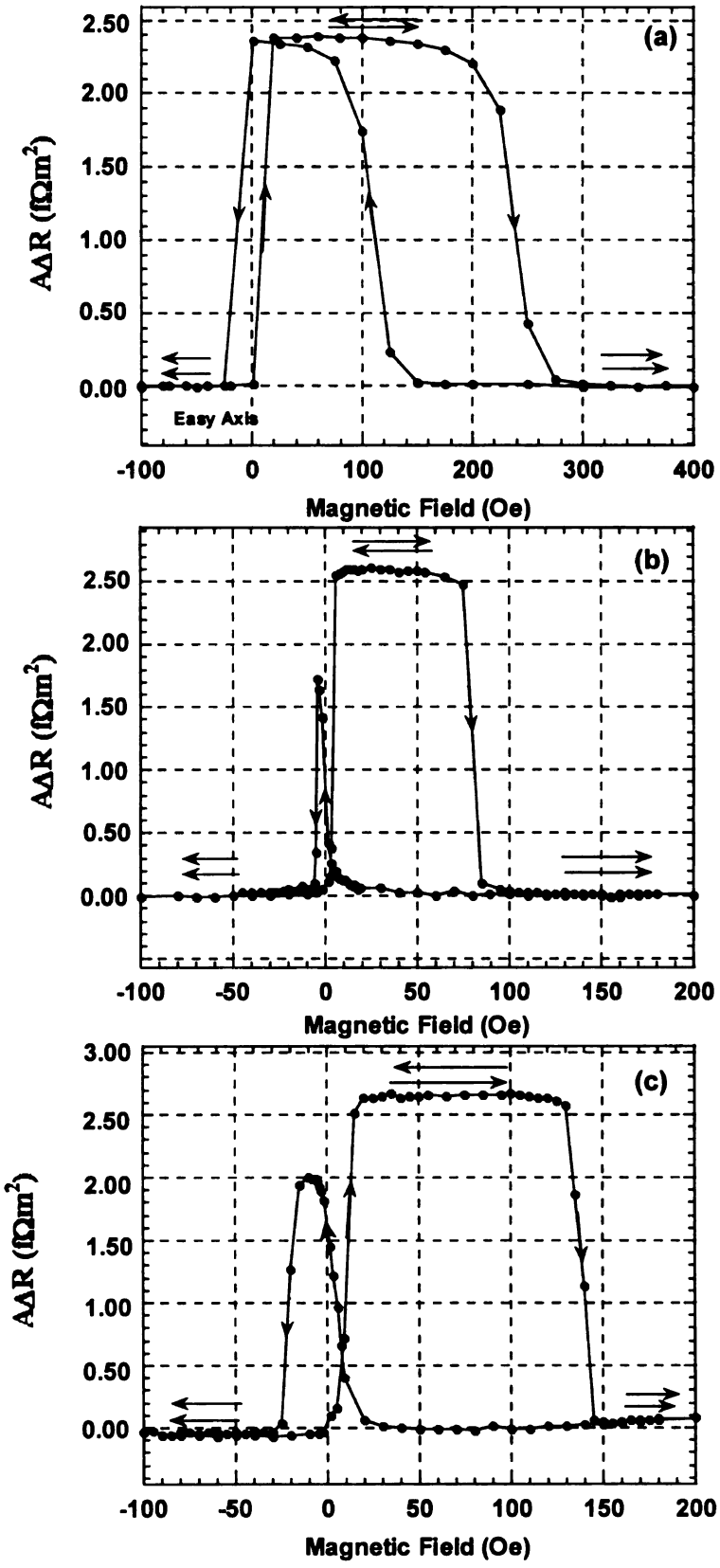

CCP-MR of a 75 x 75 μm^2 pillar of a polycrystalline EBSV.
T_{Growth} = -30°C
$A\Delta R = 2.4\ f\Omega m^2$

CCP-MR of a millimeter size polycrystalline EBSV.
T_{Growth} = 90°C
$A\Delta R = 2.5\ f\Omega m^2$

CCP-MR of a 75 x 75 μm^2 pillar of an epitaxial EBSV.
T_{Growth} = 90°C
$A\Delta R = 2.6\ f\Omega m^2$

Figure 6.12 The CPP-MR hysteresis loops of two polycrystalline Py spin-valves: Nb_{250}-Cu_{20}-$FeMn_8$-Py_{24}-Cu_{24}-Py_{24}- Au_{15}-$Nb_{250\ nm}$ and one epitaxial Nb_{250}-Cu_{20}-Py_{24}-Cu_{24}-Py_{24}-$FeMn_8$-Au_{15}-$Nb_{250\ nm}$.

6.4 SUMMARY

The important issues in studying the magneto-transport properties of epitaxial single magnetic films and spin-valves are growth temperature, deposition rates, type of buffer layer, and surface quality of the substrates. It has been shown that the coercive field in epitaxial single Py films grown at 90°C is much larger than that observed in films grown at 350°C, most likely as a result of a large number of dislocations and defects which create strain in the deposited films. Depositing on a different buffer layer might reduce the number of these dislocations and therefore dissipate some of the strain. The surface quality of the substrates is also an important factor, especially for magneto-transport performance of epitaxial EBSV. The presence of residual dirt particles on the substrate surface was suspected to create pinholes in the Cu layer which resulted in an undesired coupling between the two ferromagnetic (Py) layers. Changes in the substrate cleaning procedures eliminated the problem of coupling between Py layers. In the CPP-MR hysteresis loops from epitaxial EBSV samples prepared with substrates cleaned in a clean room, showed sharp switching from the parallel to antiparallel states, with a long range and flat antiparallel state plateau. In studying the effect of deposition rate, an intermediate Cu deposition rate of 3.4 Å/s gave the best defined and flattest antiparallel plateau. $A\Delta R$ values of epitaxial EBVS samples were comparable to those for similar polycrystalline EBSVs. The deposition temperature was also an important factor in the fabrication of epitaxial spin-valves in particular its effect on the exchange-bias coupling between the pinned Py and the adjacent FeMn layers. Magnetization data of these EBSV showed no evidence of magnetic anisotropy in the free layer of the EBSVs.

Appendix 6.A

Transport Properties of Epitaxial Nb Films

Nb is one of the many metals that become superconducting at low temperature. Bulk, high purity Nb has a resistivity of about 13 μΩ-cm at room temperature, with a superconducting critical transition temperature (T_c) of 9.2 K. However, depending on the growth condition, Nb films can have different resistivity and T_c values than bulk. A polycrystalline sputter deposited Nb film (~300 nm thick) has resistivity of about 15-18 μΩ-cm at room temperature and about 6 μΩ-cm at 10 K, with T_c = 8.9 K, using both van der Paaw and four probe measurements. Single crystal epitaxial Nb films are expected to have better transport properties than polycrystalline films (less dislocations and point defects). The epitaxial Nb films grown by sputter deposition had a residual resistivity of about 15-17 μΩ-cm at room temperature and approximately 0.6-1.01 μΩ-cm at 10 K, using van der Paaw measurements and approximately 0.75-1.56 μΩ-cm using four probe measurements. The superconducting transition temperature of these epitaxial Nb films was approximately $T_c \cong 9.1$ K, as shown in Figure 6.A.1(a).

Magnetic Property of Nb:

From a magnetic point of view, Nb is a strong diamagnet below its transition temperature and a very weak paramagnet above its transition temperature. Therefore, measurement of the magnetization as a function of temperatures can also determine the transition temperature of the Nb film. Figure 6.A.1(b), shows magnetization of the same epitaxial Nb film as in Figure 6.A.1(a).

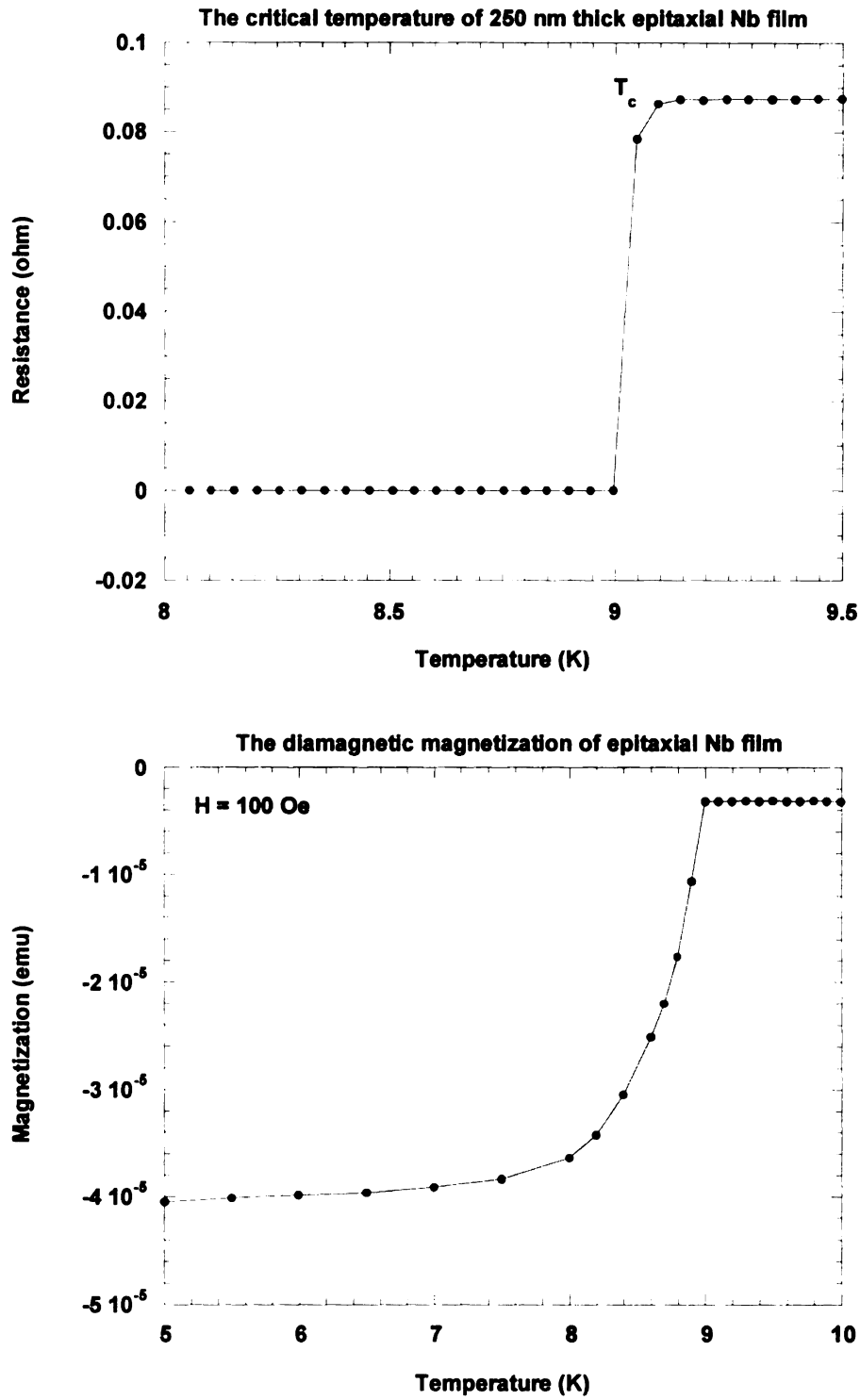

Figure 6.A.1. The resistance and magnetization of a 250 nm thick epitaxial Nb film as a function of temperatures. The T_C of this film is about 9.1 K.

APPENDIX 6.B

TYPES OF SPIN-VALVES

There are several types of spin-valve structures. Among them, hybrid spin-valves (such as Co/Cu/Py) and exchange-biased spin-valves (such as FeMn/Py/Cu/Py) are the most important ones.

Hybrid spin-valves: The idea behind the hybrid spin-valve is to be able to independently rotate the direction of the magnetization of both ferromagnetic layers. This independent control of the ferromagnetic layer could be achieved by using either the same type of ferromagnetic material, with one of the ferromagnetic layers is much thicker than the other, or by using a different ferromagnetic material for the second magnetic layer.

Examples: Py_{12} - Cu_{20} – $Py_{24\ nm}$ and Py_{12} – Cu_{20} – $Co_{6\ nm}$.

Exchange-biased spin-valves (EBSV): In the EBSV structure, both ferromagnetic layers could either be the same or different materials, or have different thicknesses. However, one of the two ferromagnetic layers must be pinned to an anti-ferromagnetic layer. The pinning is due an interfacial interaction between antiferromagnetic and ferromagnetic layers that leads to anisotropy, a unidirectional anisotropy or 'exchange-bias' [1]. The pinning direction is along the applied field and is referred to as the easy axis. The second ferromagnetic layer is known as the free layer. If the thicknesses of both magnetic layers are identical, the EBSV structure is referred to as symmetrical EBSV.

Example: $FeMn_8$ – Py_{24} – pinned layer) – Cu_{24} – $Py_{24\ nm}$– free layer) and

$FeMn_8$– Co_6– Cu_{20}– Py_{24} (nm).

6.4 REFERENCES.

1) R. Jungblut, R. Coehoorn, M.T. Johnson, Ch. Sauer, P.J. van der Zaag, A. R. Ball, Th. Rijks, J. aan de Stegge, and A. Reinders, J. Magn. Magn. Mater. **148**, 300 (1995).

2) E. Berkowitz and K. Takano, J. Magn. Magn. Mater. **200**, 552 (1999).

3) J. Nogués and Ivan K. Schuller, J. Magn. Magn. Mater. **192**, 203 (1999).M. F.

4) Gillies, J. N. Chapman, and J. C. Kools, J. Appl. Phys. **78**, 5554 (1995).

5) W. H. Meiklejohn and C. P. Bean, Phys. Rev. **105** 904 (1957).

6) B. D. Cullity, Introduction to magnetic Materials (Addison-Wesley Publishing Company, Reading, MA, 1972).

7) D. Mauri, H. C. Siegmann, P. S. Bagus, and E. Kay, J. Appl. Phys. **62**, 3047 (1987).

8) P. Malozemoff, Phys. Rev. B **35**, 3679 (1987).

9) P. Malozemoff, Phys. Rev. B **37**, 7673 (1988).

10) D. Sander, A. Enders, and J. Kirschner, J. Magn. Magn. Mater. **200**, 439 (1999).

11) C. Tsang, N. Heiman, and K. lee, J. Appl. Phys. **52**, 2471 (1981).

12) W. P. Pratt Jr., S. D. Steenwyk, S.Y. Hsu, W. C. Chiang, A. C. Schaefer, R. Loloee, and J. Bass, IEEE Trans. Magn. **33**, 3505 (1997).

13) S. D. Steenwyk, S. Y. Hsu, R. Loloee, J. Bass, and W. P. Pratt Jr., J. Appl. Phys. **81** 4011 (1997).

14) R.D. Slater, J.A. Caballero, R. Loloee, and W.P. Pratt, Jr. to be published in J. Appl. Phys (2001).

15) L. Vila, W. Park, J.A. Caballero, D. Bozec, R. Loloee, W.P. Pratt, Jr., and J. Bass, J. Appl. Phys. **87** 8610 (2000).

16) H. Geng, R. Loloee, J.W. Heckman, J. Bass, W.P. Pratt, Jr, and M.A. Crimp, accepted for publication in Magnetic Material, Structures, and MRS proceedings (2000).

CHAPTER 7

SUMMARY AND CONCLUSIONS

The objective of this dissertation was to design and develop a sputter deposition system for growing epitaxial films, multilayers, and spin-valves. Furthermore, the results of crystallographic characterization of sputter deposited Nb, Cu, Co, and Py have been correlated to the magnetic and magneto-transport properties of the sputter deposited Py films and Py based spin-valves.

This study resulted in the successful growth of epitaxial Nb($1\bar{1}0$), Cu(111), Co(111), Py(111) films, and Py based spin-valves. The results of AFM and EBSP characterization revealed that Nb grew as high quality epitaxial bcc single-crystal films on Al_2O_3 $(11\bar{2}0)_{hcp}$. Later in the study, epitaxial Cu films were grown on these epitaxial Nb layers. The crystallographic characterization of these Cu films revealed two in-plane twin variants corresponding to two different stacking sequences of {111} fcc planes. Orientation distribution maps revealed that the area of the twin variants varies widely and did not display any particular patterns. Epitaxial Co $(111)_{fcc}$ and Py $(111)_{fcc}$ layers were grown on epitaxial Cu films at high temperature (≥ 350°C). Both Co and Py films also displayed twin variants with orientation maps similar to those observed for epitaxial Cu films. The crystallographic characterization results of Co and Py samples grown at 90°C revealed that two different orientation variants were also present, but in smaller sizes. However, due to the degradation of the associated EBSP patterns and the resolution of EBSP, mapping of the orientation distributions was not possible.

Growth temperature, deposition rates, type of buffer layer, and surface quality of the substrates are important factors that can affect the magnetic properties of single magnetic films and Py based spin-valves. Regardless of the growth temperature and type of buffer layer, no magnetic anisotropy, including magnetocrystalline and magnetoelastic anisotropy, was observed in single epitaxial Py films. In exchange-biased spin-valves, a moderate deposition rate and an ultra-clean substrate resulted in samples with sharp switching of the magnetic moment from the parallel to the antiparallel state and a very flat antiparallel plateau. Studies of the effect of pinning along different in-plane axes on magneto-transport properties of one of the EBSVs revealed the existence of anisotropy in the free ferromagnetic layer, which may be related to differently oriented defects in the Py film which were created during sample preparation (ion milling). Further study of a similar EBSV sample displayed no magnetic anisotropy in the free Py layer.

CONCLUSION:

The growth and subsequent crystallographic nature of metal films and superlattices play important roles in determining the fundamental physical properties of the films. Epitaxed growth of Nb, Cu, Co, and Py films from the basis for growing magnetic multilayers (such as $[Cu\text{-}Co]_N$) and spin-valves (FeMn-Py-Cu-Py [Py: $Ni_{84}Fe_{16}$]) which have applications as GMR (Giant Magneto-Resistance) position sensors, magnetic head readers, and magnetic random access memories. GMR in these devices depends on structural details such as the thin-film growth direction, interfacial roughness and intermixing, and grain boundaries. However, the exact effects of these variables on given systems are not yet well understood. Consequently, it has been necessary to further

characterize the growth and film structure of these magnetic systems to explore the effect of crystal structure on the magneto-transport properties for advanced applications. This project was designed to develop a sputtering deposition system to grow and develop epitaxial films, magnetic multilayers and spin-valves in a preferred orientation.

In conclusion, a sputtering deposition system has been successfully designed and developed to grow epitaxial films. The following projects were carried out in this dissertation:

(1) Surface topography of deposited metallic films (Nb, Cu, Co, and Py) using an atomic force microscope (AFM) in tapping mode.

The AFM results revealed that except for Nb films, which grow with very smooth surfaces (depending on the growth conditions), the rest of the materials (Cu, Co, and Py) always have rough surfaces with islands of different sizes. In general, samples which have been grown under similar conditions, displayed very similar AFM images.

(2) Measurement of crystallographic orientations and grain distributions in deposited films using electron backscatter patterns (EBSP).

The EBSP results revealed that, at high temperature, all fcc materials (Cu, Co, and Py) display two in-plane variants corresponding to two stacking sequences of {111} fcc planes. Orientation maps revealed that the twin variants displayed a random distribution, with no evidence of any particular morphological patterns. The average variant sizes in films grown at elevated temperatures, as determined by the intercept method, were found to be 4 to 6 μm. There was no correlation between the size and

distribution of the twin variants in the EBSP orientation map and the size and distribution of the islands in the AFM images. The relative areas of the twin variants are similar in all materials (Cu, Co, Py) and ranged between 45% and 55%. Epitaxial films of all three materials (Cu, Co, and Py) deposited at room temperature revealed that they grow in small, coherent islands that do not coalesce. Epitaxial films grown at room temperature therefore contain large numbers of grain boundaries, misfit dislocations, and other types of defects.

(3) *Evaluation of magneto-transport properties of sputter deposited epitaxial magnetic films and spin-valves by using CPP-MR and magnetization measurements.*

The important issues in studying the magneto-transport properties of single magnetic films and spin-valves were growth temperature, deposition rates, type of buffer layer and surface quality of the substrates. It was shown that the coercive field in epitaxial single Py films deposited on Cu at 90°C is much larger than those grown on Cu at 350°C, presumably due to the presence of a large number of dislocations and defects which create strain in the deposited films. Growth of Py films on FeMn buffer layers resulted in lower coercive fields, possibly as a result of a reduction of the density of dislocations. Studies of the effect of deposition rate show that moderate Cu deposition rates resulted in sharper switching from the parallel state to antiparallel state, with a wider range of the antiparallel state up to higher fields. The EBSV sample deposited at a high Cu deposition rate produced a significantly different MR loop and displayed slower switching from the parallel to the antiparallel state and larger coercive field. The high coercivity was suggestive of a large number of dislocations and defects in the spin-valve, producing strain in this sample. The deposition substrate temperature was also an important factor

in the fabrication of epitaxial spin-valves. It was observed that the Py (ferromagnetic) layer adjacent to the FeMn (antiferromagnetic) in spin-valves deposited at a substrate temperature of 90°C did not have a strong exchange coupling (pinning) to the FeMn layer and the exchange-biased field weakened as spin-valve exposed to high magnetic field, opposite to the easy axis. Magnetic anisotropy was observed in one symmetrical EBSV which appeared to be related to existence of some oriented defects and strain induced during sample preparation. There were two noticeable differences between the CPP-MR hysteresis loops in the epitaxial and polycrystalline exchange-biased spin-valves with an identical layer structure. The epitaxial samples exhibited fast switching from the parallel to the antiparallel state for a small applied field while the antiparallel state plateau was much flatter (higher resistance state remain up to larger magnetic field). The CPP-resistance in the epitaxial sample (in parallel state) was almost twice that of a similar polycrystalline spin-valve; however the values of GMR were similar.

FUTURE STUDIES:

Crystallographic Characterization: EBSP is a convenient and accurate characterization technique for the determination of the orientation distribution in epitaxial films. These orientation variants are distinguished by a change in the Kikuchi bands in the patterns. As explained in the Chapter 4, the analysis of EBSP patterns from epitaxial Cu, Co, and Py deposited at 90°C revealed that both variants coexist within the EBSP interaction volume. However, in the films grown at room temperature the patterns were unsolvable, and without consistent band indexing, it is impossible to fully characterize the variant size and distribution. Therefore, different crystallographic characterization techniques, such as TEM and HRTEM, are needed to study these samples to observe the existence of small grains, as well as to study the interface roughness of these samples.

Magneto-transport characterization: The results of magneto-transport studies showed that the second antiparallel state in the CPP-MR hysteresis loop was not established due to distortion of the exchange-bias coupling (pinning) between the antiferromagnetic (FeMn) layer and the adjacent ferromagnetic (Py) layer as sample was exposed to high magnetic fields (at the second parallel-state). It was concluded that the growth of epitaxial Py and FeMn at moderate temperature (90°C) did not allow a strong exchange bias coupling between the ferromagnetic and antiferromagnetic layers. Similar behavior was also seen in the standard and micron-sizes polycrystalline EBSVs. Therefore, additional micro-size epitaxial spin-valve samples need to be fabricated at low temperature ($30°C > T > -30°C$) to confirm the temperature dependence issue.